

REPORT DOCUMENTATION PAGE			Form Approved OMB NO. 0704-0188		
<p>The public reporting burden for this collection of information is estimated to average 1 hour per response, including the time for reviewing instructions, searching existing data sources, gathering and maintaining the data needed, and completing and reviewing the collection of information. Send comments regarding this burden estimate or any other aspect of this collection of information, including suggestions for reducing this burden, to Washington Headquarters Services, Directorate for Information Operations and Reports, 1215 Jefferson Davis Highway, Suite 1204, Arlington VA, 22202-4302. Respondents should be aware that notwithstanding any other provision of law, no person shall be subject to any penalty for failing to comply with a collection of information if it does not display a currently valid OMB control number.</p> <p>PLEASE DO NOT RETURN YOUR FORM TO THE ABOVE ADDRESS.</p>					
1. REPORT DATE (DD-MM-YYYY) 15-12-2015		2. REPORT TYPE Final Report		3. DATES COVERED (From - To) 20-Aug-2008 - 19-Nov-2016	
4. TITLE AND SUBTITLE Final Report: Resolving and Discriminating Overlapping Anomalies from Multiple Objects in Cluttered Environments			5a. CONTRACT NUMBER W911NF-08-1-0385		
			5b. GRANT NUMBER		
			5c. PROGRAM ELEMENT NUMBER		
6. AUTHORS Fridon Shubitidze, John Sigman, Yinlin Wang, Irma Shamatava, Juan Pablo Fernandez, Alex Bijamov, D. Karkashadze			5d. PROJECT NUMBER		
			5e. TASK NUMBER		
			5f. WORK UNIT NUMBER		
7. PERFORMING ORGANIZATION NAMES AND ADDRESSES Dartmouth College 11 Rope Ferry Rd. Hanover, NH 03755 -1404			8. PERFORMING ORGANIZATION REPORT NUMBER		
9. SPONSORING/MONITORING AGENCY NAME(S) AND ADDRESS (ES) U.S. Army Research Office P.O. Box 12211 Research Triangle Park, NC 27709-2211			10. SPONSOR/MONITOR'S ACRONYM(S) ARO		
			11. SPONSOR/MONITOR'S REPORT NUMBER(S) 55000-EV.19		
12. DISTRIBUTION AVAILABILITY STATEMENT Approved for Public Release; Distribution Unlimited					
13. SUPPLEMENTARY NOTES The views, opinions and/or findings contained in this report are those of the author(s) and should not be construed as an official Department of the Army position, policy or decision, unless so designated by other documentation.					
14. ABSTRACT The primary objective of the project#55000-EV entitled "Resolving and Discriminating Overlapping Anomalies from Multiple Objects in Cluttered Environments" was to mitigate the effects of dispersed metallic clutter, to resolve the contribution of independent or coupled objects to the composite EMI data, and to discriminate each object of interest based on its response under more realistic field conditions. Specific objectives were: 1. Research techniques that minimize the contribution of clutter by using upward projection methods on data acquired at field sites with instruments such as the MPV, TEMTADS, BUD, and GEM-3D+					
15. SUBJECT TERMS EMI, Sensing, High Frequency EMI, UXO, detection, Classification					
16. SECURITY CLASSIFICATION OF:			17. LIMITATION OF ABSTRACT UU	15. NUMBER OF PAGES	19a. NAME OF RESPONSIBLE PERSON Fridon Shubitidze
a. REPORT UU	b. ABSTRACT UU	c. THIS PAGE UU			19b. TELEPHONE NUMBER 603-646-3671

Report Title

Final Report: Resolving and Discriminating Overlapping Anomalies from Multiple Objects in Cluttered Environments

ABSTRACT

The primary objective of the project#55000-EV entitled "Resolving and Discriminating Overlapping Anomalies from Multiple Objects in Cluttered Environments" was to mitigate the effects of dispersed metallic clutter, to resolve the contribution of independent or coupled objects to the composite EMI data, and to discriminate each object of interest based on its response under more realistic field conditions. Specific objectives were:

1. Research techniques that minimize the contribution of clutter by using upward projection methods on data acquired at field sites with instruments such as the MPV, TEMTADS, BUD, and GEM-3D+
2. Develop an N-target locator that, without any computationally expensive optimizations, provides an estimate of the number of objects within in a sensor's field of view and their locations and orientations
3. Formulate robust classifiers that segregate N objects into UXO and non-UXO based on their isolated EMI responses
4. Discriminate UXO-like targets using rigorous models (NSMS, SEA) which explicitly include coupling between targets if required.

To address these objectives, under this project first we developed physically complete forward approaches:

- ? Standardized Excitation Approach for understanding modeling targets EMI responses in great details.
- ? Normalized surface magnetic source model (NSMS) for EMI sensors data inversion and classification.
- ? Orthonormalized volume magnetic source model (ONVMS) for next generation EMI systems data analysis and subsurface multiple targets classification.

These models were combined with advanced signal processing and data-inversion approaches, which provided robust regularization and classification feature parameters estimations for targets intrinsic, such as magnetic polarizabilities, multi-static data matrix eigenvalues, and extrinsic, i.e. targets locations and orientations. These advanced signal processing algorithms are:

- ? Joint diagonalization for multi-target data pre-processing (JD)
- ? Differential evolution (DE) for estimating targets locations and orientations.
- ? A field-potential (HAP) method to locate targets.

Our advanced forward-inverse and signal processing algorithms have been applied to next generation sensors data sets collected at several live UXO sites.

- ? We developed site specific UXO libraries for each live UXO sites. These libraries were used for targets classification via a finger-print matching technique.

- ? Our models were adapted to all next-generation sensors, including the MetalMapper, TEMTADS and MPV data sets. The models were applied to blind live-site UXO discriminations studies. The studies have demonstrated the excellent discrimination capabilities.

Enter List of papers submitted or published that acknowledge ARO support from the start of the project to the date of this printing. List the papers, including journal references, in the following categories:

(a) Papers published in peer-reviewed journals (N/A for none)

Received

Paper

09/01/2014	18 Fridon Shubitidze, Juan Pablo Fernandez, Benjamin E. Barrowes, Irma Shamatava, Alex Bijamov, Kevin O'Neill, David Karkashadze. The Orthonormalized Volume Magnetic Source Model for Discrimination of Unexploded Ordnance, IEEE Transactions on Geoscience and Remote Sensing, (08 2014): 0. doi: 10.1109/TGRS.2013.2283346
------------	--

TOTAL: 1

Number of Papers published in peer-reviewed journals:

(b) Papers published in non-peer-reviewed journals (N/A for none)

Received Paper

TOTAL:

Number of Papers published in non peer-reviewed journals:

(c) Presentations

1. HFEMI for Intermediate conductive objects and voids detection

Number of Presentations: 1.00

Non Peer-Reviewed Conference Proceeding publications (other than abstracts):

Received Paper

09/01/2014	16	Fridon Shubitidze,, Benjamin Barrowes, , John Sigman, , Kevin O'Neill,, Irma Shamatava . High Frequency Electromagnetic Induction Sensing for Non-Metallic Ordnances Detection , DIPED-2014. 23-SEP-14, . : ,
09/03/2013	7	Irma Shamatava , Fridon Shubitidze, Roman Joabava, Benjamin E. Barrowes, Kevin O'Neill, Alex Bijamov. APPLICATION OF THE ONVMS MODEL TO DISCRIMINATECHALLENGING UXO TARGETS , Direct and Inverse Problems of Electromagnetic and Acoustic Wave Theory (DIPED), 2012 XVIIth International Seminar/Workshop on. 24-SEP-12, . : ,
09/03/2013	8	F. Shubitidze, Irma Shamatava,, Juan P. Fernández, , Benjamin E. Barrowes,, Kevin O'Neill, Alex Bijamov. ONVMS APPLIED TO A NEW ADVANCED PORTABLE EMI SYSTEMDATA, 2012 XVIIthInternational Seminar/Workshop on Direct and InverseProblems of Electromagnetic and Acoustic Wave Theory . 24-SEP-12, . : ,

TOTAL: 3

Peer-Reviewed Conference Proceeding publications (other than abstracts):

<u>Received</u>	<u>Paper</u>
08/16/2012 5.00	Benjamin E. Barrowes, Fridon Shubitidze, Tomasz M. Grzegorzczk, Pablo Fernandez, Kevin O'Neill. Pedemis: a portable electromagnetic induction sensor with integrated positioning, Detection and Sensing of Mines, Explosive Objects, and Obscured Targets XVII. 27-APR-12, Baltimore, Maryland, USA. : ,
09/01/2014 15.00	Steven S. Bishop, Jason C. Isaacs, Steven A. Grant, Benjamin E. Barrowes, Fridon Shubitidze, Steven A. Arcone. Homemade explosives in the subsurface as intermediate electrical conductivity materials, a new physical principle for their detection, SPIE Defense + Security. 05-MAY-14, Baltimore, Maryland, USA. : ,
09/03/2013 9.00	Benjamin E. Barrowes, Tomasz M. Grzegorzczk, Fridon Shubitidze, Pablo Fernández, Kevin O'Neill, J. Thomas Broach, Jason C. Isaacs, Leslie M. Collins. The Pedemis Instrument: operation and APG field results, SPIE Defense, Security, and Sensing. 29-APR-13, Baltimore, Maryland, USA. : ,
09/03/2013 10.00	Juan Pablo Fernández, Benjamin Barrowes, Kevin O'Neill, Irma Shamatava, Fridon Shubitidze, . Toward a real-time positioning system for a portable EMI sensor, SPIE Defense, Security, and Sensing. 29-APR-13, Baltimore, Maryland, USA. : ,
09/03/2013 11.00	Benjamin E. Barrowes, Fridon Shubitidze, Tomasz M. Grzegorzczk, Pablo Fernández, Kevin O'Neill, . Pedemis: a portable electromagnetic induction sensor with integrated positioning, SPIE Defense, Security, and Sensing. 23-APR-12, Baltimore, Maryland. : ,
09/03/2013 12.00	Fridon Shubitidze, Benjamin E. Barrowes, Irma Shamatava, Juan Pablo Fernandez, Alex Bijamov, Kevin O'Neill, . Advanced UXO discrimination: resolving multiple targets and overlapping EMI signals</title>, SPIE Defense, Security, and Sensing. 23-APR-11, Orlando, Florida. : ,
09/03/2013 13.00	Juan Pablo Fernández, Benjamin Barrowes, Alex Bijamov, Tomasz Grzegorzczk, Nicolas Lhomme, Kevin O'Neill, Irma Shamatava, Fridon Shubitidze, . MPV-II: an enhanced vector man-portable EMI sensor for UXO identification</title>, SPIE Defense, Security, and Sensing. 23-APR-11, Orlando, Florida. : ,
09/03/2013 14.00	F. Shubitidze, J. P. Fernández, I. Shamatava, A. Luperon, B. E. Barrowes, K. O'Neill, A. Bijamov, . Inversion-free discrimination of unexploded ordnance in real time, SPIE Defense, Security, and Sensing. , Baltimore, Maryland. : ,
TOTAL:	8

Number of Peer-Reviewed Conference Proceeding publications (other than abstracts):

(d) Manuscripts	
<u>Received</u>	<u>Paper</u>
TOTAL:	

Number of Manuscripts:

Books	
<u>Received</u>	<u>Book</u>
TOTAL:	

Received Book Chapter

TOTAL:

Patents Submitted

Patents Awarded

Awards

Graduate Students

<u>NAME</u>	<u>PERCENT SUPPORTED</u>	Discipline
John Sigman	0.80	
Yinlin Wang	0.90	
FTE Equivalent:	1.70	
Total Number:	2	

Names of Post Doctorates

<u>NAME</u>	<u>PERCENT SUPPORTED</u>
FTE Equivalent:	
Total Number:	

Names of Faculty Supported

<u>NAME</u>	<u>PERCENT SUPPORTED</u>	National Academy Member
Fridon Shubitidze	0.50	
Alex Hartov	0.04	
FTE Equivalent:	0.54	
Total Number:	2	

Names of Under Graduate students supported

<u>NAME</u>	<u>PERCENT SUPPORTED</u>
FTE Equivalent:	
Total Number:	

Student Metrics

This section only applies to graduating undergraduates supported by this agreement in this reporting period

The number of undergraduates funded by this agreement who graduated during this period: 0.00

The number of undergraduates funded by this agreement who graduated during this period with a degree in science, mathematics, engineering, or technology fields:..... 0.00

The number of undergraduates funded by your agreement who graduated during this period and will continue to pursue a graduate or Ph.D. degree in science, mathematics, engineering, or technology fields:..... 0.00

Number of graduating undergraduates who achieved a 3.5 GPA to 4.0 (4.0 max scale):..... 0.00

Number of graduating undergraduates funded by a DoD funded Center of Excellence grant for Education, Research and Engineering:..... 0.00

The number of undergraduates funded by your agreement who graduated during this period and intend to work for the Department of Defense 0.00

The number of undergraduates funded by your agreement who graduated during this period and will receive scholarships or fellowships for further studies in science, mathematics, engineering or technology fields:..... 0.00

Names of Personnel receiving masters degrees

<u>NAME</u>
Yinlin Wang
Total Number:

Names of personnel receiving PhDs

<u>NAME</u>

Total Number:

Names of other research staff

<u>NAME</u>	<u>PERCENT SUPPORTED</u>
-------------	--------------------------

Irma Shamatava	0.50
----------------	------

FTE Equivalent:	0.50
------------------------	-------------

Total Number:	1
----------------------	----------

Sub Contractors (DD882)

Inventions (DD882)

Scientific Progress

The primary objective of the project#55000-EV entitled "Resolving and Discriminating Overlapping Anomalies from Multiple Objects in Cluttered Environments" was to mitigate the effects of dispersed metallic clutter, to resolve the contribution of independent or coupled objects to the composite EMI data, and to discriminate each object of interest based on its response under more realistic field conditions. Specific objectives were:

1. Research techniques that minimize the contribution of clutter by using upward projection methods on data acquired at field sites with instruments such as the MPV, TEMTADS, BUD, and GEM-3D+
2. Develop an N-target locator that, without any computationally expensive optimizations, provides an estimate of the number of objects within in a sensor's field of view and their locations and orientations
3. Formulate robust classifiers that segregate N objects into UXO and non-UXO based on their isolated EMI responses
4. Discriminate UXO-like targets using rigorous models (NSMS, SEA) which explicitly include coupling between targets if required.

To address these objectives, under this project first we developed physically complete forward approaches:

- ? Standardized Excitation Approach for understanding modeling targets EMI responses in great details.
- ? Normalized surface magnetic source model (NSMS) for EMI sensors data inversion and classification.
- ? Orthonormalized volume magnetic source model (ONVMS) for next generation EMI systems data analysis and subsurface multiple targets classification.

These models were combined with advanced signal processing and data-inversion approaches, which provided robust regularization and classification feature parameters estimations for targets intrinsic, such as magnetic polarizabilities, multi-static data matrix eigenvalues, and extrinsic, i.e. targets locations and orientations. These advanced signal processing algorithms are:

- ? Joint diagonalization for multi-target data pre-processing (JD)
- ? Differential evolution (DE) for estimating targets locations and orientations.
- ? A field-potential (HAP) method to locate targets.

Our advanced forward-inverse and signal processing algorithms have been applied to next generation sensors data sets collected at several live UXO sites.

? We developed site specific UXO libraries for each live UXO sites. These libraries were used for targets classification via a finger-print matching technique.

? Our models were adapted to all next-generation sensors, including the MetalMapper, TEMTADS and MPV data sets. The models were applied to blind live-site UXO discriminations studies. The studies have demonstrated the excellent discrimination capabilities.

Technology Transfer

The technologies developed under this project have been presented on various conferences, transferred and shared to USA army cold regions research laboratory and UXO community.



Resolving and Discriminating Overlapping Anomalies from Multiple Objects in Cluttered Environments

55000-EV– Final Report

Principal Investigator: *Dr. Fridon Shubitidze*

Thayer School of Engineering, Dartmouth College

December 2015

Table of Contents

Table of Contents	ii
List of Figures	v
List of Tables	viii
List of Acronyms	ix
Abstract	1
Acknowledgements	2
1 Introduction	3
1.1 Background and objectives	3
1.2 Report structure	4
2 Forward models	6
2.1 Introduction	6
2.2 The Generalized Standardized Excitation Approach for UXO discrimination	8
2.2.1 The Model Based SEA	9
2.2.2 Efficient calculation of spheroidal modal expansion coefficients	12
2.2.3 Numerical results: The universal RSS	13
2.2.4 Data derived generalized SEA applied to MPV TD data	17
2.2.5 Numerical results for the DATA-Derived GSEA	20
2.3 The single-dipole approximation	25
2.4 Normalized surface magnetic source model	27
2.4.1 Governing equations	27
2.4.2 Theoretical basis of NSMS	28
2.4.3 Formulation for bodies of revolution; determining NSMS amplitudes from data	30
2.4.4 The dipole model as a limiting case of NSMS	34
2.4.5 Invariance properties of the total NSMS	36
2.4.6 Interpretation of the total NSMS	37
2.4.7 The parameterized NSMS	37
2.5 The orthonormalized volume magnetic source model	38
2.5.1 Orthonormal Green functions	40
2.5.2 ONVMS procedure	42

2.6	Joint diagonalization for multi-target data pre-processing	43
2.6.1	The multi-static response matrix	43
2.6.2	Interpretation and diagonalization of the MSR matrix	44
2.6.3	Algorithm for joint diagonalization.....	47
3	Inverse Models.....	49
3.1	Introduction	49
3.2	Gradient-based methods of optimization.....	50
3.2.1	Stepwise optimization.....	52
3.2.2	Simultaneous optimization	52
3.2.3	Condensed algorithm.....	52
3.3	Differential evolution	53
3.4	The HAP method.....	55
3.4.1	Estimating the location and orientation of buried objects	55
3.4.2	A simplified HAP method	57
3.4.3	Determining the HAP amplitudes.....	57
3.4.4	The HAP method with gradient information	59
3.4.5	Estimating object location using measured monostatic and multistatic EMI data.....	60
4	ESTCP live-site classification studies using advanced models	72
4.1	Introduction	72
4.2	Camp Sibert.....	72
4.2.1	Target location and characterization; preliminary pattern-matching classification	73
4.2.2	SVM classification	77
4.2.3	SVM analysis of Camp Sibert data: summary.....	82
4.2.4	Mixed model approach applied to Camp Sibert data.....	83
4.3	Camp Butner.....	85
4.3.1	TEMTADS data discrimination strategy and classification results using supervised clustering.....	87
4.4	Camp George West.....	91
4.4.1	Camp George West MPV data inversion and classification scheme	91

5	Conclusions.....	99
6	References.....	100

List of Figures

Figure 1: Problem geometry, with additional fictitious spheroid.	9
Figure 2: Frequency-domain EMI response for 81 mm UXO; (a) GEM-3 excitation; (b) nose up vertical, (c) nose up 45° inclination, (d) horizontal.	14
Figure 3: Time-domain EMI response for 81-mm UXO; (a) EM-3 excitation; (b) nose up vertical, (c) nose up 45° inclination, (d) horizontal.	15
Figure 4: Problem geometry and reduced set of sources $\mathbf{p}_i^{\text{pmn}}$ distributed along rings on the spheroid surface.	18
Figure 5: Actual and schematic diagram of the MPV-TD sensor.	21
Figure 6: The measured and modeled scattered magnetic field flux at given time channel versus observation points; A) H_x magnetic field flux; b) H_z magnetic field flux.	23
Figure 7: The measured and modeled scattered magnetic field versus frequency and distance.	24
Figure 8: A dipole's location in a global coordinate system.	25
Figure 9: The NSMC that are distributed on a prolate spheroidal surface is implemented for a body of revolution. The prolate spheroidal coordinate system is specified by (ξ, η, ϕ)	32
Figure 10: A schematic diagram for a dipole model.	35
Figure 11: A metallic object under the transmitter. The target's EMI response at the receiver coil can be calculated from the equivalent surface or volume magnetic dipole moment $d\mathbf{m}$	39
Figure 12: The HAP approach for a dipole.	55
Figure 13: Determining the location and orientation of a buried target. The method assumes the object is a point dipole and exploits an analytic relation between the field measured at \mathbf{r}_i and the scalar potential at the same point to find the location \mathbf{r}_d . The potential is constructed using a layer of equivalent magnetic sources placed between the sensor and the object; \mathbf{r}_s is a typical location on the layer.	58
Figure 15. The GEM-3D+ sensor head showing the transverse receiver coils.	60
Figure 15. Comparisons between actual and modeled H_z data.	60
Figure 16. Comparisons between actual and predicted data for a sphere subject to GEM-3D+ excitation: (a) x-component, (b) y-component.	61
Figure 17. Estimated $\sqrt{x_c^2 + y_c^2}$ (left) and z_c (right) for the steel sphere. The true $z_c = 26$ cm.	62
Figure 18. Comparison between GEM-3D+ blind tests inversions and library NSMS.	64
Figure 19. Estimated z_c for the 81-mm UXO. The true $z_c = 60$ cm.	65
Figure 20. Actual and schematic diagram of the MPV-TD sensor.	66
Figure 21. Predicted and actual TD MPV data for a 60-mm UXO.	67
Figure 22. NSMS model comparison to library for Target #1.	69
Figure 23. NSMS model comparison to library for Target #4 (left) and Target #5 (right).	69
Figure 24. NSMS model comparison to library for Target #2 (left) and Target #3 (right).	70

Figure 25: Camp Sibert anomalies: 4.2 inch, base plates and partial mortars.	73
Figure 26: Camp Sibert EM-63 near field distributions: Left and middle columns: actual and modeled data respectively. Right column: misfits.....	75
Figure 27: Inverted total NSMS for all anomalies: 4.2" mortars, base plates, and partial mortars.	76
Figure 28: <i>Left</i> : Classification features. <i>Right</i> : ROC curve of NSMS performance.....	76
Figure 29: a) Unexploded shell from Cell No. 7 and (b,c) the two false alarms obtained by the SVM classifier using k and $Q(t_{15})/Q(t_1)$ as discriminators.....	77
Figure 30: Result of the SVM classification for the Camp Sibert anomalies using the logarithms of k and $R = Q(t_{15})/Q(t_1)$. The SVM has been trained with capacity $C = 10$ and kernel width $\sigma = 1/200$. The small markers denote the ground truth for both training (hollow) and testing (solid) cells. The larger markers highlight the cases where there is disagreement between the ground truth and the SVM prediction.....	78
Figure 31: Result of the SVM classification for the Camp Sibert anomalies using the logarithms of the Pasion-Oldenburg parameters k and γ . The SVM here has a capacity $C = 9$. The small markers denote the ground truth for both training (hollow) and testing (solid) cells. The larger markers show the wrong SVM predictions.	80
Figure 32: Result of the SVM classification for the Camp Sibert Anomalies using the logarithms of the Pasion- Oldenburg parameters β and γ . The SVM capacity $C = 10^5$. The small markers denote the ground truth for both training (hollow) and testing (solid) cells. The larger markers highlight the wrong predictions made by the SVM.....	80
Figure 33: SVM classification of the Camp Sibert Anomalies using the logarithms of k , b , and g . The SVM has $C = 9$. The small markers denote the ground truth for both training and testing cells. The larger markers highlight the cases where there is disagreement between the ground truth and the SVM prediction.	81
Figure 34: Log-scale plot of $Q(t_{15})/Q(t_1)$ vs. k for Camp Sibert data classification. <i>Left</i> : Ground truth. <i>Right</i> : K -means clustering result.....	84
Figure 35: Classification of 216 targets into five classes using a bivariate normal mixture. Also shown are the 95% confidence ellipses.	84
Figure 36: Five ROC curves that indicate the performance of the mixed model approach to Camp Sibert data.	85
Figure 37: TEMTADS multi-static response matrix eigenvalues versus time for some samples of requested anomalies.	86
Figure 38: TEMTADS multi-static response matrix eigenvalues versus time for a 105-mm HE projectile and a 105-mm HEAT round (top row), an M-48 Fuze and a 37-mm munition (center row), and two clutter scenarios, one with two items (left) and another with several (right) (third row).	88
Figure 39: Inverted total ONVMS time-decay profiles for four Camp Butner targets: (top row) 105-mm HE munition and 105-mm HEAT round, and (bottom) M-48 Fuze and 37-mm projectile with copper band.	89
Figure 40: Inverted total ONSMS time decay profiles for a 37-mm projectile without copper band.	90
Figure 41: ROC curve for the Camp Butner TEMTADS test data.	90

Figure 42. Camp George West MPV multi-static response matrix eigenvalues versus time for some samples of background, 75 mm, ISO and clutter anomalies.....	92
Figure 43. Inverted total ONVMS time-decay profiles for a 75 mm projectile in the Camp George West study, Anomaly #57.	93
Figure 44. Scatter plot of size and decay for all Camp George West anomalies based on the extracted total ONVMS for time channels N# 5, 10, 20, and 35.....	94
Figure 45. Result of the clustering for the Camp George West anomalies using the size and shape information for $n = 90$. The circles denote the anomalies for which the ground truth was asked.....	95
Figure 46. Inverted total ONVMS time-decay profiles for ISO (upper figure) and 75 mm projectiles (lower figure) targets.	96
Figure 47. Inverted total ONVMS time-decay profiles for whole and partial native partial 75 mm projectiles. Green, black and blue lines are for total $ONMVS_{zz}$, $ONMVS_{yy}$ and $ONMVS_{xx}$, respectively.	97
Figure 48. ROC curve for the Camp George West data.	98

List of Tables

Table 1. Estimated and actual positions and orientations for the GEM-3D+ blind-test data runs.	63
Table 2. Ground truth for the MPV-TD blind-test data runs.	68
Table 3. Inverted results for position and orientation for MPV-TD blind-test data. Numbers with an asterisk are arbitrary due to BOR considerations.	68
Table 4: SVM classification of Camp Sibert anomalies using k and R with $C = 10$	78
Table 5: SVM classification of Camp Sibert anomalies using γ and k with $C = 9$	79
Table 6: SVM classification of Camp Sibert anomalies using β and γ with $C = 105$	81
Table 7: SVM classification of Camp Sibert anomalies using the complete NSMS time decay	81

List of Acronyms

3D	Three-Dimensional
AIC	Akaike Information Criterion
APG	Aberdeen Proving Ground
BIC	Bayesian Information Criterion
BOR	Body of Revolution
BUD	Berkeley UXO Discriminator
cm	Centimeter
CRREL	Cold Regions Research and Engineering Laboratory
DE	Differential Evolution
DGPS	Differential Global Positioning System
DoD	Department of Defense
DOE	Department of Energy
EM	Expectation Maximization
EMI	Electromagnetic Induction
ESTCP	Environmental Security Technology Certification Program
FD	Frequency Domain
GSEA	Generalized Standardized Excitation Approach
HAP	(1) magnetic field vector \mathbf{H} , (2) vector potential \mathbf{A} , (3) scalar magnetic Potential ψ
Hz	Hertz
ID	Identification
LS	Least Squares
m	Meter
MAS	Method of Auxiliary Sources
MD	Multi-Dipole

MDL	Minimum Description Length
MEG	Magnetoencephalographic
ML	Maximum Likelihood
mm	Millimeter
ms	Millisecond
μ s	Microsecond
MM	MetalMapper
MNM	Multivariate Normal Mixture
MPV	Man-Portable Vector
MT	Mixed Theory
MUSIC	Multiple Signal Classification
NMMS	Non-metric Multidimensional Scaling
NRL	Naval Research Laboratory
NSMC	Normalized Surface Magnetic Charge
NSMS	Normalized Surface Magnetic Source
ONVMS	Ortho-Normalized Volume Magnetic Source Model
PCA	Principal Component Analysis
PNN	Probabilistic Neural Network
RBF	Radial Basis Function
ROC	Receiver Operating Characteristic
RSS	Residual Sum of Squares
RTS	Robotic Total Station
SEA	Standard Excitation Approach
SFS	Scattered Field Singularities
SLO	San Luis Obispo
SNR	Signal-to-Noise Ratio

SS	Sum of Squares
SVM	Support Vector Machine
TD	Time Domain
TEM	Time Domain Electromagnetic
TEMTADS	Time Domain Electromagnetic Towed Array Detection System
TNLL	Twice-Negative Log-Likelihood Function
TOI	Target Of Interest
TSA	Thin Skin Approximation
UXO	Unexploded Ordnance
VRM	Viscous Magnetic Remanence

Abstract

The primary objective of the project#55000-EV entitled "*Resolving and Discriminating Overlapping Anomalies from Multiple Objects in Cluttered Environments*" was to mitigate the effects of dispersed metallic clutter, to resolve the contribution of independent or coupled objects to the composite EMI data, and to discriminate each object of interest based on its response under more realistic field conditions. Specific objectives were:

1. Research techniques that minimize the contribution of clutter by using upward projection methods on data acquired at field sites with instruments such as the MPV, TEMTADS, BUD, and GEM-3D+
2. Develop an N-target locator that, without any computationally expensive optimizations, provides an estimate of the number of objects within in a sensor's field of view and their locations and orientations
3. Formulate robust classifiers that segregate N objects into UXO and non-UXO based on their isolated EMI responses
4. Discriminate UXO-like targets using rigorous models (NSMS, SEA) which explicitly include coupling between targets if required.

To address these objectives, under this project first we developed physically complete forward approaches:

- Standardized Excitation Approach for understanding modeling targets EMI responses in great details.
- Normalized surface magnetic source model (NSMS) for EMI sensors data inversion and classification.
- Orthonormalized volume magnetic source model (ONVMS) for next generation EMI systems data analysis and subsurface multiple targets classification.

These models were combined with advanced signal processing and data-inversion approaches, which provided robust regularization and classification feature parameters estimations for targets intrinsic, such as magnetic polarizabilities, multi-static data matrix eigenvalues, and extrinsic, i.e. targets locations and orientations. These advanced signal processing algorithms are:

- Joint diagonalization for multi-target data pre-processing (JD)
- Differential evolution (DE) for estimating targets locations and orientations.
- A field-potential (HAP) method to locate targets.

Our advanced forward-inverse and signal processing algorithms have been applied to next generation sensors data sets collected at several live UXO sites.

- We developed site specific UXO libraries for each live UXO sites. These libraries were used for targets classification via a finger-print matching technique.
- Our models were adapted to all next-generation sensors, including the MetalMapper, TEMTADS and MPV data sets. The models were applied to blind live-site UXO discriminations studies. The studies have demonstrated the excellent discrimination capabilities.

Acknowledgements

The Principal Investigator, Dr. Fridon Shubitidze of Dartmouth College, conceived, implemented, and tested most of the approaches presented in this report. He developed advanced forward and inverse EMI models, combined them with advanced signal processing, and successfully applied them to live-site UXO data sets.

Dr. Juan Pablo Fernández of Dartmouth College combined the SVM technique with advanced EMI techniques, modeled MPV sensor data sets and conducted Camp Sibert, AL and MPV data discrimination studies,

Dr. Alex Bijamov implemented statistical clustering algorithms for ONVMS and performed inversion and discrimination studies for Camp Butner TEMTADS data.

Dr. David Karkashadze, visiting professor at Dartmouth College, developed the mathematical basis of the HAP and ONVMS techniques.

Mrs. Irma Shamatava adapted the advanced models to next-generation sensor data and conducted various inversion and discrimination studies.

Mr. Yinlin Wang implement multi targets inversion algorithms using the joint diagonalization technique and applied them to advanced sensors (5x5 and 2x2 3D TEMATDS) data sets.

Mr. John Sigman implemented advanced classification algorithms for estimating the dig stop point.

Dr. Benjamin Barrowes and Dr. Kevin O'Neill of the US Army ERDC-CRREL participated in the development and testing of advanced forward EMI models.

Funding for this project was provided by the Army Research Office. We wish to express our sincere appreciation to Dr. Russel Harmon and Dr. David Steps, and the staff of the ARO for their support.

1 Introduction

1.1 Background and objectives

The well-known and prohibitive cost of carefully excavating all geophysical anomalies detected at lands contaminated with unexploded ordnance (UXO) is one of the greatest impediments to performing an efficient and thorough cleanup of former battlefields and of Department of Defense (DoD) and Department of Energy (DOE) sites. Innovative discrimination techniques are required that can quickly and reliably distinguish between hazardous UXO and non-hazardous metallic items. The key to success lies in the development of advanced processing techniques that can analyze and process sophisticated magnetic or electromagnetic induction data, with its novel waveforms, ever improving quality, and vector or tensor character, so as to maximize the probability of correct classification and minimize the false-alarm rate.

The objective of the proposed work was to mitigate the effects of discrete metallic clutter from EMI data, and the simultaneous discrimination of multiple anomalies in close proximity with overlapping EMI responses. Specifically, we aimed to develop a robust approach for processing high quality data to mitigate the effects of clutter using continuation techniques which tend to suppress the response from small clutter-like targets, and then discriminate UXO from non-UXO targets at highly contaminated sites that include challenging terrain, vegetation, water effects, and geology using rigorous models that may include interaction effects.

- Develop 3D EMI model for highly conducting and permeable metallic objects in order to understand interaction effects between the objects and the surrounding host medium. Here studies were conducted for state of the art sensors, such as frequency domain GEM-3D and time domain MPV sensors. The noise levels associated with sensor position accuracy and surrounding medium are studied. The fast, regularization free algorithm called H-A-Phi technique are adapted to frequency domain GEM-3D and time domain MPV sensors to estimate objects location, orientation in conducting background. The performance of the forward models, such as multi dipole model, NSMC and GSEA are tested for UXOs that are buried in conducting ground. Statistical and supervised machine learning algorithms are utilized for UXO identification.
- Research techniques that minimize the contribution of metallic and geologic clutter by using data projection methods on data acquired at field sites with instruments such as the MPV-MM1443, TEMTADS, Metal Mapper and GEM-3D+. High quality, well located data from these sensors are used which provided an unmatched level of data fidelity.

- Develop an N-target locator, able to provide estimates of the number of targets present in the sensors field of view along with their locations and orientations, without resorting to computationally expensive optimizations. This locator utilizes high quality EMI data without solving the traditional ill posed inverse scattering problem. Here, two approaches for this N-target locator are investigated: (a) $\{H, A, \psi\}$ (HAP) method based on scattered magnetic field H , magnetic vector potential A , and magnetic scalar potential ψ assuming only dipolar responses; Extend a non-linear signal-processing algorithm, called the differential evolution algorithm.
- Formulate robust classifiers that segregate N targets into UXO and non-UXO. This classifier considers model based parameters such as volume and polarizabilities for using rapid statistical techniques such as Support Vector Machines (SVM) techniques; discriminate UXO-like targets using rigorous (NSMS, SEA) models which explicitly include coupling between targets if required; investigate the complexities of the soil EMI response in both the frequency and time domains.

1.2 Report structure

Chapter 2 outlines the theoretical basis of the advanced EMI forward models that we use to represent the EMI response of obscured targets, the workhorses at the core of our whole procedure. We first present the GSEA, which is a robust for representing targets EMI response, but insufficient for fast inversions. We then introduce and study in detail the NSMS model, which distributes dipoles on a closed surface surrounding a target of interest. After that we derive and describe the ONVMS technique, which infuses dipoles throughout the subsurface volume illuminated by a sensor. We end by describing a data-preprocessing technique based on joint diagonalization that estimates the number of targets in a measurement with no need for data inversion; the method, moreover, can provide initial estimates of target locations and perform rudimentary discrimination.

Chapter 3 discusses inverse models: the methods used to harness the forward models so they provide relevant intrinsic and extrinsic information starting from measured data. After presenting some traditional gradient-search based methods and pointing out some of their limitations we describe differential evolution, a state-of-the-art global-search method, similar in character to genetic algorithms, that has shown remarkable flexibility and usefulness. We end by describing the HAP method, a semi-analytic non-iterative procedure to locate buried targets and presenting some results.

Finally, Chapter 4 provides a detailed account of the discrimination and classification studies performed on data from actual UXO sites—the Camp Sibert in Alabama, Camp George West in Colorado, and Camp Butner in North Carolina—in which several combinations of the techniques

presented in the previous chapters were used. We describe our solution strategies and the results we obtained.

2 Forward models

2.1 Introduction

Distinguishing an object of interest from innocuous items is the main problem that the UXO community is facing currently. This inverse problem demands fast and accurate representation of target EMI response. In this section we provide an overview of the theoretical basis and implementation details of several models of increasing usefulness and sophistication, starting with the standard point-dipole approach, continuing with the generalized standardized excitation approach (GSEA) and the normalized surface magnetic source (NSMS) model, and culminating with the orthonormalized volume magnetic source (ONVMS) model. We finish the section by describing a fast, inversion-free method to estimate the number of buried targets and presenting some results for actual EMI data sets.

The most frequently used method for representing the EMI response of a metallic target in both frequency and time domains approximates the whole object with a set of orthogonal co-located point dipoles that fire up in response to the primary field; the induced dipole moment is related to the primary field through a symmetric polarizability tensor. The use of this dipole approximation is motivated by its speed and simplicity; this simplicity, however, rests on assumptions that often become problematic and limit the model's usefulness. One such assumption is that the buried target of interest is either far enough from the transmitter loop, or small enough, that the primary field is essentially uniform throughout its extent. Usually, complex targets composed of different materials and different sections that contribute appreciably to the response—and, in the case of UXO, containing such complicating features as fins and rings—simply cannot be modeled accurately with a single point dipole. Such cases require more advanced methods that will capture the underlying physics correctly. One such technique is the GSEA approach.

The GSEA approach is based generalized standardized excitation approach, for the representing EMI response from heterogeneous and multiple objects, excited by an arbitrary time varying magnetic field. There are two ways to implement the GSEA in practice: 1) the model-based and 2) data-based SEA. The model based approach, that is described in this report requires three steps: 1) Decomposition of a primary magnetic field into spheroidal modes; 2) Solving the full EMI problem via full method of auxiliary sources (MAS) and MAS/ thin-skin-depth approximation (TSA) and 3) Representing the scattered field via reduced sets of sources. The GSEA catches all the complexity of a full, rigorous solution, but cannot be executed quickly enough for application in real field data inversions classification. To overcome this we implemented the NSMS.

The NSMS method [1-4] can be considered as a generalized surface dipole model, and indeed reduces to the point dipole model in a special limiting case. The NSMS approach models an object's response to the primary field of a sensor by distributing a set of equivalent elementary magnetic sources—normally oriented dipoles in this case—over an auxiliary surface that surrounds it. Such a surface distribution can be hypothetically generated by spreading positive magnetic charge over the outer side of the equivalent surface (usually a prolate spheroid) and an identical distribution of opposite sign on its inner side [5], resulting in a double layer of magnetic charge separated by an infinitesimal distance. This double layer introduces the proper discontinuities in the tangential components of the magnetic flux density vector \mathbf{B} but does not affect the transition of its normal component, which must always be continuous given the lack of free magnetic charges in nature. The resulting magnetic-moment distribution radiates a field that by construction satisfies the governing EMI equations and can thus account for the secondary field outside the object. The particulars of location and orientation are divided out by normalizing the dipole density at every point with the component of the primary magnetic field normal to the surface. The resulting surface amplitude Ω of the NSMS distribution is a property of the object, and its integral Q over the surface constitutes a sort of global magnetic polarizability that is independent of the computational constructs—primary field, surrounding surface, object location and orientation, etc.—introduced for its determination. The surface amplitude can be determined directly for library-matching purposes by minimizing the difference between measured and modeled data for a known combination of object and sensor at a given relative location and orientation.

The NSMS technique has demonstrated good computational speed and superior classification performance when applied to EMI datasets consisting of well-isolated single targets, but is found to degrade quickly on both counts when confronted with multi-target cases. This has forced us to generalize the model further and develop the ONVMS procedure.

The ONVMS model, a further extension of NSMS, is based on the assumption that a collection of subsurface objects can be replaced with a set of magnetic dipole sources, distributed over a volume. Since all actual radiating sources are located within the scatterers—rather than in the soil or air—the spatial distribution of these fictitious dipoles (their amplitudes scaled by the primary field) indicates the locations and orientations of any targets present inside the computational volume. The great advantage of the ONVMS technique over the other models discussed above is that it takes into account mutual couplings between different sections of the different targets while simultaneously avoiding the appearance of singular matrices in multi-target situations. It is thus gracefully indifferent to the number of targets: Once the amplitudes and the locations of the corresponding dipoles are determined, one need only look at their clustering patterns, compute the time-dependent total polarizability tensor for each group, and

subsequently diagonalize each such tensor using joint diagonalization (see immediately below for another application). The resulting diagonal elements have been found to be intrinsic to the objects they represent, and can be used, on their own or combined with other quantities, in discrimination analysis. Recent ESTCP live-site discrimination studies have clearly indicated the superior discrimination performance (illustrated in chapter 4) of the ONVMS method.

One of the main challenges one faces when attempting multi-target inversion and classification is the inability to estimate the number of targets. Under this project we implemented a technique based on joint diagonalization that estimates the number of targets present in the field of view of the sensor as it takes a data shot, in real time and without requiring a forward model, and, in a good number of cases, even provides the capability to perform a quick inversion-free characterization and classification of these targets. JD determines the eigenvalues and eigenvectors of a square time- or frequency-dependent multi-static response (MSR) matrix synthesized directly from measured data. The number of nonzero eigenvalues of the matrix (i.e., those above a noise threshold) is related to the number of elementary sources in the illuminated cell; moreover, the time-decay patterns of these non-vanishing eigenvalues are intrinsic properties of the targets to which the sources correspond and can ultimately provide dependable classification features.

2.2 The Generalized Standardized Excitation Approach for UXO discrimination

Distinguishing an object of interest from innocuous items is the main problem that the UXO community is facing currently. This inverse problem demands fast and accurate representation of target EMI response. To some extent, these needs can be satisfied in the case of homogeneous targets by using analytical solutions that have been developed for basic non-spherical shapes [6], [7], and [8]. However, most actual UXO are geometrically complex and materially heterogeneous objects. Both numerical and experimental analyses of EMI responses from heterogeneous objects have demonstrated the strong interaction between different parts of the target [9-12]. Therefore, EMI response for heterogeneous objects cannot in general be represented as the simple sum of signals from each part independently. Using the hybrid full MAS-MAS/TSA, or virtually any other numerical method for a detailed, accurate, and rigorous solution of EMI scattering from complex objects requires from several tens up to several hundreds or thousands of unknowns. This fact makes currently available rigorous 3D-EMI numerical models impractical for the calculations typically required by inversion algorithms. To overcome these issues, this chapter describes a new algorithm called the generalized SEA, for the representing EMI response from heterogeneous and multiple objects, excited by an arbitrary time varying magnetic field.

There are two ways to implement the GSEA in practice: 1) the model-based and 2) data-based SEA. Here we describe both approaches in detail.

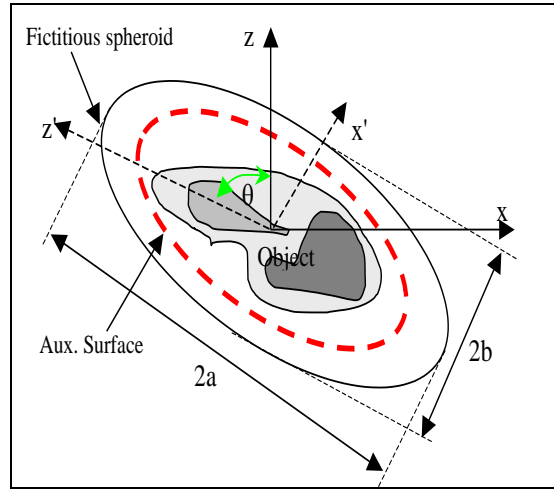


Figure 1: Problem geometry, with additional fictitious spheroid.

2.2.1 The Model Based SEA

The model can be divided into three major steps:

Step #1. Decomposition of a primary magnetic field into spheroidal modes

Let us assume that a heterogeneous object, containing different homogeneous sections, is illuminated by an arbitrarily oriented, time varying primary magnetic field. We surround the object with a fictitious spheroid, which is introduced only as a computational aide in the decomposition of the primary magnetic field into fundamental spheroidal modes. We choose spheroids because they can assume the general proportions of elongated objects of interest, such as UXO, which are also typically bodies of revolution. Oblate spheroids can also be used for flattened shapes. In general, the fictitious surface could be any smooth, closed surface. On the fictitious spheroid given by $\xi = \xi_0$ the primary magnetic field can be expressed as:

$$\mathbf{H}^{\text{pr}} = -\nabla\psi^{\text{pr}} = \sum_{m=0}^{\infty} \sum_{n=m}^{\infty} \sum_{p=0}^1 b_{pmn} \mathbf{H}_{pmn}^{\text{pr}} \quad (1)$$

where $\psi^{\text{pr}} = \left\{ \frac{H_0 d}{2} \sum_{m=0}^{\infty} \sum_{n=m}^{\infty} \sum_{p=0}^1 b_{pmn} P_n^m(\eta) P_n^m(\xi) T_{pm}(\phi) \right\}$, $T_{pm}(\phi) = \begin{cases} \cos(m\phi), & p=0 \\ \sin(m\phi), & p=1 \end{cases}$, in which ψ^{pr} is the primary

field's scalar potential, decomposed into fundamental spheroidal modes as in [6]; (η, ξ, ϕ) are the standard spheroidal coordinates; d is the spheroid's interfocal distance and P_n^m are associated Legendre functions of the first kind, The b_{pmn} are coefficients needed to express the primary field and \mathbf{H}_{pmn}^{pr} is the pmn mode primary magnetic field component when $b_{pmn}=1$.

Step #2: Solving the full EMI problem via full MAS-MAS/TSA

After the primary magnetic field has been decomposed into the pmn spheroidal modes, then the complete solution for the target response to each \mathbf{H}_{pmn}^{pr} field is obtained. In general, these need to be calculated only once and then stored, for all primary fields, i.e. for all sensor-scatterer configurations. To do so, one extends each mode to the physical surface within the enclosing spheroid and applies the above-mentioned full MAS-MAS/TSA method. Finally, the target's response for each primary magnetic field component $b_{pmn} \mathbf{H}_{pmn}^{pr}$ is expressed as:

$$\mathbf{H}_{pmn}^{sc}(\mathbf{r}) = b_{pmn} \sum_{k=1}^N Q_k^{pmn} \mathbf{G}(\mathbf{r}, \mathbf{r}'_k) \quad (2)$$

where Q_k^{pmn} is the amplitude of k^{th} auxiliary magnetic charge, located at \mathbf{r}'_k in the target's domain, corresponding to the response to \mathbf{H}_{pmn}^{pr} ; $\mathbf{G}(\mathbf{r}, \mathbf{r}'_k)$ is the magnetic field produced by a unit value of the k^{th} magnetic charge; and N is the number of auxiliary magnetic charges. Using Q_k^{pmn} for each fundamental mode, the total response at any point outside the scatterer can be represented as:

$$\mathbf{H}^{sc}(\mathbf{r}) = \sum_{m=0}^{\infty} \sum_{n=m}^{\infty} \sum_{p=0}^1 b_{pmn} \sum_{k=1}^N Q_k^{pmn} \mathbf{G}(\mathbf{r}, \mathbf{r}'_k) \quad (3)$$

Thus, after pre-computation of Q_k^{pmn} coefficients for any given object, the EMI scattering problem for any particular 3-D configuration breaks down merely to determining spheroidal modal expansion coefficients b_{pmn} .

Step #3: Representing the scattered field via reduced sets of sources

In the full MAS-MAS/TSA calculations mentioned above, considerable resolution is required to enforce the boundary conditions in detail over the physical boundary. That is, some substantial number of sources Q_k is required to represent the scattered magnetic field outside the object (including its physical surface). We can re-express that field quite accurately for observation points outside an enclosing fictitious spheroid, using a much smaller number of sources (Figure 1). The distance between the

additional spheroid and the object's surface is typically some significant fraction of the object's characteristic dimensions, but is smaller than the distance to any contemplated observation point. Thus, for each input pmn spheroidal mode, the amplitudes of a reduced source set (RSS) $[q^{pmn}]$ are determined by solving the following linear system of equations:

$$[g][M^{pmn}] = [\psi_{pmn}^{sc}(\mathbf{r}_j)], \quad (4)$$

where

$$g(\mathbf{r}_j, \mathbf{r}'_i) = \frac{(\mathbf{r}_j - \mathbf{r}'_i) \cdot \hat{\mathbf{n}}_i}{4\pi\mu_o |\mathbf{r}_j - \mathbf{r}'_i|} \quad (5)$$

and $g(\mathbf{r}_j, \mathbf{r}'_i)$ is the potential at the \mathbf{r}_j observation point produced by the i^{th} point magnetic dipole at \mathbf{r}'_i on the inner auxiliary surface and oriented along $\hat{\mathbf{n}}_i$ unit normal vector. $\psi_{pmn}^{sc}(\mathbf{r}_j)$ is the scalar potential at \mathbf{r}_j for the pmn mode with $b_{pmn} = 1$. The $[q^{pmn}]$ sources completely determine the scattered field outside the fictitious spheroid. Using magnetic charges Q_k^{pmn} obtained by solving the full EMI boundary value problem, $\psi_{pmn}^{sc}(\mathbf{r}_j)$ can be expressed as:

$$\psi_{pmn}^{sc}(\mathbf{r}_j) = \sum_{k=1}^N Q_k^{pmn} \frac{1}{4\pi\mu_o |\mathbf{r}_j - \mathbf{r}'_k|} \quad (6)$$

and the complete secondary magnetic field can be represented as:

$$\mathbf{H}^{sc}(\mathbf{r}) = \sum_{m=0}^{\infty} \sum_{n=m}^{\infty} \sum_{p=0}^1 b_{pmn} \sum_{i=1}^{N_{red}} M_i^{pmn} \bar{\bar{\mathbf{G}}}(\mathbf{r}, \mathbf{r}_i). \quad (7)$$

where $\bar{\bar{\mathbf{G}}}(\mathbf{r}, \mathbf{r}_i) = -\nabla g(\mathbf{r}, \mathbf{r}_i)$.

Note that, while we may ultimately be able to express the scattered field using a small number of sources, this is a fundamentally different strategy from what has been applied heretofore in the simple independent dipole models. In the latter, each source responds only to the primary field striking it locally. Here, however, the M_i^{pmn} , $i=1,2,\dots,N_{red}$ act together not in response to local stimuli, but to express the response of the entire object to the distributed excitation of the pmn mode. Using the full MAS-MAS/TSA numerical code the q_i^{pmn} can be generated and stored for any number of pmn spheroidal modes in infinite series (7). Once this is done, then the truncation criterion can be determined from the input primary magnetic field.

2.2.2 Efficient calculation of spheroidal modal expansion coefficients

Using the method outlined above, one can obtain a great many forward solutions quickly during an inversion search through many prospective scatterer – sensor configurations. One need only determine the b_{pmn} required for the primary field implied by each configuration. In a typical inversion, this must be done many times, hence its efficiency is important.

Previously the b_{pmn} were determined via relationships in terms of magnetic scalar potential [8, 9]. While this is sensible when the problem proceeds in terms of potential, one must often work in terms of the magnetic field itself, as it is in numerical enforcement of boundary conditions. Further, calculation of the potential is not always straightforward. EMI sensors, typically, consist of wire loops and as the applicable Biot-Savart law provides magnetic field, not potential, some indirection is required. Using this approximation together with orthogonality relationships between the associated Legendre functions, one can express the b_{pmn} explicitly in terms of an integral of the primary field over a surrounding spheroidal surface. The time required for that double integration is a concern in repetitive inversion calculations.

To avoid the surface integral, in reference [13] the authors obtain a system to solve for the b_{pmn} coefficients by point matching over the spheroid, proceeding in terms of the primary magnetic field potential. Here, we retain the surface integral but apply an efficient quadrature. Also, instead of the scalar magnetic field potential, we proceed directly in terms of the normal component of the primary magnetic field on the fictitious spheroid to obtain the algebraic system for computing the b_{pmn} coefficients. From equation (7), the normal component H_{nor}^{pr} of the primary magnetic field can be expressed as:

$$H_{nor}^{pr}(\eta, \xi_o, \phi) = -\frac{H_o d}{2h_{\xi_o}} \sum_{m=0}^{\infty} \sum_{n=m}^{\infty} \sum_{p=0}^1 b_{pmn} P_n^m(\eta) P_n^m(\xi_o) T_{pm}(\phi) \quad (8)$$

where $P_n^m(\xi_o) = \left. \frac{dP_n^m(\xi)}{d\xi} \right|_{\xi=\xi_o}$ is a derivative of the associated Legendre function evaluated on the

$\xi = \xi_o$ spheroidal surface. Based on the orthogonality properties of the associated Legendre and trigonometric functions, the b_{pmn} coefficients are:

$$b_{pmn} = -\frac{2n+1}{\alpha \pi H_o d} \frac{(n-m)!}{P_n^m(\xi_o) (n+m)!} \int_{-1}^1 P_n^m(\eta) \int_0^{2\pi} h_{\xi_o} H_{nor}^{pr}(\eta, \xi_o, \phi) d\eta d\phi \quad (9)$$

where $\alpha = 2$ for $m = n = 0$ and $\alpha = 1$ otherwise.

Overall, the entire SEA approach can be described briefly as follows:

1. For a given UXO item, amplitudes of responding magnetic dipoles M_i^{pmn} $i = 1, 2, \dots, N_{\text{red}}$ rings are determined and sorted in the universal library for any number of basic spheroidal mode excitations $pmn = 1, 2, \dots$
2. Once step 1 is complete, then for a given sensor, the primary field is decomposed into spheroidal modes, the spheroidal modal decomposition b_{pmn} coefficients are calculated, and the necessary number of spheroidal modes is determined.
3. Use reduced set of sources (RSS) M_i^{pmn} to calculate EMI response for each pmn -th basic excitation. Scale each pmn -EMI response on the b_{pmn} coefficients and calculate the target's complete response by superimposing responses of each basic excitation.

The GSEA, which is based on the MAS-TSA and introduced here, can produce a target's ultra-wideband frequency response. Thus, the proposed GSEA can be used directly to obtain an object's TD EMI responses via convolution theorem without recalculating amplitudes of the responding sources. This makes the GSEA a unified model to treat both FD and TD data, and is attractive from a practical point of view, thus many state-of-the-art EMI sensors (EM-63, EM-61, Zonge NanoTEM) are operating in TD.

Let us briefly describe the important formulas required to compute the TD EMI response for a general current waveform $I(t)$ flowing in a transmitter loop. By using the convolution theorem the induced voltage in the receiver coil can be expressed as

$$\frac{dB}{dt} = -\int_0^t A'(t-\tau)I'(\tau)d\tau - A(0)I'(t) - A'(t)I(0), \quad (10)$$

where $A(t)$ represents an object's impulse response and the prime means the derivative with respect to time t . Equation represents the TD response of an object to a general excitation current $I(t)$ source.

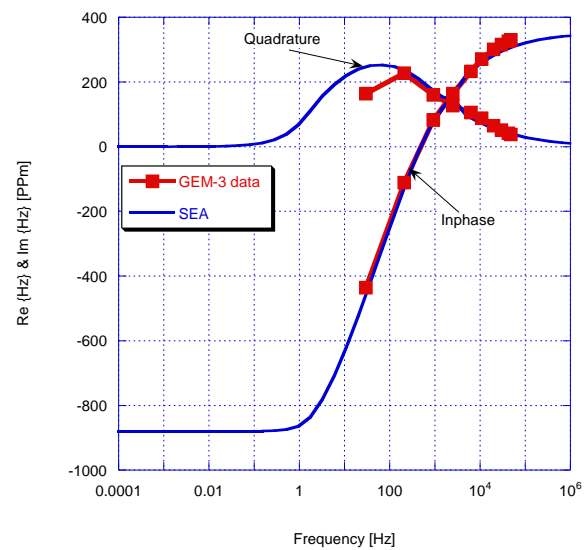
2.2.3 Numerical results: The universal RSS

This section presents some numerical and experimental data that demonstrate the GSEA as a unified model for any FD or TD sensor configuration, and its applicability to complex data sets: novel waveforms, multi-axis, vector, or tensor magnetic, or electromagnetic induction data, or any combination of magnetic and EMI data; and ability to take into account the influence of conductive and magnetically susceptible geological soils on metal detectors.

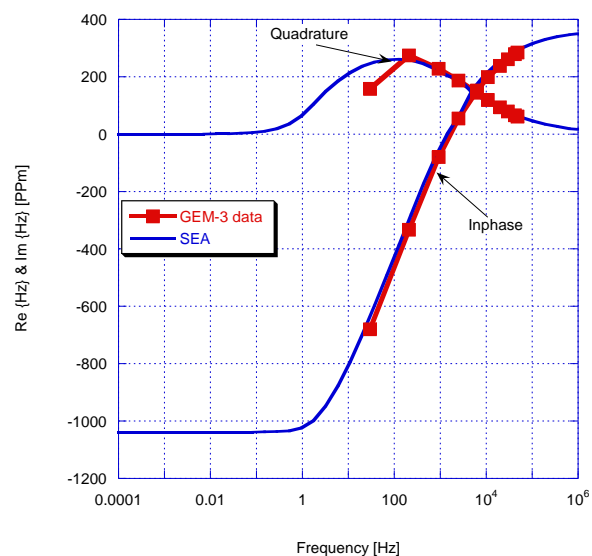


FD

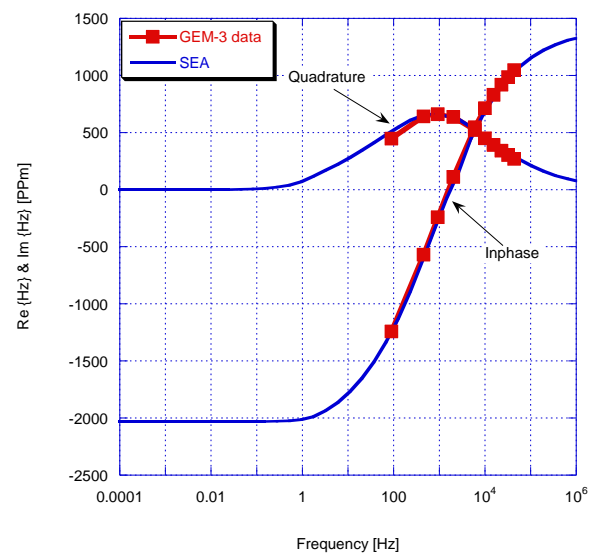
a)



b)



c)



d)

Figure 2: Frequency-domain EMI response for 81 mm UXO; (a) GEM-3 excitation; (b) nose up vertical, (c) nose up 45° inclination, (d) horizontal.

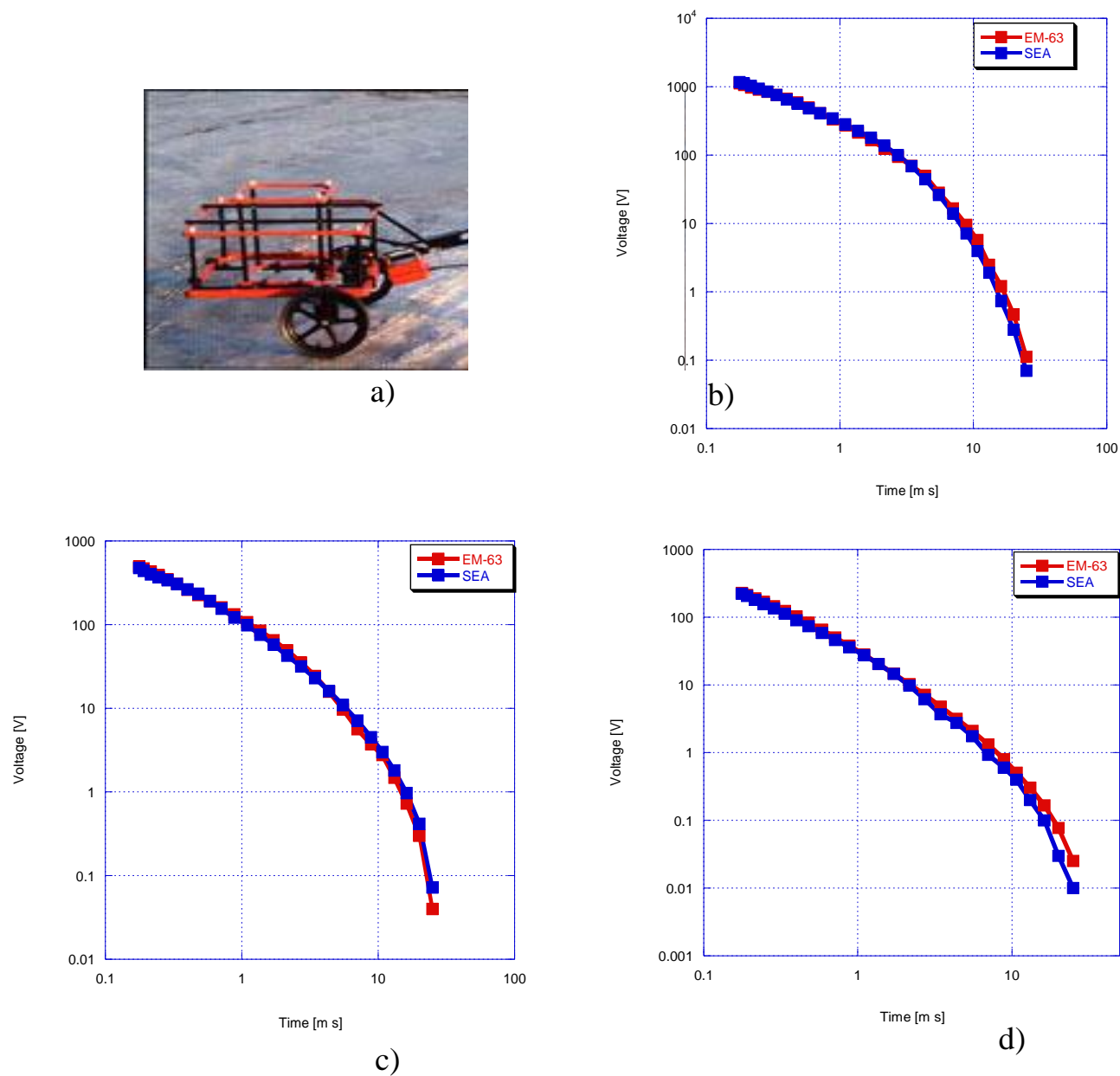


Figure 3: Time-domain EMI response for 81-mm UXO; (a) EM-3 excitation; (b) nose up vertical, (c) nose up 45° inclination, (d) horizontal.

As discussed above, the reduced source set (RSS) M_i^{pmn} in Eq. (8) depends only on the target's geometry and electromagnetic properties. To validate such a unique characteristic of the RSS, here comparisons between RSS modeled and experimental data are given for an actual UXO (81 mm) in both FD and TD. The data were collected by two EMI systems that are widely used in the UXO discrimination community: (1) a wideband frequency-domain sensor (GEM-3) developed by Geophex Ltd. and (2) a time-domain instrument (EM-63) developed by Geonics. The data were collected on the U.S. Army Engineer Research and Development Center test stand site.

Figure 2 shows the comparisons between GSEA and actual data in the frequency domain. In this case data were collected for the UXO oriented in three different directions relative to the GEM-3 sensor head: (1) vertical tail up, (2) 45° degree nose up, and (3) transverse. The GEM-3 frequency range is from 30 Hz to 50 kHz. The comparisons between measured and actual experimental data are in very good agreement for all orientations. Note that the RSS produces results in an ultra-wideband frequency range, from magneto-static (0 Hz) to the EMI frequency limit. This allows users to accurately compute the scattered field at any required frequencies by simple interpolation and to obtain EMI responses readily in TD via inverse Fourier transforms. To illustrate this capability, here the first impulse responses in TD are evaluated by applying the digital filter technique to the inverse sine transform as follows:

$$A(t) = \frac{2}{\pi} \int_0^\infty \text{Im } B(\omega) \sin \omega t \, d\omega \quad (11)$$

where $\text{Im } B(\omega)$ represents an imaginary part of the magnetic flux that is calculated via RSS. Then the induced voltage is calculated using the time convolution technique (10).

In the EM-63 instrument, the current waveform consists of an exponential current increase followed by a linear ramp off. The current has three pulses per measurement. For comparisons between RSS and TD data, here the same 81-mm UXO is chosen. The object was excited from three: (1) vertical tail up, (2) 45° degree nose up, and (3) transverse orientations. For all three excitations, the vertical distance between the sensor's transmitter loop and the center of the cylinder is $h = 60.00$ cm. The TD induced voltage is calculated by an inverse Fourier transform of the frequency-domain magnetic field flux using equations (10) and (11). The comparisons are depicted in Figure 3. They show very good convergence between the measured and modeled TD data. Therefore, the universal RSS accurately produces EMI responses for a given target for any sensor in FD and TD domains.

In this chapter, the generalized standardized excitation approach, which is a fast, universal, and rigorous forward modeling system, has been developed and demonstrated. The GSEA is applicable to any FD or TD sensor configuration, and to any data set: novel waveforms, multi-axis, vector and tensor, or

magnetic or electromagnetic induction data, or any combination of magnetic and EMI data. By using an appropriate dyadic Green's function the GSEA takes into account a host medium. EMI response from a magnetically susceptible half-space is analyzed versus sensor height and frequency. Numerical tests show that a frequency-dependent, magnetically susceptible half-space significantly affects the 81-mm UXO's EMI responses in both FD and TD. This study suggests that a magnetically susceptible host medium must be taken into account in UXO discrimination problems.

2.2.4 Data derived generalized SEA applied to MPV TD data

In this section, the data-derived GSEA is utilized for EMI sensors to enhance UXO discrimination. The key element in the GSEA is to determine the amplitudes of the responding sources, which are characteristic of the object and are independent of sensor type, object location and orientation, and transmitted waveform. In this chapter we outline the numerical procedure for determining the amplitudes of the GSEA directly from the EMI sensor data. The applicability of the GSEA to FD and TD data is demonstrated by comparing the GSEA modeled data to actual TD and FD data that were collected at the US Army ERDC test-stand site. The most straightforward way to determine the amplitudes of the responding magnetic dipole sources is to solve a standard inverse problem based on the measured data. Obviously, this process requires very good experimental conditions and a sufficient number of independent measurements of an object of interest in order to reduce the degree of ill-posedness. Recently [14], applied such a data-derived approach to extracting the modal response coefficients, which were magnetic charges, for each candidate by carefully designing the measurements at different distances and orientations in free space using the frequency domain GeoPhex Inc GEM-3 sensor. Here, the data-derived GSEA, which uses magnetic dipoles instead of magnetic charges, is applied to the new MPV-TD data.

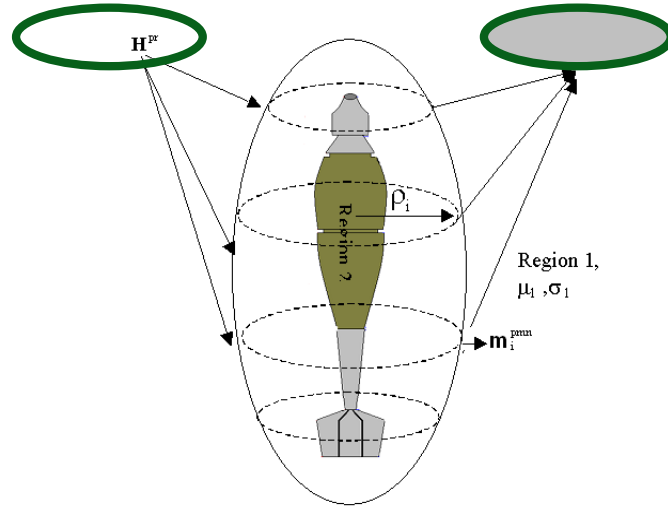


Figure 4: Problem geometry and reduced set of sources $\mathbf{p}_i^{\text{pmn}}$ distributed along rings on the spheroid surface.

Recently, the SEA based on the fictitious magnetic charges has been developed and applied to UXO discrimination using both frequency and time domain EMI data [14]. Here, the GSEA, which is based on the magnetic dipoles as responding sources, is extended to both FD and TD EMI sensors data. Notice, that the GSEA is applicable for free space as well as for a conducting and magnetically susceptible host media. To illustrate the GSEA for EMI sensor, let us assume that an object placed in a free space Figure 4. The object is illuminated by an arbitrarily oriented, time varying primary magnetic field. In the EMI frequency regime, displacement currents within and outside the object are assumed to be zero, i.e. both the scattered and primary magnetic fields are irrotational. We surround the object with a fictitious spheroid, which is introduced only as a computational aide in the decomposition of the primary magnetic field into fundamental spheroidal modes. We choose spheroids because they can assume the general proportions of elongated objects of interest, such as UXO, which are also typically bodies of revolution (BOR). Oblate spheroids can also be used for flattened shapes. In general, the fictitious surface could be any smooth closed surface, as applicable for a related standardized source set approximation described in [9, 15]. On the fictitious spheroid given by $\xi = \xi_0$ (Figure 4), the primary magnetic field can be expressed as in equation (2.1).

After the primary magnetic field is decomposed into the pmn spheroidal modes, then the complete solution for the target to each $\mathbf{H}_{\text{pmn}}^{\text{pr}}$ field can be obtained. Finally, the target's full response is:

$$\mathbf{B}^{\text{sc}}(\mathbf{r}, t) = \nabla \times \sum_{m=0}^{\infty} \sum_{n=m}^{\infty} \sum_{p=0}^1 b_{\text{pmn}} \mathbf{A}_{\text{pmn}}^{\text{sc}}(\mathbf{r}, t) = \nabla \times \mathbf{A}^{\text{sc}}(\mathbf{r}, t) \quad (12)$$

$$\mathbf{A}_{pmn}^{sc}(\mathbf{r}, t) = \frac{\mu_o}{4\pi} \int_{S_{sph}} \frac{\mathbf{m}_{pmn}(\mathbf{r}', t) \times \mathbf{R}}{R^3} d\mathbf{s}' \quad (13)$$

where \mathbf{A}_{pmn}^{sc} is the pmn mode of the scattered vector potential, the $\mathbf{A}^{sc}(\mathbf{r}, t)$ is the total scattered potential, $\mathbf{m}_{pmn}(\mathbf{r}', t)$ are responding magnetic dipoles that are distributed on the fictitious spheroidal surface, \mathbf{r} and \mathbf{r}' are the observation and sources points' radius vectors respectively, and $\mathbf{R} = \mathbf{r} - \mathbf{r}'$. Note that in the EMI range, the secondary magnetic field is irrotational, which means that the scattered field propagates outside the object simultaneously i.e. there is no time delay in equation (12). By using the Green's function, the scattered magnetic field is approximated by a set of magnetic dipoles that are oriented normal to the fictitious spheroidal surface (Figure 4), i.e.:

$$\mathbf{m}_{pmn}(\mathbf{r}', t) = \mathbf{M}_{pmn}(\mathbf{r}', t) \cdot \hat{\mathbf{n}}(\mathbf{r}') \quad (14)$$

where $\hat{\mathbf{n}}(\mathbf{r}')$ is normal at \mathbf{r}' point on the spheroidal surface, and $\mathbf{M}_{pmn}(\mathbf{r}', t)$ are the amplitudes of the responding sources. The MPV TD sensor, as well as many other EMI sensors, measures time derivatives of the magnetic flux over the receiver coils, as

$$\text{Signal} = \int_{S_r} \frac{\partial \mathbf{B}^{sc}(\mathbf{r}, t)}{\partial t} d\mathbf{s}' = \frac{\partial}{\partial t} \int_{S_r} \text{rot } \mathbf{A}^{sc}(\mathbf{r}, t) d\mathbf{s}' = \frac{\partial}{\partial t} \oint_L \mathbf{A}_\ell^{sc}(\ell', t) d\ell' \quad (15)$$

After taking equations (12) and (14) into (15),

$$\text{Signal} = \oint_L \left[\sum_{m=0}^{\infty} \sum_{n=m}^{\infty} \sum_{p=0}^1 b_{pmn} \int_{S_{sph}} \frac{\partial \mathbf{M}_{pmn}(\mathbf{r}', t)}{\partial t} \cdot \mathbf{G}(\mathbf{r}', \mathbf{r}) d\mathbf{s}' \right] d\ell' \quad (16)$$

where

$$\mathbf{G}(\mathbf{r}', \mathbf{r}) = \frac{\mu_o}{4\pi} \frac{\hat{\mathbf{n}}(\mathbf{r}') \times \mathbf{R}}{R^3} \quad (17)$$

where $\frac{\partial \mathbf{M}_{pmn}(\mathbf{r}', t)}{\partial t} = \mathbf{M}'_{pmn}(\mathbf{r}', t)$ is a time derivatives of the amplitudes of the responding magnetic dipoles that need to be determined from the actual measured data.

Since many, if not all UXO are BOR, it is desirable to simplify equation (16) for BOR objects. After dividing the fictitious spheroid surface into J belts (Figure 4), and taking into account the object's BOR symmetry, the amplitude of the responding $\mathbf{M}'_{pmn}(\mathbf{r}', t)$ source around each j^{th} belt can be

expanded into a Fourier series with respect to the azimuthal ϕ angle, and equation (16) can be rewritten as:

$$\text{Signal}(\mathbf{r}) = \oint_L \left[\sum_{m=0}^{\infty} \sum_{n=m}^{\infty} \sum_j^J M_j'^{mn}(\rho_j, t) \sum_{p=0}^1 \int_{\Delta S_{\text{sph}}^j} (b_{0mn} \cos(m\phi) + b_{1mn} \sin(m\phi)) \cdot \mathbf{G}(\mathbf{r}_j', \mathbf{r}) ds' \right] d\ell' \quad (18)$$

Finally, the EMI scattered fields from all J belts is set to equal the measured signal at \mathbf{r} point that is a known field arising from the scatterer. For \mathbf{r}_k , $k=1, 2, \dots, K$ points, equation (8) leads to a linear system of equations that can be solved by using a well developed least square minimization algorithm. Overall, the entire data derived GSEA approach can be described briefly as follows: first, for a given UXO, detailed, very well controlled data are collected. Then, the amplitudes of the responding magnetic dipoles are determined from actual data and sorted into a library for some number of basic spheroidal pmn mode excitations. Finally, for a given sensor, the primary field is decomposed into spheroidal modes, the spheroidal modal decomposition b_{pmn} coefficients are calculated, each of the object's pmn EMI responses are scaled by the b_{pmn} coefficients, and the target's complete response is calculated by just superimposing responses of each basic excitation.

2.2.5 Numerical results for the DATA-Derived GSEA

a) Vector TD data

In this section, all subsequent studies are done for the new MPV TD sensor made by G&G Sciences Inc. The MPV TD sensor consists of two transmitter loops with 37.5 cm radii and five triaxial receiver loops/cubes (Figure 5).

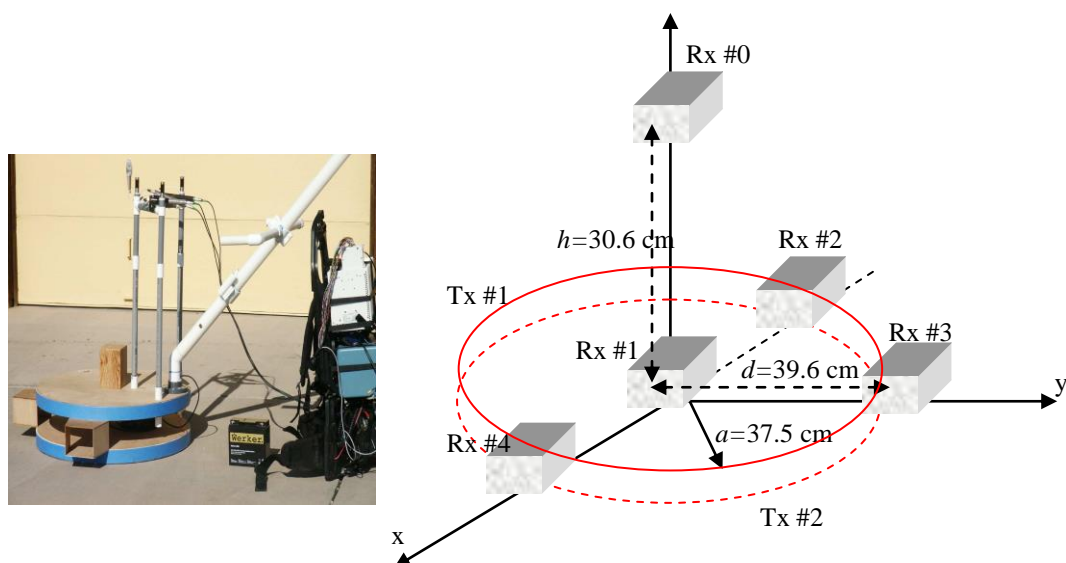


Figure 5: Actual and schematic diagram of the MPV-TD sensor.

The receivers are located: cube #0 upper center, cube #1 lower center; cube #2: left ($x = -39.6$ cm); Cube #3: forward ($y = 39.6$ cm); Cube #4: right at $x = 39.6$ cm. These receivers accurately measure the complete transient response over a wide dynamic range of time from $100\mu\text{s}$ to 25ms . The measurements were conducted at the UXO test-stand at the U.S. Army Engineer Research and Development Center Laboratory, Vicksburg, MS. The measurement platform, which is made with nonmetallic fiberglass material, has a usable measurement area of 3×4 m. The sensor is mounted on a robotic arm that can be moved and controlled around the measurement area using software running on a personal computer. Automated remote controls are used to position an ordnance item at an accurate depth (to within 1 cm) below the measurement area. The sensor can be positioned with an accuracy of approximately 1 mm. All data presented here were collected by G&G Sciences Inc, personnel. The data were collected on an 89 point grid for objects at different orientations and depths. The response of each object was represented only with five magnetic dipole belts, with $m=0,1,2$, and $n=m, \dots, 6$ and the spheroidal modes all together total 42 responding sources. Figure 6 shows comparisons between modeled and actual data at fixed time gates for x - and z - components of the scattered magnetic fields for five receivers. The results clearly shows that the GSEA predicts 60mm UXO EMI responses very well.

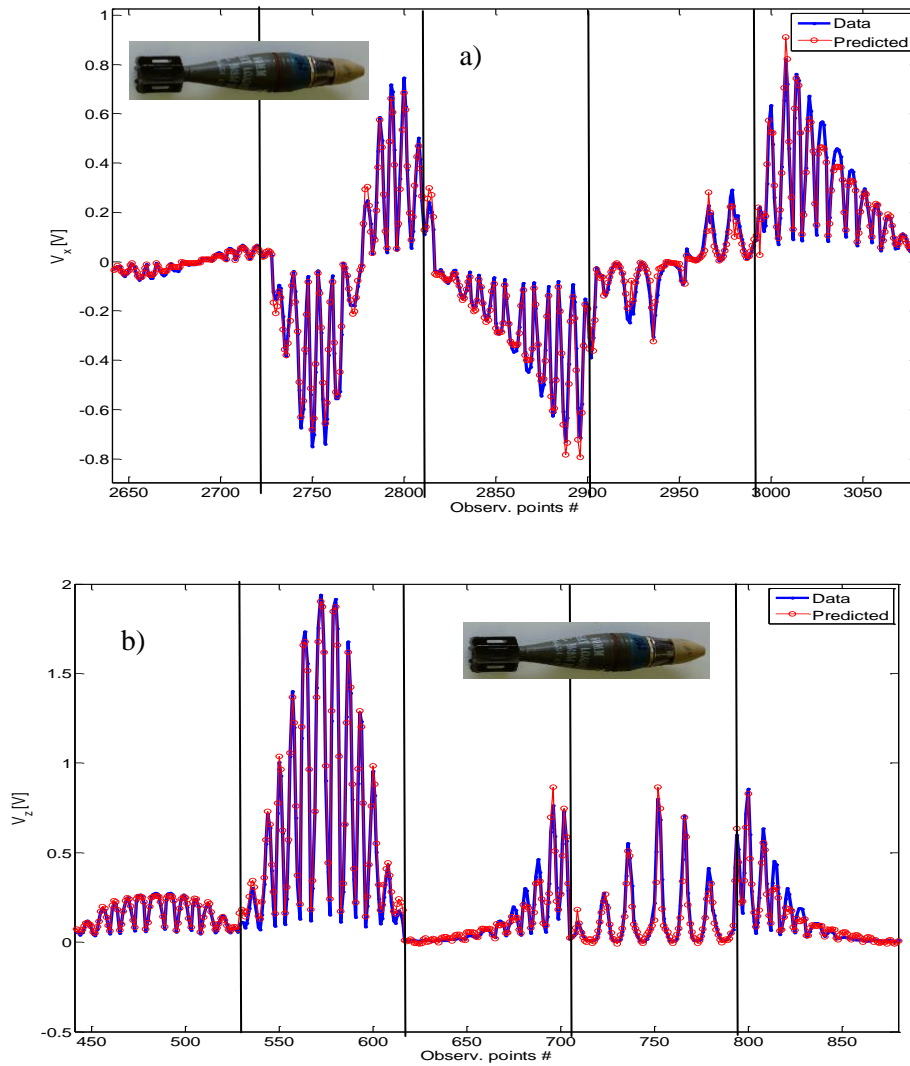


Figure 6: The measured and modeled scattered magnetic field flux at given time channel versus observation points; A) Hx magnetic field flux; b) Hz magnetic field flux

b) Scalar FD data

Similar tests were done for FD EMI data using GEM-3 sensor. The data were collected at CRREL over ATC-set UXO at different location and orientations. The comparisons between actual and measured data are given in Figure 7. Results are in excellent agreement over entire the frequency band.

In this section, the data-derived GSEA that is based on using magnetic dipoles instead of magnetic charges, has been applied to new MPV TD and GEM-3 data. The magnetic flux over the receiver coils is calculated using the vector potential which reduces the prior surface integration to a closed loop integration with a simple integrand. The method is applicable for novel waveforms, multi-axis and vector receivers, and tensor or magnetic or electromagnetic induction data, or any combination. There is excellent agreement between the GSEA and experimental data. In future work, we will apply the method to magnetic and EMI data. The method has been tested against actual data, and we have demonstrated its effectiveness in UXO discrimination tests.

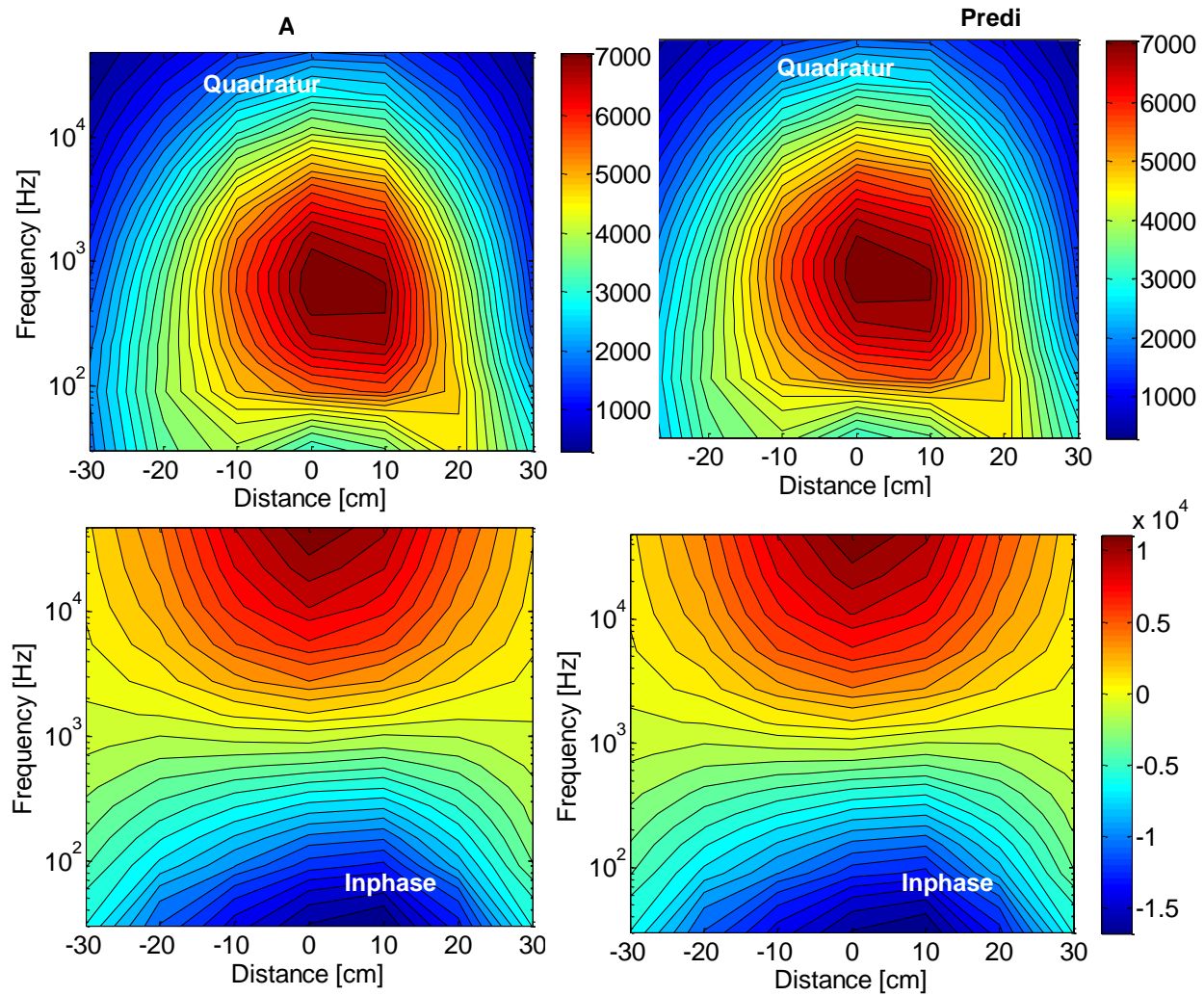


Figure 7: The measured and modeled scattered magnetic field versus frequency and distance

2.3 The single-dipole approximation

According to the Huygens Equivalence Principle, an object's entire response to a given excitation can be approximated as the summation of magnetic fields produced by elementary magnetic dipoles/charges placed on a closed surface surrounding the target. Using the superposition principle, this set of dipoles can be approximated as one independent aggregate dipole. In the simple dipole model, the secondary magnetic field at \mathbf{r} due to a dipole of moment \mathbf{m} is:

$$\mathbf{H} = \frac{1}{4\pi R^3} (3\hat{\mathbf{R}}\hat{\mathbf{R}} - \bar{\mathbf{I}}) \cdot \mathbf{m} \equiv \bar{\mathbf{G}} \cdot \mathbf{m} \quad (19)$$

where $\hat{\mathbf{R}}$ is the unit vector along $\mathbf{R} = \mathbf{r}' - \mathbf{r}_d$, \mathbf{r}_d is the dipole's position, and $\bar{\mathbf{I}}$ is the identity dyad (see Figure 8). The dipole moment \mathbf{m} induced by the primary magnetic field \mathbf{H}^{pr} is given by

$$\mathbf{m} = \bar{\mathbf{M}} \cdot \mathbf{H}^{\text{pr}}(\mathbf{r}', \mathbf{r}_d), \quad (20)$$

where $\bar{\mathbf{M}}$, the target's magnetic polarizability tensor, is a symmetric matrix: $\mathbf{M}_{\alpha\beta} = \mathbf{M}_{\beta\alpha}$, $\alpha, \beta = x, y, z$. This tensor depends on the scatterer's shape, size, and material properties. In a coordinate system aligned with the scatterer's principal axes for different primary magnetic fields $\mathbf{H}^{\text{pr}}(\mathbf{r}, \mathbf{r}_d)$, (20) can be written in matrix form as

$$[\mathbf{m}] = \bar{\mathbf{M}} \cdot [\mathbf{H}^{\text{pr}}]. \quad (21)$$

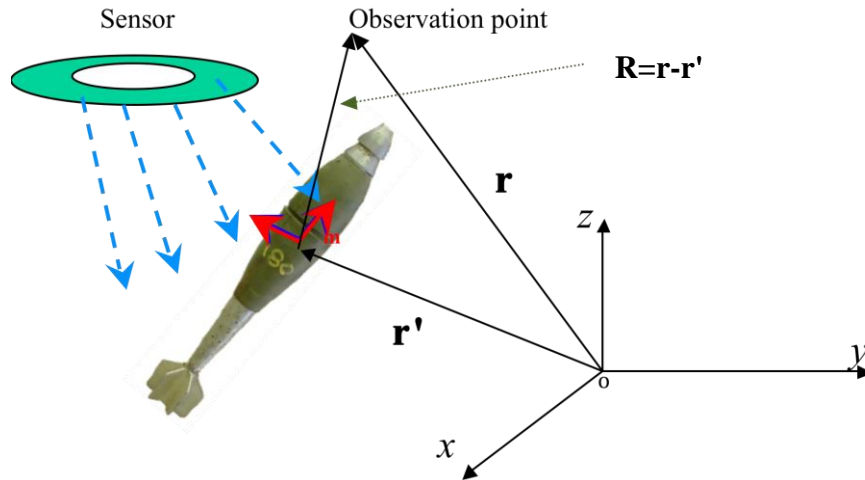


Figure 8: A dipole's location in a global coordinate system.

Thus the secondary magnetic field is

$$\mathbf{H} = \bar{\bar{\mathbf{G}}} \cdot \bar{\bar{\mathbf{M}}} \cdot [\mathbf{H}^{\text{pr}}] \equiv [\bar{\bar{\mathbf{Y}}}] \cdot [\mathbf{M}]^T, \quad (22)$$

where $[\mathbf{M}]$ is a 1×6 dimensional vector whose components ($M_{xx}, M_{xy}, M_{xz}, M_{yy}, M_{yz}, M_{zz}$) correspond to the elements of the target's magnetic polarizability tensor $\bar{\bar{\mathbf{M}}}$ and $[\bar{\bar{\mathbf{Y}}}]$ is a 3×6 matrix,

$$\bar{\bar{\mathbf{Y}}} = \frac{1}{4\pi R^5} \begin{pmatrix} \Upsilon_{11} & \Upsilon_{12} & \Upsilon_{13} & \Upsilon_{14} & \Upsilon_{15} & \Upsilon_{16} \\ \Upsilon_{21} & \Upsilon_{22} & \Upsilon_{23} & \Upsilon_{24} & \Upsilon_{25} & \Upsilon_{26} \\ \Upsilon_{31} & \Upsilon_{32} & \Upsilon_{33} & \Upsilon_{34} & \Upsilon_{35} & \Upsilon_{36} \end{pmatrix}, \quad (23)$$

whose elements are as follows:

$$\begin{aligned} \Upsilon_{11} &= H_x^{\text{pr}} (3R_x^2 - R^2) & \Upsilon_{12} &= 3R_x (R_x H_y^{\text{pr}} + R_y H_x^{\text{pr}}) - H_y^{\text{pr}} R^2 & \Upsilon_{13} &= 3R_x (R_x H_z^{\text{pr}} + R_z H_x^{\text{pr}}) - H_z^{\text{pr}} R^2 \\ \Upsilon_{14} &= 3R_x R_y H_y^{\text{pr}} & \Upsilon_{15} &= 3R_x (R_y H_z^{\text{pr}} + R_z H_y^{\text{pr}}) & \Upsilon_{16} &= 3R_x R_z H_z^{\text{pr}} \\ \Upsilon_{21} &= 3R_y R_x H_x^{\text{pr}} & \Upsilon_{22} &= 3R_y (R_x H_y^{\text{pr}} + R_y H_x^{\text{pr}}) - H_x^{\text{pr}} R^2 & \Upsilon_{23} &= 3R_y (R_x H_z^{\text{pr}} + R_z H_x^{\text{pr}}) \\ \Upsilon_{24} &= H_y^{\text{pr}} (3R_y^2 - R^2) & \Upsilon_{25} &= 3R_y (R_y H_z^{\text{pr}} + R_z H_y^{\text{pr}}) - H_z^{\text{pr}} R^2 & \Upsilon_{26} &= 3R_y R_z H_z^{\text{pr}} \\ \Upsilon_{31} &= 3R_z R_x H_x^{\text{pr}} & \Upsilon_{32} &= 3R_z (R_x H_y^{\text{pr}} + R_y H_x^{\text{pr}}) & \Upsilon_{33} &= 3R_z (R_x H_z^{\text{pr}} + R_z H_x^{\text{pr}}) - H_x^{\text{pr}} R^2 \\ \Upsilon_{34} &= 3R_z R_y H_y^{\text{pr}} & \Upsilon_{35} &= 3R_z (R_y H_z^{\text{pr}} + R_z H_y^{\text{pr}}) - H_y^{\text{pr}} R^2 & \Upsilon_{36} &= H_z^{\text{pr}} (3R_z^2 - R^2) \end{aligned}$$

Once the vector \mathbf{M} is determined the magnetic polarizability tensor $\bar{\bar{\mathbf{M}}}$ is constructed as

$$\bar{\bar{\mathbf{M}}} = \begin{pmatrix} M_{xx} & M_{xy} & M_{xz} \\ M_{xy} & M_{yy} & M_{yz} \\ M_{xz} & M_{yz} & M_{zz} \end{pmatrix}, \quad (24)$$

and finally the $\bar{\bar{\mathbf{M}}}$ tensor's principal polarizability elements are determined in the target frame coordinate system, which is related to the global coordinate system via the Euler rotation tensor $\bar{\bar{\mathbf{A}}}(\psi, \theta, \phi)$, as

$$\bar{\bar{\mathbf{M}}} = \bar{\bar{\mathbf{A}}} \bar{\bar{\boldsymbol{\beta}}} \bar{\bar{\mathbf{A}}}^T \equiv \bar{\bar{\mathbf{A}}} \begin{pmatrix} \beta_{xx} & 0 & 0 \\ 0 & \beta_{yy} & 0 \\ 0 & 0 & \beta_{zz} \end{pmatrix} \bar{\bar{\mathbf{A}}}^T. \quad (25)$$

Body-of-revolution (BOR) symmetry (which most UXO possess) dictates that $\beta_{xx} = \beta_{yy}$ and that the third Euler angle ψ is zero. We thus obtain

$$\bar{\bar{\mathbf{A}}} = \begin{bmatrix} \cos \theta \cos \phi & \cos \theta \sin \phi & -\sin \theta \\ -\sin \phi & \cos \phi & 0 \\ \sin \theta \cos \phi & \sin \theta \sin \phi & \cos \theta \end{bmatrix}, \quad (26)$$

where θ and ϕ are the angles between the local and global axes. Note that the tensor $\bar{\bar{\mathbf{M}}}$ depends on time or frequency while the Euler tensor does not. This suggests that one could apply joint diagonalization (along the lines of the procedure introduced in Section 2.6) to separate the polarizability eigenvalues from the rotational eigenvectors; the attitude angles can in turn be extracted from the latter.

2.4 Normalized surface magnetic source model

2.4.1 Governing equations

Outside the objects of interest, both the primary and the secondary magnetic fields in air and ground (\mathbf{H}^{pr} and \mathbf{H}^{sc} respectively, both measured in A/m) are irrotational and can be represented by scalar magnetic potentials (with dimensions of current) through

$$\mathbf{H}^{\text{out}} \equiv \mathbf{H}^{\text{pr}} + \mathbf{H}^{\text{sc}} = -\nabla \psi^{\text{out}} = -\nabla \psi^{\text{pr}} - \nabla \psi^{\text{sc}}. \quad (27)$$

Inside a metallic target the EMI field is governed by a diffusion equation and can be expressed as

$$\mathbf{H}^{\text{in}} = \frac{1}{\mu^{\text{in}}} \nabla \times \mathbf{A}^{\text{in}}, \quad (28)$$

where the vector potential \mathbf{A} (also with dimensions of current) obeys

$$\nabla \times \left(\frac{1}{\mu^{\text{in}}} \nabla \times \mathbf{A}^{\text{in}} \right) + \sigma^{\text{in}} \frac{\partial \mathbf{A}^{\text{in}}}{\partial t} = 0, \quad (29)$$

and $\mu^{\text{in}} = \mu_r^{\text{in}} \mu_0$; $\mu_0 = 4\pi \cdot 10^{-7}$ [H/m] and σ^{in} are respectively the magnetic permeability and the electric conductivity of the object.

The total interior and exterior magnetic fields are connected at the surface of an object by the customary boundary conditions

$$\begin{aligned}\hat{\mathbf{n}} \times (\mathbf{H}^{\text{pr}} + \mathbf{H}^{\text{sc}}) &= \hat{\mathbf{n}} \times \mathbf{H}^{\text{in}}, \\ \hat{\mathbf{n}} \cdot \mu_r^{\text{out}} (\mathbf{H}^{\text{pr}} + \mathbf{H}^{\text{sc}}) &= \hat{\mathbf{n}} \cdot \mu_r^{\text{in}} \mathbf{H}^{\text{in}},\end{aligned}\quad (30)$$

where $\hat{\mathbf{n}}$ is a unit vector normal to the surface and μ_r^{in} and μ_r^{out} are the relative magnetic permeabilities of the target and the surrounding medium respectively. Dividing the scatterer's surface into subsurfaces (patches) allows us to rewrite the boundary conditions in the following convenient form:

$$[\bar{\bar{G}}][P] = [V], \quad (31)$$

where

$$[\bar{\bar{G}}] = \begin{bmatrix} G_n^{P_n} & \mu_r G_n^{P_u} & \mu_r G_n^{P_v} \\ G_u^{P_n} & G_u^{P_u} & G_u^{P_v} \\ G_v^{P_n} & G_v^{P_u} & G_v^{P_v} \end{bmatrix}, \quad [P] = \begin{bmatrix} P_n \\ P_u \\ P_v \end{bmatrix}, \quad \text{and} \quad [V] = - \begin{bmatrix} H_n^{\text{pr}} \\ H_u^{\text{pr}} \\ H_v^{\text{pr}} \end{bmatrix}. \quad (32)$$

The vector $[P]$ contains the amplitudes of induced magnetic dipoles oriented along the $\hat{\mathbf{n}}$, $\hat{\mathbf{u}}$ and $\hat{\mathbf{v}}$ directions, where $\hat{\mathbf{n}}$ is normal to the surface and $\hat{\mathbf{v}} = \hat{\mathbf{n}} \times \hat{\mathbf{u}}$ and $\hat{\mathbf{u}} = \hat{\mathbf{v}} \times \hat{\mathbf{n}}$ are tangential to it. The impedance matrix $[\bar{\bar{G}}]$ depends only on the target's geometry and electromagnetic parameters and not on its location and orientation; its elements represent the exterior and interior solutions, expressed in terms of dipole sources distributed over the surface using a Green function of the form $e^{jkR}/4\pi R$. More explicit forms of the $G_{\xi}^{P_{\xi}}$ matrices, where $\hat{\xi} = \hat{\mathbf{n}}, \hat{\mathbf{u}}, \hat{\mathbf{v}}$, are presented in [4]. Finally, $[V]$ is the primary magnetic field that can be considered as a driving/forcing vector for the $[P]$. Since most actual UXO are heterogeneous objects, numerical methods may require tens or even hundreds of thousands of unknowns for magneto quasi static boundary-value problems. This makes rigorous 3D-EMI numerical models impractical for UXO discrimination. To achieve the goal of reproducing EMI responses of realistic objects quickly, accurately, and with only a few model parameters we developed the normalized surface magnetic source model.

2.4.2 Theoretical basis of NSMS

The NSMS model is based upon the assumption that the entire scatterer can be replaced with an auxiliary very thin surface shell. The primary magnetic field strikes the shell and induces on it a surface magnetization, in terms of which the secondary scalar potential can be written as [5]

$$\psi^{\text{sc}}(\mathbf{r}) = \frac{1}{4\pi} \oint_S \mathbf{M}(\mathbf{r}') \cdot \nabla' \frac{1}{R} ds' \quad (33)$$

Here $\mathbf{R} = \mathbf{r} - \mathbf{r}'$, where \mathbf{r} is the observation point and \mathbf{r}' is on the surface S , and $\mathbf{M}(\mathbf{r}')$ is a surface density of magnetization, which can be defined as the induced magnetic moment per unit surface: $\mathbf{m} = \oint_S \mathbf{M}(\mathbf{r}') ds'$. The surface density \mathbf{M} of magnetic polarization may be resolved at every point on S into normal and tangential components by means of the identity

$$\mathbf{M} = (\hat{\mathbf{n}} \cdot \mathbf{M})\hat{\mathbf{n}} + (\hat{\mathbf{n}} \times \mathbf{M}) \times \hat{\mathbf{n}}, \quad (34)$$

and combining (34), (33) and (27) we get for the total scattered magnetic field

$$\begin{aligned} \mathbf{H}^{\text{sc}}(\mathbf{r}) = & -\frac{1}{4\pi} \nabla \oint_S (\hat{\mathbf{n}}' \cdot \mathbf{M}(\mathbf{r}')) \hat{\mathbf{n}}' \cdot \nabla' \frac{1}{R} ds' \\ & - \frac{1}{4\pi} \nabla \oint_S (\hat{\mathbf{n}}' \times \mathbf{M}(\mathbf{r}')) \times \hat{\mathbf{n}}' \cdot \nabla' \frac{1}{R} ds'. \end{aligned} \quad (35)$$

The first integral in (35) may be interpreted as a scalar potential due to a double layer of moment

$$\boldsymbol{\tau}(\mathbf{r}') = (\hat{\mathbf{n}}' \cdot \mathbf{M}(\mathbf{r}')) \hat{\mathbf{n}}' = \sigma_m(\mathbf{r}') \hat{\mathbf{n}}', \quad (36)$$

and the second may be interpreted as a scalar potential due to a “free” magnetic charge distribution proportional to a discontinuity in the normal components of magnetic flux. Since the normal component of the magnetic field is always continuous across a boundary between two media, the total scattered magnetic field can thus be written as

$$\mathbf{H}^{\text{sc}}(\mathbf{r}) = -\nabla \oint_S \sigma_m(\mathbf{r}') g(\mathbf{r}, \mathbf{r}') ds' \quad (37)$$

where

$$g(\mathbf{r}, \mathbf{r}') = \frac{1}{4\pi} \hat{\mathbf{n}}' \cdot \nabla' \frac{1}{|\mathbf{r} - \mathbf{r}'|}. \quad (38)$$

Thus the EMI response of a permeable and conducting metallic object can be represented using a surface density $\sigma_m(s')$. At every point, the magnetic flux density \mathbf{B} is

$$\mathbf{B} = \mu_0 (\mathbf{H} + \mathbf{M}). \quad (39)$$

Using Gauss’s law for the magnetic flux density in the volume enclosed by S and using the divergence theorem we obtain

$$\begin{aligned}\int_V \nabla \cdot \mathbf{B} dv &= \mu_0 \oint_S (\mathbf{H} \cdot \hat{\mathbf{n}}' + \mathbf{M} \cdot \hat{\mathbf{n}}') ds' \\ &= \mu_0 \oint_S (H_n(\mathbf{r}') + \sigma_m(\mathbf{r}')) ds' = 0,\end{aligned}\quad (40)$$

and it follows that the magnetization density at a given point on the surface equals

$$\begin{aligned}\sigma_m(s') &= -H_n(s') = -(H_n^{\text{pr}}(s') + H_n^{\text{sc}}(s')) \\ &= -H_n^{\text{pr}}(s') (1 + P(s')), \end{aligned}\quad (41)$$

where $P(s')$ is in general position-dependent on S surface. In other words, the surface magnetic charge is proportional to the normal component $H_n^{\text{pr}}(s')$ of the primary magnetic field. This motivates us to introduce a normalized surface distribution $\Omega(s')$ through

$$\sigma_m(s') \equiv -\Omega(s') [\mathbf{H}^{\text{pr}}(s') \cdot \hat{\mathbf{n}}'], \quad (42)$$

which would result from exciting each patch of the surface S with a nonphysical unit primary magnetic field in the normal direction. After combining (37) and (42), the total scattered magnetic field can be expressed as

$$\begin{aligned}\mathbf{H}^{\text{sc}}(\mathbf{r}) &= \oint_S \Omega(\mathbf{r}') [\mathbf{H}^{\text{pr}}(\mathbf{r}') \cdot \hat{\mathbf{n}}'] \nabla g(\mathbf{r}, \mathbf{r}') ds' \\ &= \oint_S \Omega(\mathbf{r}') [\mathbf{H}^{\text{pr}}(\mathbf{r}') \cdot \hat{\mathbf{n}}'] \frac{3\mathbf{R}(\mathbf{R} \cdot \hat{\mathbf{n}}') - R^2 \hat{\mathbf{n}}'}{4\pi R^5} ds'.\end{aligned}\quad (43)$$

In the following we will argue that Ω , and in particular its integral over the surface,

$$Q = \oint_S \Omega ds', \quad (44)$$

contains all the information about an object that could be of need in the UXO discrimination problem, incorporating the effects of heterogeneity, interaction with other objects, and near- and far-field effects. We note that Q has dimensions of volume, which makes it comparable to the polarizability tensor elements of the point dipole model [12, 16-22].

2.4.3 Formulation for bodies of revolution; determining NSMS amplitudes from data

Most UXO are bodies of revolution (BOR), and the simplicity and efficiency afforded by this simplification motivates specializing the above analysis to scatterers with BOR symmetry. The best choice for auxiliary surface is a prolate spheroid, since it has BOR symmetry but at the same time has the elongated shape of UXO and can be made to have a definite orientation. We take a spheroid of semiminor and semimajor axes a and $b \equiv ea$ with $e > 1$. In the prolate spheroidal coordinate system (ξ, η, φ) we can write (43) in the form (see Figure 9)

$$\mathbf{H}^{\text{sc}}(\mathbf{r}) = \int_{-1}^1 h_{\eta'} d\eta' \int_0^{2\pi} h_{\varphi'} d\varphi' \Omega(\eta', \xi_0, \varphi') [\mathbf{H}^{\text{pr}}(\mathbf{r}') \cdot \hat{\xi}'] \nabla g(\mathbf{r}, \mathbf{r}'), \quad (45)$$

where the prolate spheroidal coordinates obey $-1 \leq \eta \leq 1$, $0 \leq \xi < \infty$, $0 \leq \varphi \leq 2\pi$, \mathbf{r} is the observation point, h_{η} and h_{φ} are the metric coefficients

$$h_{\eta} = \frac{d}{2} \sqrt{\frac{\xi_0^2 - \eta^2}{1 - \eta^2}} \quad \text{and} \quad h_{\varphi} = \frac{d}{2} \sqrt{(1 - \eta^2)(\xi_0^2 - 1)}, \quad (46)$$

the spheroid is characterized by $\xi_0 = e / \sqrt{e^2 - 1}$, and $d = 2\sqrt{b^2 - a^2}$ is the focal distance.

For a body with BOR symmetry the NSMS amplitude is azimuthally constant, and moreover the variation of the induced magnetic charge density σ is accounted for by the normal component of the primary magnetic field. This implies that $\Omega(\eta', \xi_0, \varphi') = \Omega(\eta')$. For convenience we define

$$\mathbf{H}^{\text{sc}}(\mathbf{r}) = \int_{-1}^1 \Omega(\eta') \mathbf{K}(\eta', \mathbf{r}) d\eta', \quad (47)$$

where

$$\mathbf{K}(\eta', \mathbf{r}) = \int_0^{2\pi} [\mathbf{H}^{\text{pr}}(\mathbf{r}') \cdot \hat{\xi}'] \nabla g(\mathbf{r}, \xi_0, \eta', \varphi') h_{\eta'} h_{\varphi'} d\varphi', \quad (48)$$

and assume that the NSMS can be approximated by a series of expansion functions $F_m(\eta')$ such that

$$\Omega(\eta') = \sum_{m=1}^M \Omega_m F_m(\eta') \quad (49)$$

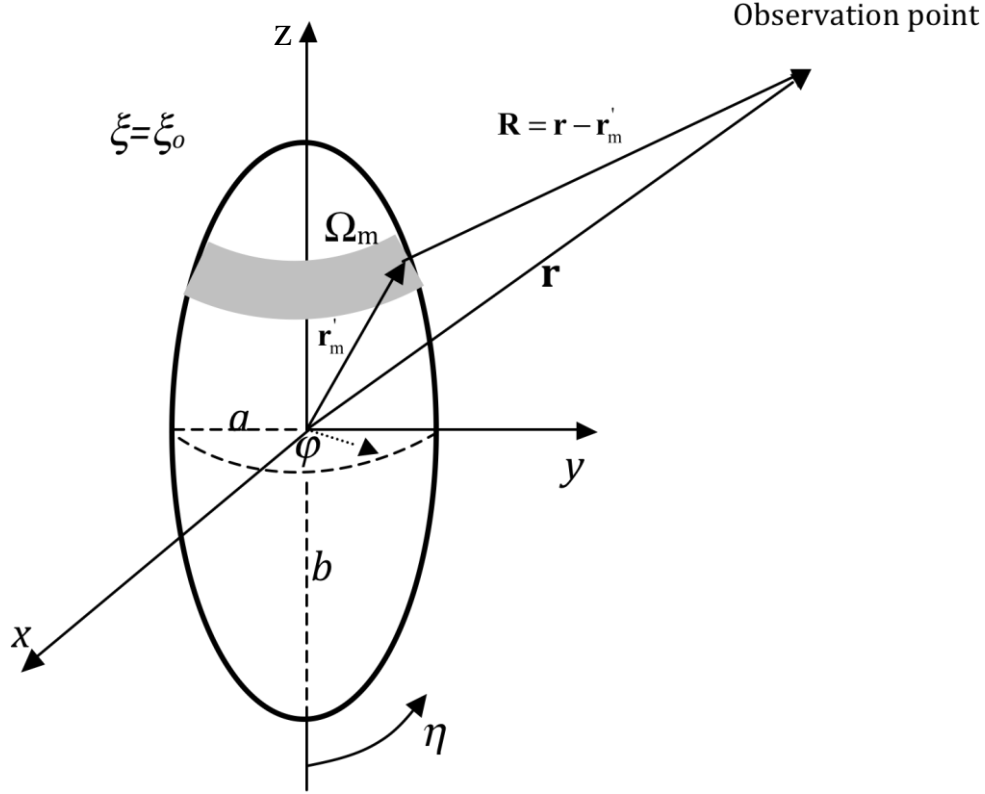


Figure 9: The NSMC that are distributed on a prolate spheroidal surface is implemented for a body of revolution. The prolate spheroidal coordinate system is specified by (ξ, η, ϕ) .

For computational simplicity, in the subsequent analysis we assume the expansion functions $F_m(\eta)$ are a set of orthogonal pulse functions given by

$$F_m(\eta') = \begin{cases} 1, & \eta' \in \Delta\eta_m \\ 0, & \text{otherwise.} \end{cases} \quad (50)$$

The expansion in terms of pulse functions is a “stairstep” approximation to the NSMS distribution on the spheroid along η' , where the spheroidal surface is divided into M belts. The expansion coefficient Ω_m thus corresponds to the NSMS amplitude at the m -th belt. Substituting into (47) we obtain

$$\mathbf{H}^{\text{sc}}(\mathbf{r}) = \int_{-1}^1 \sum_{m=1}^M \Omega_m F_m(\eta') \mathbf{K}(\eta', \mathbf{r}) d\eta', \quad (51)$$

and the use of (50) in (51) enables us to write

$$\begin{aligned} \mathbf{H}^{\text{sc}}(\mathbf{r}) &= \sum_{m=1}^M \Omega_m \int_{\Delta\eta_m} \mathbf{K}(\eta, \mathbf{r}) d\eta \equiv \sum_{m=1}^M \Omega_m \mathbf{f}(\eta_m, \mathbf{r}) \\ &= \Omega_1 \mathbf{f}(\eta_1, \mathbf{r}) + \Omega_2 \mathbf{f}(\eta_2, \mathbf{r}) + \cdots + \Omega_M \mathbf{f}(\eta_M, \mathbf{r}). \end{aligned} \quad (52)$$

The physical interpretation of this equation is as follows. The spheroid has been divided up to M belts, each of surface $\Delta S_m = 2\pi h_{\eta'}^m h_{\phi'}^m \Delta \eta_m$, as shown in Figure 9, with the NSMS being an unknown constant over each belt. At the center of each segment, the sum of the scattered fields from all M belts is set to equal the measured field $\mathbf{H}^{\text{data}}(\mathbf{r})$ at point \mathbf{r} that is a known field arising from the scatterer. For a point \mathbf{r}_n the latter equation leads to

$$\sum_{m=1}^M \Omega_m \mathbf{f}(\eta_m, \mathbf{r}_n) = \mathbf{H}^{\text{data}}(\mathbf{r}_n) \quad (53)$$

So far we have only generated one equation (or three if we have access to the full vector field) with M unknowns. We can obtain additional independent equations by using data collected at different points \mathbf{r}_n with $n = 1, 2, \dots, N$. Matching the modeled scattered magnetic field to the data at these N points results in the linear system

$$[\mathbf{Z}_{mn}][\Omega_m] = [\mathbf{H}^{\text{data}}(\mathbf{r}_n)], \quad (54)$$

with

$$\begin{aligned} [\mathbf{Z}_{mn}] &= \begin{bmatrix} \mathbf{f}(\eta_1, \mathbf{r}_1) & \mathbf{f}(\eta_2, \mathbf{r}_1) & \cdots & \mathbf{f}(\eta_M, \mathbf{r}_1) \\ \mathbf{f}(\eta_1, \mathbf{r}_2) & \mathbf{f}(\eta_2, \mathbf{r}_2) & \cdots & \mathbf{f}(\eta_M, \mathbf{r}_2) \\ \vdots & \vdots & \ddots & \vdots \\ \mathbf{f}(\eta_1, \mathbf{r}_N) & \mathbf{f}(\eta_2, \mathbf{r}_N) & \cdots & \mathbf{f}(\eta_M, \mathbf{r}_N) \end{bmatrix}, \\ [\Omega_m] &= [\Omega_1 \ \Omega_2 \ \dots \ \Omega_M]^T, \\ [\mathbf{H}^{\text{data}}(\mathbf{r}_n)] &= [\mathbf{H}^{\text{data}}(\mathbf{r}_1) \ \mathbf{H}^{\text{data}}(\mathbf{r}_2) \ \dots \ \mathbf{H}^{\text{data}}(\mathbf{r}_N)]^T, \end{aligned} \quad (55)$$

and $\mathbf{f}(\eta_m, \mathbf{r}_n)$ given by (52), whose solution can be written symbolically as

$$[\Omega_m] = \frac{[\mathbf{Z}_m]^T [\mathbf{H}^{\text{data}}(\mathbf{r}_n)]}{[\mathbf{Z}_m]^T [\mathbf{Z}_m]}. \quad (56)$$

Once $[\Omega_m]$ is determined the object's EMI response can be computed readily. The resulting discrete NSMS distribution can then be used to compute the total NSMS amplitude, which is a global measure of Ω for the entire object and can be used for discrimination:

$$Q = \sum_{m=1}^M \Omega_m \Delta S_m. \quad (57)$$

In the following sections we study some features of this global measure of response.

2.4.4 The dipole model as a limiting case of NSMS

Here we show that NSMS reduces in the limit to the point dipole model [16-21] of Section 2.3. Recall that the magnetic field due to a dipole of moment \mathbf{m} is

$$\mathbf{H}^{\text{sc}}(\mathbf{r}) = \frac{1}{4\pi R^3} \mathbf{m} \cdot (3\hat{\mathbf{R}}\hat{\mathbf{R}} - \bar{\mathbf{I}}), \quad (58)$$

where $\hat{\mathbf{R}}$ is the unit vector along $\mathbf{R} = \mathbf{r} - \mathbf{r}_d$ and \mathbf{r}_d and \mathbf{r} are respectively the location of the dipole and the observation point, as seen in Figure 10, while $\bar{\mathbf{I}}$ is the identity dyad. The relation between the induced dipole moment \mathbf{m} and the primary magnetic field \mathbf{H}^{pr} at the dipole location is given by

$$\mathbf{m} = \bar{\bar{\mathbf{M}}} \cdot \mathbf{H}^{\text{pr}}(\mathbf{r}_d), \quad (59)$$

where the magnetic polarizability tensor $\bar{\bar{\mathbf{M}}}$ depends on the scatterer's shape, size, and material properties. For a body of revolution, the polarizability tensor in a coordinate system aligned with the scatterer's principal axes can be written as

$$\bar{\bar{\mathbf{M}}} = \begin{bmatrix} \beta_{\rho\rho} & 0 & 0 \\ 0 & \beta_{\rho\rho} & 0 \\ 0 & 0 & \beta_{zz} \end{bmatrix} \quad (60)$$

where the degeneracy in the “radial” element $\beta_{\rho\rho}$ displays the BOR symmetry explicitly. The target's principal axes and the global coordinate system are related by the Euler rotation tensor.

Now let us prove that in the dipole model is a limited case of the NSMS. To do that, first let us divide the surrounding spheroidal surface into three belts and assume that on the m -th belt the NSMS density follows a Dirac delta distribution (see Figure 10). With these assumptions the scattered magnetic field (58) becomes

$$\mathbf{H}^{\text{sc}}(\mathbf{r}) = \frac{1}{4\pi} \sum_{m=1}^3 \frac{1}{R_m^3} \Omega_m H_m^{\text{pr}}(\mathbf{r}_m) \hat{\mathbf{n}}_m \cdot (3\hat{\mathbf{R}}_m \hat{\mathbf{R}}_m - \bar{\mathbf{I}}) \quad (61)$$

where now $\mathbf{R} = \mathbf{r} - \mathbf{r}_m$ points from \mathbf{r}_m on the m -th belt to the observation point. As $S \rightarrow 0$ we have that $\mathbf{r}_m \rightarrow \mathbf{r}_d$, and $H_n^{\text{pr}}(\mathbf{r}_m) = H_n^{\text{pr}}(\mathbf{r}_d)$, and because $\hat{\mathbf{n}}_2 = \hat{\boldsymbol{\rho}} = \alpha_1 \hat{\mathbf{x}} + \alpha_2 \hat{\mathbf{y}}$, and $\hat{\mathbf{n}}_1 = -\hat{\mathbf{n}}_3 = \hat{\mathbf{z}}$, ($\alpha_1 = \cos \alpha$ and $\alpha_2 = \sin \alpha$, where α is the angle between $\hat{\boldsymbol{\rho}}$ and $\hat{\mathbf{x}}$) then (61) reduces to

$$\mathbf{H}^{\text{sc}}(\mathbf{r}) = \frac{3\hat{\mathbf{R}}\hat{\mathbf{R}} - \bar{\mathbf{I}}}{4\pi R^3} \cdot (2\Omega_1 H_z^{\text{pr}}(\mathbf{r}_d) \hat{\mathbf{z}} + \Omega_2 (H_x^{\text{pr}}(\mathbf{r}_d) \alpha_1 \hat{\mathbf{x}} + H_x^{\text{pr}}(\mathbf{r}_d) \alpha_2 \hat{\mathbf{y}})) \quad (62)$$

in terms of the Cartesian unit vectors $\hat{\mathbf{x}}$, $\hat{\mathbf{y}}$, and $\hat{\mathbf{z}}$. After introducing a diagonal tensor

$$\bar{\bar{\mathbf{M}}}_n = \begin{bmatrix} \Omega_2 & 0 & 0 \\ 0 & \Omega_2 & 0 \\ 0 & 0 & 2\Omega_1 \end{bmatrix} \quad (63)$$

and the vector $\mathbf{m}_n = \bar{\bar{\mathbf{M}}}_n \cdot \mathbf{H}^{\text{pr}}(\mathbf{r}_d)$, (62) can be written as

$$\begin{aligned} \mathbf{H}^{\text{sc}}(\mathbf{r}) &= \frac{1}{4\pi R^3} \mathbf{m}_n \cdot (3\hat{\mathbf{R}}\hat{\mathbf{R}} - \bar{\bar{\mathbf{I}}}) \\ &= \frac{1}{4\pi R^3} [\bar{\bar{\mathbf{M}}}_n \cdot \mathbf{H}^{\text{pr}}(\mathbf{r}_d)] \cdot (3\hat{\mathbf{R}}\hat{\mathbf{R}} - \bar{\bar{\mathbf{I}}}), \end{aligned} \quad (64)$$

which proves that in the limit the NSMS model is identical to the infinitesimal dipole approximation.

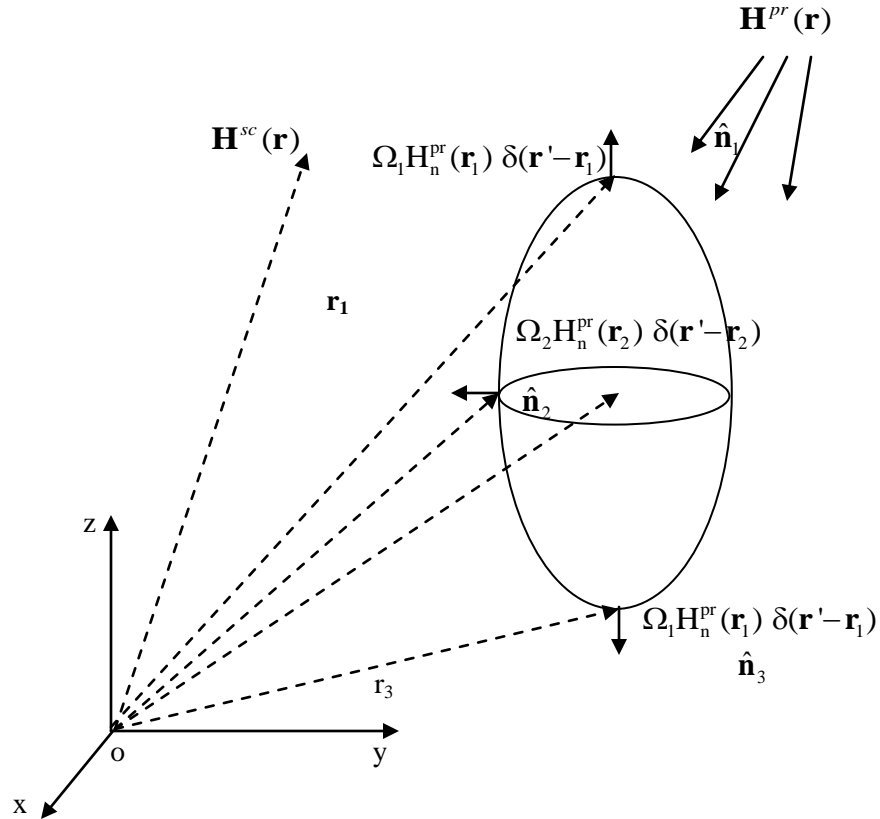


Figure 10: A schematic diagram for a dipole model.

2.4.5 Invariance properties of the total NSMS

One of the distinguishing features of the NSMS model is that the total NSMS amplitude is a global characteristic of the object and is independent of the size of the surrounding spheroidal surface. To illustrate this feature let us consider a sphere of radius a , conductivity σ , and permeability $\mu = \mu_r \mu_0$ illuminated with a time-varying uniform magnetic field $\mathbf{H}^{\text{pr}} = \hat{\mathbf{z}}$. The scattered magnetic field at any point outside the sphere can be written in analytic form as

$$\mathbf{H}_{\text{sph}} = \frac{1}{4\pi R^3} \mathbf{m}_{\text{sph}} \cdot (3\hat{\mathbf{R}}\hat{\mathbf{R}} - \bar{\bar{\mathbf{I}}}), \quad (65)$$

where $\mathbf{m}_{\text{sph}} = \beta \mathbf{H}^{\text{pr}}$ is the magnetic dipole moment of the sphere, and the polarizability β can be expressed in terms of the induction number $k = \sqrt{j\omega\mu_r\mu_0\sigma}$ through

$$\beta = 2\pi a^3 \frac{(2\mu_r + 1)(ka \coth ka - 1) - (ka)^2}{(\mu_r - 1)(ka \coth ka - 1) + (ka)^2}. \quad (66)$$

The scattered field due to the NSMS density in the spherical coordinate system is

$$\mathbf{H}^{\text{sc}}(\mathbf{r}) = \nabla \int_0^{2\pi} a^2 d\varphi \int_0^\pi \Omega(\theta) \cos \theta \frac{\hat{\mathbf{n}}' \cdot \mathbf{R}}{R^3} \sin \theta d\theta, \quad (67)$$

where

$$\begin{aligned} \hat{\mathbf{n}}' &= \hat{\mathbf{r}}' = \sin \theta \cos \varphi \hat{\mathbf{x}} + \sin \theta \sin \varphi \hat{\mathbf{y}} + \cos \theta \hat{\mathbf{z}}, \\ \hat{\mathbf{n}}' \cdot \mathbf{R} &= \hat{\mathbf{n}}' \cdot (\mathbf{r} - \hat{\mathbf{r}}) = z_0 \cos \theta - a, \\ R &= \sqrt{a^2 + z_0^2 - 2az_0 \cos \theta}. \end{aligned} \quad (68)$$

For a homogeneous sphere the amplitude of NSMS density $\Omega = \Omega_0$ is constant over the spherical surface and is the only unknown to be determined. This can be achieved by matching the secondary magnetic field of the NSMS with the dipole field (58) at an observation point; for convenience we take $\mathbf{r} = z_0 \hat{\mathbf{z}}$.

The closed-form solution for the sphere becomes

$$H_z^{\text{sph}} = \frac{m_z}{4\pi} \left[\frac{3z_0^2}{z_0^5} - \frac{1}{z_0^3} \right] = \frac{2m_z}{4\pi z_0^3} \quad (69)$$

and the scattered NSMS magnetic field due to a uniform source density Ω_0 simplifies to

$$\begin{aligned}
H_z^{\text{sc}} &= 2\pi a^2 \Omega_0 \frac{\partial}{\partial z_0} \int_0^\pi \sin \theta d\theta \frac{\cos \theta (z_0 \cos \theta - a)}{(a^2 + z_0^2 - 2az_0 \cos \theta)^{3/2}} \\
&= 2\pi a^2 \Omega_0 \frac{\partial}{\partial z_0} \left(\frac{2}{3z_0^2} \right) = -\frac{8\pi a^2 \Omega_0}{3z_0^3} = -\frac{2Q}{3z_0^3}
\end{aligned} \tag{70}$$

where $Q = 4\pi a^2 \Omega_0$ is the total NSMS of the sphere. Comparing (69) and (70) we find that

$$Q = -\frac{3}{8\pi} m_z. \tag{71}$$

The total NSMS is thus independent of the size of the surrounding surface and is an intrinsic property of the scatterer.

2.4.6 Interpretation of the total NSMS

The total NSMS (and its time evolution) depends on the size, geometry, and material composition of the object in question. Early time gates bring out the high-frequency response to the shutdown of the exciting field; the induced eddy currents in this range are superficial, and a large NSMS amplitude at early times correlates with large objects whose surface stretches wide. At late times, where the eddy currents have diffused completely into the object and low-frequency harmonics dominate, the EMI response relates to the metal content (*i.e.*, the volume) of the target. Thus a smaller but compact object has a relatively weak early response that dies down slowly, while a large but thin or hollow object has a strong initial response that decays quickly. These features can be neatly summarized by the parameters of an empirical decay-law model like the Pasion-Oldenburg law see (75).

2.4.7 The parameterized NSMS

During APG standardized test-site discrimination studies (see Chapter 4) we use a parameterized version of NSMS to encapsulate the electromagnetic signature of a target [23]. In this version of the model—which provides at least three independent polarizability-like parameters for use in discrimination and thus in a sense extracts further information from the same data—the scatterer is associated with a surrounding sphere S on which a set of dipoles are distributed. The secondary field is expressed as

$$\mathbf{H}^{\text{sc}}(\mathbf{r}, t) = \oint_S \frac{3\hat{\mathbf{R}}_{s'}\hat{\mathbf{R}}_{s'} - \mathbf{1}}{4\pi R_{s'}^3} \cdot \left\{ \begin{bmatrix} \Omega_{xx}(\mathbf{r}_{s'}, t) & \Omega_{xy}(\mathbf{r}_{s'}, t) & \Omega_{xz}(\mathbf{r}_{s'}, t) \\ \Omega_{yx}(\mathbf{r}_{s'}, t) & \Omega_{yy}(\mathbf{r}_{s'}, t) & \Omega_{yz}(\mathbf{r}_{s'}, t) \\ \Omega_{zx}(\mathbf{r}_{s'}, t) & \Omega_{zy}(\mathbf{r}_{s'}, t) & \Omega_{zz}(\mathbf{r}_{s'}, t) \end{bmatrix} \begin{bmatrix} H_x^{\text{pr}}(\mathbf{r}_{s'}) \\ H_y^{\text{pr}}(\mathbf{r}_{s'}) \\ H_z^{\text{pr}}(\mathbf{r}_{s'}) \end{bmatrix} \right\} ds' \equiv \vec{\mathbf{Z}} \cdot \mathbf{\Omega}, \tag{72}$$

where $\mathbf{R}_{s'}$ points from the location $\mathbf{r}_{s'}$ of the s' -th patch on the sphere to the observation point \mathbf{r} and the response amplitude of each patch is a combination of the primary field piercing it and the tensor of normalized strengths $\Omega_{ij}(\mathbf{r}_{s'}, t)$, which, as usual [24], is symmetric: $\Omega_{ij} = \Omega_{ji}$. The z -axis is dictated by the direction of \mathbf{m} from HAP or from the dipole model, and the x - and y -axes are arbitrarily chosen to be perpendicular to $\hat{\mathbf{z}}$ and to each other. The integral is again transformed to a matrix-vector product through numerical quadrature. The amplitude array $\mathbf{\Omega}$ is determined by minimizing in a least-squares sense the difference between measured data with a known object-sensor configuration and the predictions of equation (72). Once the tensor elements $\Omega_{ij}(s')$ are found one can define “total polarizabilities” by integrating over the sphere,

$$Q_{ij}(t) = \oint_S \Omega_{ij}(\mathbf{r}_{s'}, t) ds', \quad (73)$$

and these can in turn be used to find “principal elements” through joint diagonalization:

$$\begin{bmatrix} Q_{xx}(t) & Q_{xy}(t) & Q_{xz}(t) \\ Q_{yx}(t) & Q_{yy}(t) & Q_{yz}(t) \\ Q_{zx}(t) & Q_{zy}(t) & Q_{zz}(t) \end{bmatrix} = \mathbf{\Lambda} \begin{bmatrix} Q_x(t) & 0 & 0 \\ 0 & Q_y(t) & 0 \\ 0 & 0 & Q_z(t) \end{bmatrix} \mathbf{\Lambda}', \quad (74)$$

where the matrix $\mathbf{\Lambda}$ is orthogonal and the prime denotes transposition. The information contained in the diagonal tensor can be summarized further by incorporating the empirical decay law of Pasion and Oldenburg [25]:

$$M_{\alpha\alpha}(t) \equiv Q_{\alpha}(t) = B_{\alpha\alpha} t^{-\beta_{\alpha\alpha}} e^{-\gamma_{\alpha\alpha} t}, \quad \alpha = x, y, z, \quad (75)$$

where t is the time, $B_{\alpha\alpha}$, $\beta_{\alpha\alpha}$, and $\gamma_{\alpha\alpha}$ are the fitting parameters, and $M_{\alpha\alpha}(t)$ is the total NSMS along the x , y , and z directions in the body frame. The principal NSMS elements and the Pasion-Oldenburg parameters are intrinsic to the object and can be used, on their own or in combination with other quantities, in discrimination processing.

2.5 The orthonormalized volume magnetic source model

Most EMI sensors are composed of separate transmitting and receiving coils. When the operator activates the sensor, a current runs through the transmitter coils, which results in the establishment of a (“primary” or “principal”) magnetic field in the surrounding space (Figure 11). According to the elementary atomic model of matter, all materials are composed of atoms, each with a positively charged nucleus and a number of orbiting negatively charged electrons. The orbiting electrons cause circulating

currents and form microscopic magnetic dipoles. In the absence of an external magnetic field the magnetic dipoles of atoms of most materials have random orientations, resulting in no magnetic moment. The application of an external time varying magnetic field, by Faraday's law, induces eddy currents in highly conducting bodies by an alignment of the magnetic moments of the spinning electrons and a magnetic moment due to a change in the orbital motion of electrons. These currents and magnetization in turn generate a ("secondary" or "scattered") magnetic field that also varies with time and induces measurable currents in the receiving coils. The induced magnetic dipoles/eddy currents are distributed inside the object and produce a magnetic field intensity \mathbf{H} outside. The magnetic field due to the i -th source can then be expressed at any observation point \mathbf{r} as the matrix-vector product

$$\mathbf{H}_i(\mathbf{r}) = G_i(\mathbf{r})\mathbf{m}_i, \quad (76)$$

where the Green function G_i is given in detail in equation (19). When there are several such sources, the total field can be expressed as a superposition:

$$\mathbf{H}(\mathbf{r}) = \sum_{i=1}^M G_i(\mathbf{r})\mathbf{m}_i = \begin{bmatrix} G_1 & G_2 & \cdots \end{bmatrix} \begin{bmatrix} \mathbf{m}_1 \\ \mathbf{m}_2 \\ \vdots \end{bmatrix}. \quad (77)$$

Before going further we note that our method takes as input the (in principle unknown) number M of radiating sources. For advanced EMI sensors such as the MetalMapper and 2×2 and 5×5 TEMTADS arrays we have developed a procedure based on joint diagonalization, sketched in Section 2.6, that estimates M starting from raw data and with no need for inversion. For other sensors one may proceed by letting M vary as part of an optimization routine.

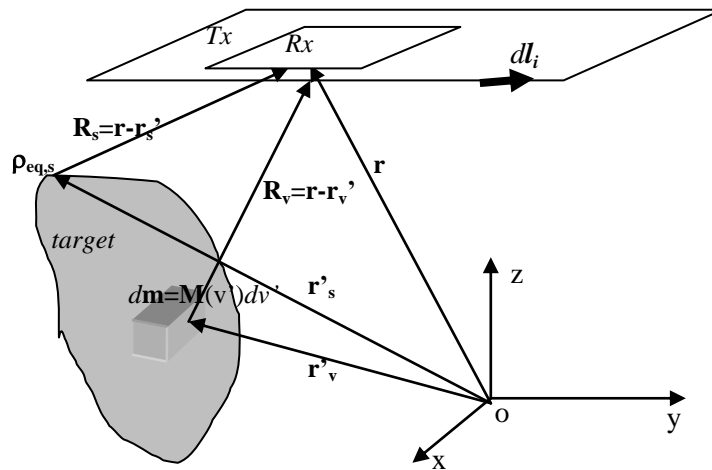


Figure 11: A metallic object under the transmitter. The target's EMI response at the receiver coil can be calculated from the equivalent surface or volume magnetic dipole moment $d\mathbf{m}$.

The superposition (77) can be used (and often has) to carry out one- and multi-object inversions starting from data taken at an ensemble of points. All the measured \mathbf{H} -values—which can pertain to multiple transmitters, multiple receivers, and different vector components—are strung together in a one-dimensional array, while the corresponding Green functions are stacked as matrix rows. The resulting composite G matrix can then be (pseudo)inverted to find the strengths of the sources. This procedure, which is nothing other than the dipole model if each body is taken to be represented by one source only, works well for one or two sources, but for larger numbers becomes very time-consuming (since the Green matrix becomes very large) and increasingly ill-posed, usually requiring regularization. The ONVMS method is designed to circumvent these difficulties.

2.5.1 Orthonormal Green functions

The method starts from the realization that the matrix-vector product (76) is valid at any observation point \mathbf{r} and, in particular, at every point \mathbf{r}_s . If we introduce the inner product

$$\langle A, B \rangle = \int_S A^T B ds = \int_{\text{Rx}_0} A^T B ds + \int_{\text{Rx}_1} A^T B ds + \dots, \quad (78)$$

where the integral is computed over the “sensitive” surfaces of the sensor, and if furthermore we can find a basis of Green functions orthogonal under this measure,

$$\mathbf{H}(\mathbf{r}_s) = \sum_{j=1}^M \Psi_j(\mathbf{r}_s) \mathbf{b}_j \quad \text{such that} \quad \langle \Psi_j, \Psi_k \rangle = F_j \delta_{jk}, \quad (79)$$

where δ_{jk} is a Kronecker delta, then it is possible to find the source amplitudes \mathbf{b}_j without costly and ill-conditioned inversions simply by exploiting the sifting property of the orthogonal basis:

$$\langle \Psi_k, \mathbf{H} \rangle = \sum_{j=1}^M \langle \Psi_k, \Psi_j \rangle \mathbf{b}_j = \sum_{j=1}^M F_k \delta_{kj} \mathbf{b}_j = F_k \mathbf{b}_k \quad (80)$$

and thus

$$\mathbf{b}_k = F_k^{-1} \langle \Psi_k, \mathbf{H} \rangle, \quad (81)$$

which clearly does not involve solving a linear system of equations; it is necessary to invert only the 6×6 matrix F_k . Moreover, this definition of the coefficients \mathbf{b}_j guarantees that they are “optimal” in the sense that the expansion (79) yields the least mean-square error $\langle \mathbf{H} - \sum_{j=1}^M \Psi_j \mathbf{b}_j, \mathbf{H} - \sum_{j=1}^M \Psi_j \mathbf{b}_j \rangle$ [26].

To construct the set of orthonormal Green functions we resort to a generalization of the Gram-Schmidt procedure [27]. Assuming that the Green matrices are linearly independent—i.e., that we cannot have a collection of distinctly located dipole sources combining to produce no measurable field unless their amplitudes all vanish—we define

$$\begin{aligned}\Psi_1 &= G_1, \\ \Psi_2 &= G_2 - \Psi_1 A_{21}, \\ &\vdots \\ \Psi_m &= G_m - \sum_{k=1}^{m-1} \Psi_k A_{mk}, \\ &\vdots \\ \Psi_M &= G_M - \sum_{k=1}^{M-1} \Psi_k A_{Mk},\end{aligned}\tag{82}$$

where the 6×6 matrices A_{jk} obey $A_{jk} = 0$ for $j \leq k$. Enforcing the orthogonality relation (79) is equivalent to setting $\langle \Psi_n, G_m \rangle = F_n A_{nm}$ for $n < m$, and using this relation twice in definition (82) we find

$$A_{mn} = F_n^{-1} \left(C_{nm} - \sum_{k=1}^{n-1} A_{nk}^T F_k A_{mk} \right),\tag{83}$$

where the overlap integral $C_{mn} = \langle G_m, G_n \rangle$.

At the end of the process it is necessary to recover an expansion expressed, like (76), in terms of the actual Green functions, in part because the functions Ψ_j are orthogonal (and defined) only at points on the receivers, and in part because of the non-uniqueness of the coefficients \mathbf{b}_j due to the arbitrary order in which the G_j enter the recursion (82). To that end, we express

$$\Psi_m = \sum_{k=1}^m G_k B_{mk},\tag{84}$$

and to find the coefficients B_{mk} we compare expansion (84) term by term to the definition (82) and use the rule that $A_{jk} = 0$ for $j \leq k$ to find

$$\begin{aligned}B_{mm} &= I, \text{ the identity,} \\ B_{m(m-1)} &= -A_{m(m-1)}, \\ B_{mq} &= -\sum_{l=q}^{m-1} B_{lq} A_{ml} \text{ for } 1 \leq q \leq m-2,\end{aligned}\tag{85}$$

in terms of which we recover the physical polarizability elements:

$$\mathbf{H} = \sum_{k=1}^M \Psi_k \mathbf{b}_k = \sum_{k=1}^M \left(\sum_{l=1}^k G_l B_{kl} \right) \mathbf{b}_k = \sum_{l=1}^M G_l \left(\sum_{k=l}^M B_{kl} \mathbf{b}_k \right) = \sum_{l=1}^M G_l \mathbf{m}_l. \quad (86)$$

2.5.2 ONVMS procedure

With all the pieces in place, we can sketch an algorithm to invert EMI data using the ONVMS model:

- 1) Given a number of sources and their tentative locations, find the Green tensors $G_i \equiv \bar{\bar{\gamma}}$ using equation (23) and compute the overlap integrals G_{mn} using the inner product (78).
- 2) Determine the first normalization factor, $F_1 = \langle G_1, G_1 \rangle$, and use it to find all the Gram-Schmidt coefficients A_{mn} with $n=1$: $A_{m1} = F_1^{-1} C_{1m}$.
- 3) Set $m=2$; compute, in sequence,
 - a) The coefficients A_{mn} with $n=2, \dots, m-1$ using equation (83);
 - b) The function Ψ_m using the expansion (82);
 - c) The normalization factor $F_m = \langle \Psi_m, \Psi_m \rangle$;

increase m by 1 and iterate until all sources have been included.

- 4) Once all the A_{mn} , F_m , and Ψ_m are known, find B_{mq} using (85).
- 5) Use the orthonormality of the new Green functions to determine the source amplitudes using $\mathbf{b}_q = F_q^{-1} \langle \Psi_q, \mathbf{H}^{\text{data}} \rangle$, as in (81). Take the measured field to be piecewise constant—i.e., constant throughout each receiver—when evaluating the integrals.
- 6) Use the computed \mathbf{b}_q , B_{mq} , and G_m , along with the expansion (86), to generate the secondary field prescribed by the given number of sources at the given locations.
- 7) Compare the model prediction with the measured data, vary the source locations, and iterate until the least-squares discrepancy between prediction and measurement attains a suitable minimum.

The procedure as written applies to only one time gate, but the extension to fully time-dependent functions is straightforward: we need only substitute the vectors \mathbf{b}_q and \mathbf{H}^{data} for two-dimensional arrays

where the columns denote time. The relations between the two, namely (81) and (86), acquire multiple right-hand-sides, and the optimization mentioned on Step 7 of the algorithm is constrained further. As a final remark we note that rigorously speaking the coefficients \mathbf{b}_q (and, for that matter, the amplitudes \mathbf{m}_k) are *not* the polarizabilities themselves but relate more closely to their time derivatives [28, 29].

The great advantage of the ONVMS technique is that it takes into account mutual couplings between different parts of targets and avoids matrix singularity problems in cases with multiple objects. Once the polarizability tensor elements and the locations of the elemental responding dipoles are determined one can group them according to their volume distribution. For each group a total polarizability tensor can be computed and diagonalized using joint diagonalization, the topic of Section 2.6. The resulting time-dependent diagonal elements have been shown to be intrinsic to the objects and can be used, on their own or combined with other quantities, in discrimination processing.

2.6 Joint diagonalization for multi-target data pre-processing

In real life situations the targets of interest are usually surrounded by natural and artificial debris with metallic content, including, for instance, the remains of ordnance that did explode. Thus it is usually not clear how many objects are producing a given detected signal; all sensing methods, including EMI, are fraught with detection rates that overwhelm cleanup efforts and hike their cost. Here we introduce a data pre-processing technique based on joint diagonalization (JD) that estimates the number of targets present in the field of view of the sensor as it takes a data shot, and, in a good number of cases, even provides the capability to perform real-time characterization and classification of the targets without the need for a forward model.

Joint diagonalization has become an important tool for signal processing and inverse problems, used as part of independent component analysis [30], blind source separation or BSS [31], common principal component analysis, and, more recently, kernel-based nonlinear BSS [32]. We further extend the applicability of the method by using it to detect and locate buried targets without the need for inversion. As we say above, a variation of the method can be used to extricate time-dependent electromagnetic signatures from attitude information. Here we will outline the detailed procedure as applied to the TEMTADS sensor array, a time-domain device with 25 transmitter/receiver pairs that provides 625 measurements over $N_g = 123$ time gates at each sensor location.

2.6.1 The multi-static response matrix

JD estimates the eigenvalues and eigenvectors of a square time- or frequency-dependent multi-static response (MSR) matrix synthesized directly from measured values. To construct the MSR matrices

one just has to stack the 625 readings at each time gate in a 25×25 array so that each column stands for one of N_t transmitters and each row represents one of N_r receivers:

$$\mathbf{S}(t_k) = \begin{bmatrix} H_{11} & H_{12} & \cdots & H_{1N_t} \\ H_{21} & H_{22} & \cdots & H_{2N_t} \\ \mathbf{M} & \mathbf{M} & \mathbf{O} & \mathbf{M} \\ H_{N_r,1} & H_{N_r,2} & \mathbf{L} & H_{N_r,N_t} \end{bmatrix}, \quad k = 1, K, N_g, \quad (87)$$

where the element H_{ij} is the field measured by the i -th receiver when the j -th transmitter is fired. The second step of the procedure is to diagonalize the 123 matrices at one stroke so they all share a single set of orthonormal eigenvectors. In other words, given the MSR matrix $\mathbf{S}(t_k)$ at the k -th time gate, we look for a unitary matrix \mathbf{V} such that the products

$$\mathbf{D}_k = \mathbf{V}^T \mathbf{S}(t_k) \mathbf{V} \quad (88)$$

are “as diagonal as possible” (i.e., their off-diagonal elements vanish within a preset tolerance). By diagonalizing all the matrices simultaneously we separate the time-dependent intrinsic features of the responding sources (and hence the interred objects), which get encapsulated in the eigenvalues, from the other factors—notably the location and orientation of the target with respect to the sensor—that influence the signal but do not change as the data are being taken; these get bundled into the eigenvectors. (The fact that the locations and orientations can be dissociated in this way from the electromagnetic signatures is an upside of the low frequencies of the quasistatic EMI range, because the relevant Green functions are time-independent.) Thus the measured data can be resolved as a superposition of “elemental” sub-signals, each corresponding to an elementary dipolar source, whose combination corresponds to the buried objects. Each source—and the corresponding field singularity—can moreover be localized numerically: the TEMTADS geometry is such that the diagonal of the unprocessed MSR matrix mimics a set of monostatic measurements, akin to those taken with a handheld sensor, which peak sharply when there is a target directly underneath. The maxima in the diagonal thus point to the transmitter/receiver pairs closest to any responding sources. These location estimates can be grouped and correlated to the eigenvalue distributions to estimate target locations.

2.6.2 Interpretation and diagonalization of the MSR matrix

We now proceed to express our above considerations quantitatively. Initially we consider the transmitter assembly, which in TEMTADS consists of a set of coplanar square loops forming a regular grid. The Biot-Savart law gives the primary magnetic induction established at the location \mathbf{r}_l of the l -th

source when the j -th transmitter antenna (whose area is σ_{Tx_j}) is excited immediately before shutoff by a current I_j :

$$\mathbf{B}_{jl}^{\text{pr}} = \frac{\mu_0 I_j}{4\pi} \sigma_{\text{Tx}_j} \frac{1}{\sigma_{\text{Tx}_j}} \oint \frac{d\mathbf{l}' \times (\mathbf{r}_l - \mathbf{r}')}{|\mathbf{r}_l - \mathbf{r}'|^3} = \mathbf{g}_{jl}^{\text{pr}} \sigma_{\text{Tx}_j} I_j. \quad (89)$$

This primary field induces in the l -th source a dipole moment given by

$$\mathbf{m}_{jl} = \mathbf{U}_l \mathbf{\Lambda}_l \mathbf{U}_l^T \mathbf{B}_{jl}^{\text{pr}}, \quad (90)$$

where the Euler rotation matrix \mathbf{U} relates the instrument's coordinate axes to the principal axes of the source, and the diagonal polarizability matrix $\mathbf{\Lambda}_i$, the only quantity intrinsic to the source, measures the strength with which the primary field induces a moment along each of those axes.

According to Faraday's law, the signal measured by a receiver coil is the electromotive force given by the negative of the time derivative of the secondary magnetic flux through the coil. Since the field at point \mathbf{r} of a dipole of moment \mathbf{m} placed at \mathbf{r}_0 is given by

$$\mathbf{B} = \frac{\mu_0}{4\pi} \nabla \times \left(\mathbf{m} \times \frac{\mathbf{r} - \mathbf{r}_0}{|\mathbf{r} - \mathbf{r}_0|^3} \right), \quad \text{and thus} \quad \int \mathbf{B} \cdot d\mathbf{s} = -\mathbf{m} \cdot \frac{\mu_0}{4\pi} \oint d\mathbf{l} \times \frac{\mathbf{r} - \mathbf{r}_0}{|\mathbf{r} - \mathbf{r}_0|^3} \quad (91)$$

by straightforward application of Stokes's theorem, one obtains that the signal sampled at time t_k by the i -th receiver (of area σ_{Rx_i}) when the l -th source is excited by the j -th transmitter is

$$\begin{aligned} H_{ij}^l(t_k) \sigma_{\text{Rx}_i} \sigma_{\text{Tx}_j} I_j &= \frac{\mu_0}{4\pi} \sigma_{\text{Rx}_i} \frac{1}{\sigma_{\text{Rx}_i}} \oint \frac{d\mathbf{l}' \times (\mathbf{r}' - \mathbf{r}_l)}{|\mathbf{r}' - \mathbf{r}_l|^3} \cdot \dot{\mathbf{m}}_{jl}(t_k) = \mathbf{g}_{li}^{\text{sc}} \sigma_{\text{Rx}_i} \cdot \dot{\mathbf{m}}_{jl}(t_k) \\ &= \mathbf{g}_{li}^{\text{sc}} \sigma_{\text{Rx}_i} \cdot [\mathbf{U}_l \mathbf{\Lambda}_l(t_k) \mathbf{U}_l^T] \cdot \mathbf{g}_{jl}^{\text{pr}} \sigma_{\text{Tx}_j} I_j, \end{aligned} \quad (92)$$

where a dot over a variable indicates its time derivative. In equations (89) and (92) the line element $d\mathbf{l}'$ lies on the x - y plane, and as a consequence the Green functions are similar in structure to those of the simple model presented in Section 2.2. Note that we have included the exciting current I_j and the transmitter and receiver areas in the definition of the signal; we have explicit knowledge of these quantities and can factor them out. If only the l -th source is illuminated, we construct the MSR matrix for the complete transmitter/receiver array by tiling $N_r \times N_t$ instances of the expression (92):

$$\mathbf{S} = \mathbf{G}^{\text{sc}} \mathbf{U}_l \mathbf{\Lambda}_l \mathbf{U}_l^T (\mathbf{G}^{\text{pr}})^T, \quad (93)$$

where the primary (or transmitter) dyad \mathbf{G}^{pr} is of size $N_t \times 3$, the secondary (or receiver) dyad \mathbf{G}^{sc} is of size $N_r \times 3$, and the response matrix $\mathbf{U}\mathbf{\Lambda}\mathbf{U}^T$ is 3×3 . When there is more than one source present, the MSR matrix of equation (93) is readily generalized:

$$\begin{aligned} \mathbf{S} &= \begin{bmatrix} \mathbf{G}_1^{\text{sc}} & \mathbf{G}_2^{\text{sc}} & \dots \end{bmatrix} \begin{bmatrix} \mathbf{U}_1 \mathbf{\Lambda}_1 \mathbf{U}_1^T & 0 & \dots \\ 0 & \mathbf{U}_2 \mathbf{\Lambda}_2 \mathbf{U}_2^T & \dots \\ \vdots & \vdots & \ddots \end{bmatrix} \begin{bmatrix} (\mathbf{G}_1^{\text{pr}})^T \\ (\mathbf{G}_2^{\text{pr}})^T \\ \vdots \end{bmatrix} \\ &= \begin{bmatrix} \mathbf{G}_1^{\text{sc}} \mathbf{U}_1 & \mathbf{G}_2^{\text{sc}} \mathbf{U}_2 & \dots \end{bmatrix} \begin{bmatrix} \mathbf{\Lambda}_1 & 0 & \dots \\ 0 & \mathbf{\Lambda}_2 & \dots \\ \vdots & \vdots & \ddots \end{bmatrix} \begin{bmatrix} (\mathbf{G}_1^{\text{pr}} \mathbf{U}_1)^T \\ (\mathbf{G}_2^{\text{pr}} \mathbf{U}_2)^T \\ \vdots \end{bmatrix}, \end{aligned} \quad (94)$$

where we see that the features intrinsic to the targets can be separated formally from the particulars of the measurement—that is, from the geometry and dimensions of the sensor and the sensor-target attitude. The array \mathbf{S} has size $N_r \times N_t$ and is square if $N_r = N_t$, as is the case with TEMTADS. This allows us to diagonalize the matrix but does not suffice to guarantee that the extracted information is useful—i.e., that the eigenvalues and eigenvectors are real, and that the latter are orthonormal. For that to hold we must have a real, symmetric matrix, which requires $\mathbf{G}_i^{\text{sc}} = \mathbf{G}_i^{\text{pr}} \equiv \mathbf{G}_i$. This cannot be rigorously true, because the receivers cannot coincide exactly with the transmitters, but holds approximately for TEMTADS if we factor the exciting current and the coil areas out of \mathbf{S} , as we did in equation (92). The diagonalization we perform is thus a particular case of a singular value decomposition (SVD), and in what follows we use “diagonalization” as shorthand for “SVD of a symmetric matrix.”

The decomposition (94) exhibits the actual polarizability elements but is not directly available to us because the Green tensors are not orthogonal. To see what we do get when we diagonalize \mathbf{S} we can perform the SVD on \mathbf{G} :

$$\mathbf{S} = \mathbf{G} \mathbf{U} \mathbf{\Lambda} \mathbf{U}^T \mathbf{G}^T = \mathbf{W} \left[\mathbf{\Sigma} \mathbf{V}^T \mathbf{U} \mathbf{\Lambda} \mathbf{U}^T \mathbf{V} \mathbf{\Sigma} \right] \mathbf{W}^T = \mathbf{W} \mathbf{Z} \mathbf{\Lambda} \mathbf{Z}^T \mathbf{W}^T = \mathbf{Y} \mathbf{\Lambda} \mathbf{Y}^T \quad (95)$$

In the intermediate step we have used the fact that the matrix within the brackets is real and symmetric and thus has a purely real eigendecomposition. Result (95) shows that the eigenvalue matrix $\mathbf{\Lambda}$, though time-dependent, is not solely composed of source responses, but also contains location and orientation information extracted from the Green tensors. The eigenvectors, likewise, include information from both the polarizabilities and the measurement particulars.

We also see in the decomposition (95) that \mathbf{S} contains an unknown “hidden dimension”— $3N$, where N is the number of sources—in the size of the block-diagonal response matrix. Numerical diagonalization (or, in general, the SVD) of \mathbf{S} will impose this middle dimension to be $N_r = N_t$. Ideally,

the method should be able to resolve up to $\lfloor N_r / 3 \rfloor$ responding sources, or eight for TEMTADS, but the actual number is lower. For one, the procedure will resolve targets only when they are spatially separated: two distinct dipoles sharing one location decrease the rank of the \mathbf{G} matrices, and hence of \mathbf{S} , by 3. In any case, diagonalization of \mathbf{S} can again let us estimate the number of targets illuminated by the sensor; since the only time-dependent quantities are the intrinsic polarizabilities of the sources, we expect the additional information provided by the time decay of the eigenvalues to be useful for classification.

The development outlined above corresponds to each time gate taken separately. To make sense of the time-dependent information we have to find a way to “follow” each of the eigenvalues as the signal decays. (A similar process must be carried out when using the dipole model for inversion.) One could in principle diagonalize the MSR matrix at each time channel, and the eigenvectors, which depend only on geometry and pose, should stay constant; however, it is not possible to know a priori the order in which the eigenvalues will be given by the diagonalization; this fact—not to mention noise and experimental uncertainty—makes it inevitable to have to disentangle the tensor elements by hand, which is easily done wrong. Instead, we explicitly look for an orthogonal matrix of eigenvectors that diagonalizes all the MSR matrices simultaneously. The procedure we employ is a generalization of the method for single matrices, and is well-known; it is sketched in next Section.

2.6.3 Algorithm for joint diagonalization

The joint diagonalization algorithm we use [31, 33, 34] is a generalization of Jacobi’s procedure to find the eigenvalues of a single matrix. Formally we set out to solve the optimization problem

$$\begin{aligned} \min_V \quad & \frac{1}{2} \sum_{q=1}^{N_g} \sum_{i \neq j} ([VA(t_q)V^T]_{ij})^2 \\ \text{s.t.} \quad & V^T V = I, \end{aligned} \tag{96}$$

which we accomplish by making repeated Givens-Jacobi similarity transformations designed to gradually accumulate the “content” of the matrices on their diagonals until a certain tolerance level is reached. The transformations are of the form $A(t_q) \rightarrow A'(t_q) = V_{rs} A(t_q) V_{rs}^T$, with the matrix V_{rs} being the identity but with the four elements V_{rr} , V_{rs} , V_{sr} , and V_{ss} replaced by the two-dimensional rotation array

$$\begin{bmatrix} \cos \phi_{rs} & \sin \phi_{rs} \\ -\sin \phi_{rs} & \cos \phi_{rs} \end{bmatrix}, \quad \text{with} \quad \tan 2\phi_{rs} = \frac{f_{rs}}{n_{rs} + \sqrt{f_{rs}^2 + n_{rs}^2}}, \tag{97}$$

where

$$n_{rs} = \sum_q \{ [a_{rr}(t_q) - a_{ss}(t_q)]^2 - [a_{rs}(t_q) + a_{sr}(t_q)]^2 \}, \quad (98)$$

$$f_{rs} = 2 \sum_q [a_{rr}(t_q) - a_{ss}(t_q)][a_{rs}(t_q) + a_{sr}(t_q)]. \quad (99)$$

The indices are swept systematically, and the procedure is repeated until convergence is reached. The computational burden is equivalent to that of diagonalizing the matrices one by one. The resulting eigenvalues and eigenvectors are all real because all the MSR matrices are symmetric.

3 Inverse Models

3.1 Introduction

Several EMI sensing and data-processing techniques [1-4, 6-9, 11, 12, 14, 15, 17, 28, 35-40] have been recently developed for detecting and discriminating between UXO and non-UXO items. Typically the first step of these methods is the recovery of a set of parameters that specify a physics-based model representing the object under interrogation. For example, in EMI sensing, the recovered parameters consist of the object's location and spatial orientation in addition to "intrinsic" parameters such as the polarizability tensor (along with some parameterization of its time-decay curve) in dipole models or the amplitudes of responding magnetic sources in the NSMS and ONVMS models. EMI responses depend nonlinearly on the subsurface object's location and orientation, therefore determining the buried object's orientation and location is a non-linear problem. In this section several inverse scattering approaches are described for EMI data inversion.

Most EMI sensors are composed of separate transmitting and receiving coils. When the operator activates the sensor, a current runs through the transmitter coils, resulting in the establishment of a ("primary" or "principal") magnetic field in the surrounding space. By Faraday's law, this time-varying magnetic field induces eddy currents in highly conducting bodies (ferromagnetic bodies also have their magnetization affected by the impinging field). These currents and magnetization in turn generate a ("secondary" or "scattered") magnetic field that also varies with time and induces measurable currents in the receiving coils. At the end, the electromagnetic data are inverted using different forward models. The procedure for estimating the location, orientation, and electromagnetic parameters of a buried object (linked in a "model vector" \mathbf{v}) is carried out by defining an objective function that quantifies the goodness-of-fit between the measured data and the predictions of the forward model. Routinely, a least-squares (LS) approach is taken to recover \mathbf{v} : formally, if \mathbf{d}^{obs} is the vector of the measured scattered field and $\mathbf{F}(\mathbf{v})$ is the solution to the forward problem, the least-squares criterion assumes the form

$$\text{minimize } \phi(\mathbf{v}) = \left\| \mathbf{d}^{\text{obs}} - \mathbf{F}(\mathbf{v}) \right\|^2. \quad (100)$$

A simple way to determine the model vector \mathbf{v} is to use the Gauss-Newton method, which starts with an initial guess \mathbf{v}_0 and updates it iteratively through

$$\mathbf{v}_{k+1} = \mathbf{v}_k + \mathbf{s}_k \quad (101)$$

where k denotes the iteration number and \mathbf{s}_k is a perturbation direction; we solve for the \mathbf{s}_k that minimizes ϕ . In many cases the LS approaches suffer from an abundance of local minima that often leads them to

make incorrect predictions of location and orientation. Global search procedures, such as differential evolution (DE) [37, 38] and genetic algorithms [39], have been recently developed to avoid this problem. We have combined the DE algorithm with the NSMS model [2] (or with the dipole model [39]) to recover locations and orientations of buried objects. Once these extrinsic properties are found we perform classification using Mixed Models (MM) and standard Matlab built-in classifiers based on maximum likelihood methods or on linear, quadratic, or Mahalanobis distances. Both gradient and global search approaches are computationally intensive because they require a massive number of forward-model evaluations and because the determination of the nonlinear elements of \mathbf{v} —the location and orientation of the object—is a nontrivial and time-consuming problem in itself. To avoid non-linear, time-consuming inversions, and by so doing streamline the inversion process, we recently developed a new physics-based approach called the HAP method and applied it to various UXO discrimination problems. The HAP method exploits an analytic relationship between the magnetic field vector \mathbf{H} , the vector potential \mathbf{A} , and the scalar magnetic potential ψ (Psi) of a hypothetical point dipole to determine the location of a visually obscured object. Of these quantities only the magnetic field (and often only one of its components) is available, and as part of this project we developed a numerical procedure based on the 2D NSMS model that replaces the measurement surface around the scatterer with a flat plane of dipoles at a (known) location intermediate between the instrument and the target. The amplitudes of these responding sources can be computed starting from high-spatial-coverage geophysical data by solving a linear system of equations and can then be used to reconstruct \mathbf{H} , \mathbf{A} , and ψ at any point on or above the measurement surface and thus to solve for the relative location \mathbf{R} and the polarizability $\bar{\bar{\mathbf{M}}}$ of the hypothetical dipole.

This chapter briefly overviews gradient-based optimization, differential evolution, and the HAP method.

3.2 Gradient-based methods of optimization

One of the most popular approaches for solving inverse problems is the gradient method [41-43]. The gradient method requires the system's Jacobian, which contains the gradients of the scattered field with respect to the unknown parameters of interest. In many cases it is impossible to determine the scattered EM field's derivatives analytically; this, however, is not a problem with either the dipole model or the NSMS model. Further, the NSMS-based inverse approach always results in an over-determined system and thus does not suffer from the ill-conditioning that usually afflicts finite-element or finite-difference time-domain methods. The EM scattering problem can be written in compact matrix form as:

$$[\mathbf{Z}]\{\Omega\} = \{H^d\} \quad (102)$$

where $[Z]$ is the scattering matrix, $\{\Omega\}$ is a vector containing the amplitudes of responding dipoles (normalized by the primary field), and $\{H^d\}$ is a vector containing the measured data over a set of points. The important point to note is that $[Z]$ in the NSMS contains explicit expressions for the responding source amplitudes $\{\Omega\}$ in terms of the object's location and orientation that can be differentiated analytically and that contain no singularities in the regions where they must be evaluated. Let us assume that α is a set of parameters (orientation, depth, etc.) that must be determined from a set of measured data [44]. A convenient way to view the problem is to define a forward map as one that associates a given α with an initial value α_0 (which serves to kick-start the inversion process). A least-squares formulation of the problem identifies a minimum of the error function by solution of the equation

$$\left[\frac{\partial H^{\text{mod}}}{\partial \alpha} \right]_{\alpha_{\beta-1}} \{\delta \alpha_{\beta}\} = [J]_{\alpha_{\beta-1}} \{\delta \alpha_{\beta}\} = \min \left(\{H^{\text{meas}}\} - \{H^{\text{mod}}(\{\alpha_{\beta-1}\})\} \right), \quad (103)$$

where $[J]_{\alpha_{\beta-1}}$ is a Jacobian matrix based on $\{\alpha_{\beta-1}\}$, β is the iteration number, the modeled values $\{H^{\text{mod}}(\{\alpha_{\beta-1}\})\}$ are predicted based on $\{\alpha_{\beta-1}\}$, and the solution $\{\delta \alpha_{\beta}\}$ is a vector of incremental steps in the unknown parameters, which are updated via

$$\{\alpha_{\beta}\} = \{\alpha_{\beta-1}\} + \{\delta \alpha_{\beta}\}. \quad (104)$$

For a case in which the EMI response from a body of revolution (BOR) is approximated using five NSMS sources, the solution vector contains 10 numbers: five describe its location and orientation, $\theta = (x_0, y_0, z_0, \theta, \varphi)$, and five more are the source amplitudes ("omega parameters"). These parameters are recovered from measurements H^{data} of the secondary magnetic field at the center of the sensor. Specifically, the parameters are found from minimization of the sum of squares (SS),

$$SS = \frac{1}{2} \sum_{i=1}^{N_{\text{exp}}} (H_i - H_i^{\text{data}})^2 \quad (105)$$

where H_i , the theoretical scattered magnetic field at each of N_{exp} measurement points, is a function of 10 parameters,

$$H_i = H_i(\theta; \Omega_1, \Omega_2, \Omega_3, \Omega_4, \Omega_5) = \sum_{k=1}^5 \Omega_k \tilde{H}_k(\theta), \quad (106)$$

assuming five belts of sources. Our model in vector notation is expressed as

$$\mathbf{h} = \mathbf{F}(\boldsymbol{\theta}) + \varepsilon, \quad (107)$$

where $\mathbf{h} \in \mathbb{R}^{L \times 1}$ is the vector of scattered magnetic field measurements at the center of the sensor (L is the total number of measurements on the grid), $\mathbf{H} = \mathbf{H}(\boldsymbol{\theta})$ is the $L \times 5$ matrix as a function of $\boldsymbol{\theta}$ and $\boldsymbol{\Omega} \in \mathbb{R}^{L \times 1}$ is the vector of normalized magnetic charges.

Below we describe three gradient-based methods for the minimization of the sum of squares.

3.2.1 Stepwise optimization

This is a traditional way to recover $\boldsymbol{\theta}$ and $\boldsymbol{\Omega}$ in alternating fashion. We start by specifying a starting value, $\boldsymbol{\theta}_0$, and compute an estimate for $\boldsymbol{\Omega}$ from linear least squares by solving the corresponding normal equations,

$$\tilde{\boldsymbol{\Omega}} = (\mathbf{H}'\mathbf{H})^{-1} \mathbf{H}'\mathbf{h}, \quad (108)$$

where the primes denote transposition. We then keep $\boldsymbol{\Omega}$ fixed at $\tilde{\boldsymbol{\Omega}}$ and perform a nonlinear regression to obtain a new estimate for $\boldsymbol{\theta}$, which we then use to find a new $\tilde{\boldsymbol{\Omega}}$ using (108), iterating until we attain convergence.

3.2.2 Simultaneous optimization

In simultaneous optimization we treat the linear $\boldsymbol{\Omega}$ parameters on the same footing as the nonlinear $\boldsymbol{\theta}$; the Jacobian thus takes the form of an $L \times 10$ matrix:

$$\mathbf{J} = \begin{bmatrix} \frac{\partial \mathbf{F}}{\partial \boldsymbol{\theta}} & \frac{\partial \mathbf{F}}{\partial \boldsymbol{\Omega}} \end{bmatrix} = \begin{bmatrix} \frac{\partial \mathbf{F}}{\partial x} & \frac{\partial \mathbf{F}}{\partial y} & \frac{\partial \mathbf{F}}{\partial z} & \frac{\partial \mathbf{F}}{\partial \varphi} & \frac{\partial \mathbf{F}}{\partial \theta} & \frac{\partial \mathbf{F}}{\partial \Omega_1} & \frac{\partial \mathbf{F}}{\partial \Omega_2} & \frac{\partial \mathbf{F}}{\partial \Omega_3} & \frac{\partial \mathbf{F}}{\partial \Omega_4} & \frac{\partial \mathbf{F}}{\partial \Omega_5} \end{bmatrix}. \quad (109)$$

3.2.3 Condensed algorithm

In this method, we use a closed-form formula to reduce the number of model parameters from 10 to one:

$$\mathbf{h} = \mathbf{F}(\boldsymbol{\theta}) + \varepsilon, \quad (110)$$

where

$$\mathbf{F}(\boldsymbol{\theta}) = \mathbf{H}(\mathbf{H}'\mathbf{H})^{-1} \mathbf{H}'\mathbf{h}. \quad (111)$$

We need the derivatives of \mathbf{F} with respect to all five components of $\boldsymbol{\theta}$; to compute them we use a matrix chain rule. Using a formula for matrix derivatives we get the derivative for a specific component of $\boldsymbol{\theta}$ as

$$\frac{\partial \mathbf{F}}{\partial \theta} = \frac{\partial \mathbf{H}}{\partial \theta} (\mathbf{H}' \mathbf{H})^{-1} \mathbf{H}' \mathbf{h} - \mathbf{H} (\mathbf{H}' \mathbf{H})^{-1} \left(\frac{\partial \mathbf{H}'}{\partial \theta} \mathbf{H} + \mathbf{H}' \frac{\partial \mathbf{H}}{\partial \theta} \right) (\mathbf{H}' \mathbf{H})^{-1} \mathbf{H}' \mathbf{h} + \mathbf{H} (\mathbf{H}' \mathbf{H})^{-1} \frac{\partial \mathbf{H}'}{\partial \theta} \mathbf{h} \quad (112)$$

Combining the five derivatives we get the $L \times 5$ total Jacobian

$$\mathbf{J} = \left[\frac{\partial \mathbf{F}}{\partial x}, \frac{\partial \mathbf{F}}{\partial y}, \frac{\partial \mathbf{F}}{\partial z}, \frac{\partial \mathbf{F}}{\partial \varphi}, \frac{\partial \mathbf{F}}{\partial \theta} \right] \quad (113)$$

and the Gauss-Newton algorithm takes the form

$$\boldsymbol{\theta}_{s+1} = \boldsymbol{\theta}_s + (\mathbf{J}'_s \mathbf{J}_s)^{-1} \mathbf{J}'_s \mathbf{h} \quad (114)$$

to be iterated until reaching convergence.

3.3 Differential evolution

Differential evolution (DE) [37, 38], one of the global-search algorithms recently developed to bypass the local-minima problem that often leads standard gradient-search approaches to make incorrect predictions for location and orientation, is a heuristic, parallel, direct-search method for minimizing nonlinear functions of continuous variables. Similar in concept to the genetic algorithms that have been used with much success on problems with discrete variables, DE is easy to implement and has good convergence properties.

We have combined the DE algorithm with the above-discussed dipole, NSMS, and ONVMS techniques to invert digital geophysical EMI data following a procedure reminiscent of the stepwise optimization described in the previous section. The scattered field from any object whose location and orientation are known depends linearly on the magnitudes of its responding sources, and the procedure starts by giving initial values of the attitude parameters and using these estimates, along with the measured data, to determine the source amplitudes by solving a linear system of equations. The amplitudes thus found are fed into a nonlinear objective function that quantifies the mismatch between measured data and model predictions and whose (DE-determined) minimum serves to refine the estimates for location and orientation. The procedure continues to alternate between these linear and nonlinear stages until it reaches convergence (or a preset maximum number of iterations). The responding amplitudes are then stored and used in a later classification step, while the location and orientation parameters are used during target excavation.

Differential evolution uses N_p -dimensional parameter vectors \mathbf{v} ,

$$\mathbf{v}_{p,G}, p=1,2, \dots, N_p \quad (115)$$

where G is a generation/iteration index. In our case $\mathbf{v} = \{x_0, y_0, z_0, \theta, \phi\}$; the first three are the object's location and the other two are the polar (θ) and azimuthal (ϕ) Euler angles that define its orientation (by using only two angles we are assuming that UXO are effectively BOR). The objective function to be minimized is defined as

$$F(\mathbf{v}) = \frac{1}{(MN_f)^2} \sum_{m=1}^M \sum_{f=1}^{N_f} |H_{m,f}^{\text{sc}}(\mathbf{v}) - H_{m,f}^{\text{data}}(\mathbf{v})|^2, \quad (116)$$

where $H_{m,f}^{\text{sc}}(\mathbf{v})$ and $H_{m,f}^{\text{data}}$ are respectively the theoretical prediction (for vector \mathbf{v}) and the measured magnetic field data at the m -th measurement point (of M) and the f -th frequency or time point (of N_f). The DE optimization process itself can be subdivided into three steps:

1) The first step creates random initial populations $\mathbf{v}_{p,G}, p=1,2, \dots, N_p$, that span the entire parameter space. For a given $\mathbf{v}_{p,G}$ in the generation, a linear system of equations is constructed by matching measured data to the secondary magnetic field from (106). This system is linear in Ω_i and is solved directly for those parameters.

2) The second step, which requires the most execution time, is the calculation of the secondary magnetic field (106) for each of the $\mathbf{v}_{p,G}$. When the NSMS (or ONVMS) model is used, the calculation for each $\mathbf{v}_{p,G}$ requires a fraction of the time required to execute any other proposed 3D forward model; this relative computational efficiency makes NSMS (or ONVMS) an attractive alternative for performing real-time inversion.

3) Next comes the evaluation of the cost function for each population member and the storage of the best sets of parameters. At each step, the DE algorithm produces an estimate of position and orientation. By examining and sorting the cost function at each step, the best-half of the population is chosen as the next generation's parameters, whereas the bottom half is discarded. Thereafter the next generation is created by taking the parameters in the previous generation and applying crossover and mutation operations on them. The three steps are repeated until the maximum number of generations has been reached or until the objective function reaches a desired value. Rules for using DE are discussed in more detail elsewhere [37, 38].

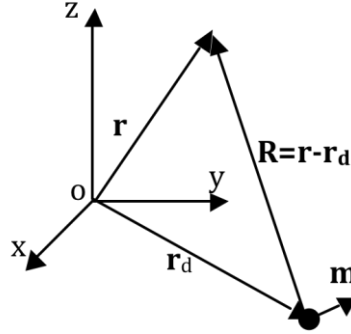


Figure 12: The HAP approach for a dipole.

3.4 The HAP method

3.4.1 Estimating the location and orientation of buried objects

In the EMI regime, the secondary magnetic fields measured by the EMI receivers are induced by eddy currents or magnetic dipoles which are distributed non-uniformly inside the scatterer. There are some particular points, named “scattered field singularities” (SFS), where most of these sources are concentrated. Recent studies show that under certain conditions the entire scatterer can be replaced with several responding elementary sources by putting them at SFS points [45-52]. The mathematical and physical properties of SFS and its applications to EM scattering problems are very well documented, and their study is known in the literature as “*Catastrophe Theory*” [45, 46]. Our objective has been to determine the locations of the SFS from data without solving traditional ill-posed inverse-scattering problems. We have found a new analytic expression for estimating the location, orientation, and polarizability elements of a buried object starting from measured EMI data. The algorithm (dubbed “HAP” [53]) is based on the fact that a target’s response can be approximated by dipole sources concentrated at SFS points. It utilizes three global values at a single location in space: (1) the magnetic field vector \mathbf{H} , (2) the vector potential \mathbf{A} , and (3) the scalar magnetic potential ψ . Since among these quantities only the \mathbf{H} field (and sometimes only one of its components) is measurable, we employ a variation of the NSMS model to obtain \mathbf{A} and ψ we distribute elementary sources on an auxiliary planar layer, located between the sensor and the object, and find their amplitudes by fitting measured data.

The magnetic field \mathbf{H} and the scalar (ψ) and vector (\mathbf{A}) potentials of a magnetic dipole are

$$\mathbf{H} = \frac{e^{jkR}}{4\pi R^3} \left[\left(\frac{3\mathbf{R}(\mathbf{R} \cdot \mathbf{m})}{R^2} - \mathbf{m} \right) (1 - jkR) - k^2 (\mathbf{R} \times (\mathbf{R} \times \mathbf{m})) \right], \quad (117)$$

$$\psi = \frac{(\mathbf{R} \cdot \mathbf{m})}{4\pi R^3} (1 - jkR) e^{jkR}, \quad (118)$$

$$\mathbf{A} = -\mu_0 \frac{\mathbf{m} \times \mathbf{R}}{4\pi R^3} (1 - jkR) e^{jkR} \equiv -\mu_0 \frac{\mathbf{m} \times \mathbf{R}}{R^3} G(R), \quad \text{where} \quad G(R) = \frac{e^{jkR}}{4\pi} (1 - jkR) \quad (119)$$

where k is the wave number in the surrounding medium, $\mathbf{R} = \mathbf{r} - \mathbf{r}_d$, \mathbf{r} is an observation point, and \mathbf{r}_d is the location of the dipole [51] (Figure 12). Note that the magnetic field (117) has terms that decay as R^{-1} , R^{-2} , and R^{-3} . The range $kR \gg 1$ is referred to as the far zone, and fields in this range are referred to as being in the far field. Similarly, fields in the near zone $kR \ll 1$ are referred to as being in the near field, and the zone $kR \approx 1$ is called intermediate zone. Typically, UXO detection and discrimination are conducted in the near zone. In addition, in the EMI regime displacement currents are considered irrelevant, which means that the contribution of the k^2 term in equation (117) can be set to zero. Making this assumption, taking the dot product of (117) with \mathbf{R} , and using (118) we get that

$$\mathbf{H} \cdot \mathbf{R} = \mathbf{H} \cdot (\mathbf{r} - \mathbf{r}_d) = \frac{1}{R^3} \left(\frac{3\mathbf{R}(\mathbf{R} \cdot \mathbf{m})}{R^2} - \mathbf{m} \right) \cdot \mathbf{R} G(R) = 2 \frac{\mathbf{R} \cdot \mathbf{m}}{R^3} G(R) = 2\psi. \quad (120)$$

Similarly, taking the cross product of (117) and \mathbf{R} and using (119) we obtain

$$\mathbf{H} \times \mathbf{R} = G(R) \frac{1}{R^3} \left(\frac{3\mathbf{R}(\mathbf{R} \cdot \mathbf{m})}{R^2} - \mathbf{m} \right) \times \mathbf{R} = -G(R) \frac{\mathbf{m} \times \mathbf{R}}{R^3} = \frac{\mathbf{A}}{\mu_0}. \quad (121)$$

Now, the cross product of \mathbf{H} and (121) gives

$$\left[\mathbf{H} \times \frac{\mathbf{A}}{\mu_0} \right] = \mathbf{H} \times [\mathbf{H} \times \mathbf{R}] = \mathbf{H}(\mathbf{H} \cdot \mathbf{R}) - \mathbf{R} |\mathbf{H}|^2 = 2\mathbf{H} \psi - \mathbf{R} |\mathbf{H}|^2, \quad (122)$$

which allows us to solve for \mathbf{R} :

$$\mathbf{R} = \frac{2\mathbf{H} \psi - [\mathbf{H} \times \mathbf{A} / \mu_0]}{|\mathbf{H}|^2}. \quad (123)$$

The location \mathbf{R} of the responding dipole is seen to be independent of the frequency. In other words, as long as MQS assumptions hold, equation (123) is valid when the dipole is in free space and equally well when it is embedded in a conducting medium such as seawater. Also note that \mathbf{R} is determined as a ratio, which makes the expression (123) partially tolerant to noise due to scaling arguments, since \mathbf{A} and ψ are dependent on the \mathbf{H} field (see equations (120) and (121)). Taking the

cross product of \mathbf{R} and (121) from the left side and using equation (120) we obtain an expression for the dipole moment \mathbf{m} :

$$\mathbf{m} = \frac{R}{G(\mathbf{R})} \left(\mathbf{R}\psi + [\mathbf{A} / \mu_o \times \mathbf{R}] \right) \quad (124)$$

with \mathbf{R} previously determined from equation (123).

3.4.2 A simplified HAP method

It is possible to simplify the HAP method by eliminating the need for the vector potential. We rewrite equation (120) as

$$\mathbf{H} \cdot \mathbf{r}_d = -2\psi + \mathbf{H} \cdot \mathbf{r}, \quad (125)$$

which provides a least-squares estimate of \mathbf{r}_d when evaluated at N distinct observation points:

$$\begin{bmatrix} H_x(\mathbf{r}_1) & H_y(\mathbf{r}_1) & H_z(\mathbf{r}_1) \\ H_x(\mathbf{r}_2) & H_y(\mathbf{r}_2) & H_z(\mathbf{r}_2) \\ \vdots & \vdots & \vdots \\ H_x(\mathbf{r}_N) & H_y(\mathbf{r}_N) & H_z(\mathbf{r}_N) \end{bmatrix} \begin{bmatrix} x_d \\ y_d \\ z_d \end{bmatrix} = \begin{bmatrix} -2\psi(\mathbf{r}_1) + \mathbf{H}(\mathbf{r}_1) \cdot \mathbf{r}_1 \\ -2\psi(\mathbf{r}_2) + \mathbf{H}(\mathbf{r}_2) \cdot \mathbf{r}_2 \\ \mathbf{M} \\ -2\psi(\mathbf{r}_N) + \mathbf{H}(\mathbf{r}_N) \cdot \mathbf{r}_N \end{bmatrix}. \quad (126)$$

3.4.3 Determining the HAP amplitudes

To construct the potentials (and the other field components, if unavailable) we assume that the field is produced by a surface distribution of magnetic charge $q(s')$ spread on a fictitious plane located just below the ground (Figure 13). The positions $\mathbf{r}_{s'}$ of the sources are fixed and known by construction, and the field can be expressed as the matrix-vector product

$$H_z(\mathbf{r}) = \int \frac{q(s')}{4\pi} \frac{z - z_{s'}}{|\mathbf{r} - \mathbf{r}_{s'}|^3} ds' \equiv \vec{\mathbf{Z}}_z \cdot \mathbf{q} \quad (127)$$

by employing a quadrature scheme. To determine the array q of charges we minimize the difference between model predictions and collected data \mathbf{H}^{meas} at a set of known points:

$$\mathbf{q} = \arg \min \frac{1}{2} \left(\vec{\mathbf{Z}}_z \cdot \mathbf{q} - \mathbf{H}_z^{\text{meas}} \right)^2 = \left[\vec{\mathbf{Z}}_z^T \cdot \vec{\mathbf{Z}}_z \right]^{-1} \left[\vec{\mathbf{Z}}_z^T \cdot \mathbf{H}_z^{\text{meas}} \right], \quad (128)$$

where each matrix row corresponds to a different measurement point and each column to a subsurface of the underground virtual source layer. The potential is then found from

$$\psi(\mathbf{r}) = \int \frac{q(s')}{4\pi|\mathbf{r} - \mathbf{r}_{s'}|} ds' \equiv \vec{\mathbf{Z}}_{\psi} \cdot \mathbf{q}. \quad (129)$$

Current EMI sensors operate in both monostatic and multistatic modes. Monostatic sensors, such as the Geophex frequency-domain GEM-3 instrument [50] and the Geonics EM-61 and EM-63 time-domain instruments [49] have collocated transmitter and receiver coils, whereas multistatic sensors like the MPV time-domain instrument [36] and the Berkeley UXO Discriminator (BUD) [54] have multiple transmitters or multiple receiver coils or both. We have implemented numerical procedures to estimate the vector and scalar magnetic potentials starting from multi-static or mono-static EMI data. For bistatic data we determine the potentials as described above; for the monostatic case we normalize the amplitudes of the responding auxiliary sources by the primary magnetic field. The procedure is discussed in further detail in [53].

It is worth reiterating that the HAP method replaces the scatterer with a point dipole, and is thus based on a rather drastic simplification; yet it provides acceptable location estimates because the sources within the target that produce the scattered field tend to concentrate at a set of “scattered field singularities” [48, 52]. The locations of these singularities change at every measurement point, since the primary field of the sensor also changes; the HAP method takes these variations into account and outputs an average location as a result.

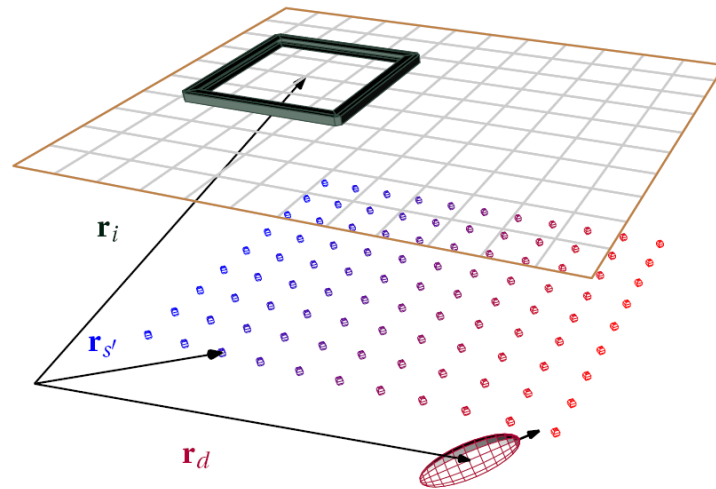


Figure 13: Determining the location and orientation of a buried target. The method assumes the object is a point dipole and exploits an analytic relation between the field measured at \mathbf{r}_i and the scalar potential at the same point to find the location \mathbf{r}_d . The potential is constructed using a layer of equivalent magnetic sources placed between the sensor and the object; $\mathbf{r}_{s'}$ is a typical location on the layer.

3.4.4 The HAP method with gradient information

The HAP technique can be simplified further by reducing the formulation such that it only requires the magnetic field and its gradient, both of which are measurable by current sensors. After taking the gradient of equation (120) with respect to the x -, y -, and z -coordinates, we obtain

$$\begin{cases} x_d \frac{\partial H_x}{\partial x} + y_d \frac{\partial H_y}{\partial x} + z_d \frac{\partial H_z}{\partial x} = 3H_x + x \frac{\partial H_x}{\partial x} + y \frac{\partial H_y}{\partial x} + z \frac{\partial H_z}{\partial x} \\ x_d \frac{\partial H_x}{\partial y} + y_d \frac{\partial H_y}{\partial y} + z_d \frac{\partial H_z}{\partial y} = 3H_y + x \frac{\partial H_x}{\partial y} + y \frac{\partial H_y}{\partial y} + z \frac{\partial H_z}{\partial y} \\ x_d \frac{\partial H_x}{\partial z} + y_d \frac{\partial H_y}{\partial z} + z_d \frac{\partial H_z}{\partial z} = 3H_z + x \frac{\partial H_x}{\partial z} + y \frac{\partial H_y}{\partial z} + z \frac{\partial H_z}{\partial z} \end{cases} \quad (130)$$

Thus, in order to determine the target's location we need only the magnetic field \mathbf{H} and its gradient at a given point in space.

To further illustrate the applicability of the HAP method in real field conditions, we investigate the performance of the technique for a case in which signals are contaminated with additive sensor noise. We generate synthetic scattered-field data using the (spheroidal) standardized excitation approach (SEA). The analysis is done for an 81-mm UXO for which the amplitudes of a reduced set of responding sources were determined and stored in a library. Using these sources we generated the object's EMI response on a 11×11 measurement grid to the primary field of the (monostatic) EM-63 sensor. These responses are depicted on Figure 2.19, upper left; the target was placed at a depth of 35 cm and oriented horizontally. To replicate the conditions of a EM-63 survey we calculated only one component (H_z) of the scattered magnetic field. The 2D NSMS layer was placed under the measurement grid and the amplitudes of the NSMS were determined, after which the magnetic field and scalar magnetic potential were determined for 26 time channels. The target position was estimated using the HAP technique. The inverted results are depicted on Figure 2.19. The results show that the HAP method reconstructs the position very well. We then added random Gaussian noise to the field reading at every position; the results appear in Figure 2.19 upper right. The object's position was inverted from the noisy data by applying the same numerical procedure. The inverted results are depicted on Figure 2.19 with red circles. We see that even with noisy data the method does a very good job of predicting the object's position, in particular its depth.

3.4.5 Estimating object location using measured monostatic and multistatic EMI data

3.4.5.1 a. Frequency-domain EMI data

In this section we apply our approach to monostatic GEM-3 data. We first compare the predicted EMI magnetic field computed via the NSMS fictitious source layer to measured data. In these tests, the NSMS model is used to predict the scattered magnetic field components H_x and H_y using only monostatic measured magnetic field data. The tests are done for a steel sphere of radius $a = 3.75$ cm.

The data were collected at two elevations: $h_1 = 21$ cm and $h_2 = 26$ cm using the new Geophex GEM-3D+ sensor. Here h_1 and h_2 are measured from the sphere's center to the measurement surface. The GEM-3D+ sensor consists of two transmitter loops and three orthogonal receivers (Figure 15). The currents in the transmitter loops circulate in opposite directions and are scaled so that their respective primary fields cancel at their common center, where the receiving coils are located. In the numerical model, the transmitter loops are idealized as infinitely thin loop sources of radii a_1 and a_2 , with currents $I_2 = -I_1 a_2/a_1$. At each elevation, the EMI field is measured on an 81-point grid at 5-cm increments.

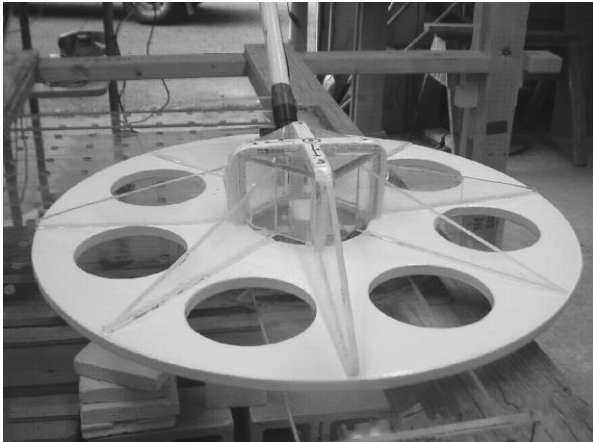


Figure 15. The GEM-3D+ sensor head showing the transverse receiver coils.

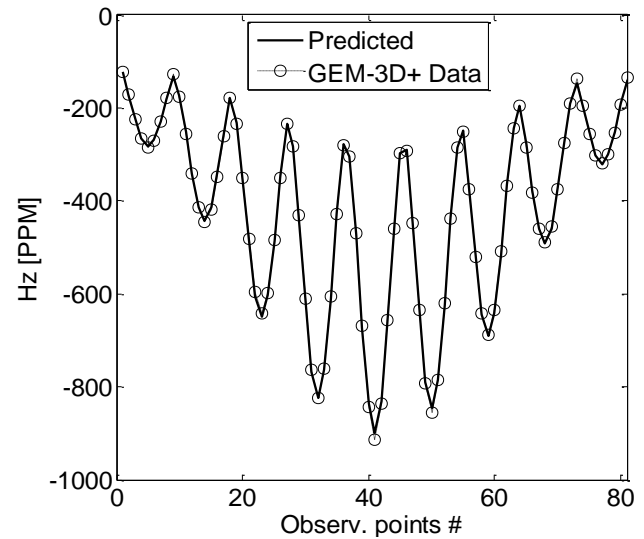


Figure 14. Comparisons between actual and modeled H_z data.

The scattered magnetic field is modeled as a superposition of the magnetic field produced by a set of normalized magnetic dipoles placed on a fictitious surface just below the actual measurement grid. The fictitious surface is divided into small patches (*cf.* Figure 13). At each patch the primary magnetic field is determined. The amplitudes of the responding magnetic dipoles on each subsurface are scaled by the primary magnetic field using (117). The amplitudes of the responding surface layer NSMS are then determined by matching the z -component of the modeled magnetic field to its measured counterpart at the

grid points with a sensor elevation h_1 . Once the amplitudes are found, the secondary field quantities $\tilde{\mathbf{H}}_1^{\text{sc}}$, $\tilde{\mathbf{A}}_1^{\text{sc}}$, and $\tilde{\psi}_1^{\text{sc}}$ can be found anywhere above the fictitious surface. Note that the auxiliary NSMS layer is placed between the object and the measurement plane. In this arrangement, the NSMS surface sources represents the magnetic fields radiated by all metallic objects distributed beneath the fictitious surface.

The NSMS sources were distributed on a 5×5 grid at an elevation $h = 10.5$ cm. The spacing between sources in this case was 10 cm. The NSMS modeled magnetic field is matched to the measured data at the elevation $h_1 = 21$ cm. The results appear in (Figure 14). The surface- distributed NSMS sources do a good job of predicting the EM signal at h_1 . After determining the amplitudes of the NSMS we can compute the x - and y -components of the scattered monostatic magnetic field at 9×9 grid points at the elevation $h_2 = 26$ cm, where the GEM-3D+ data were collected. The results appear in Figure 16. The NSMS dipoles can be seen to predict H_x and H_y of the scattered magnetic field at elevation h_2 using only the H_z of the scattered magnetic field data at h_1 .

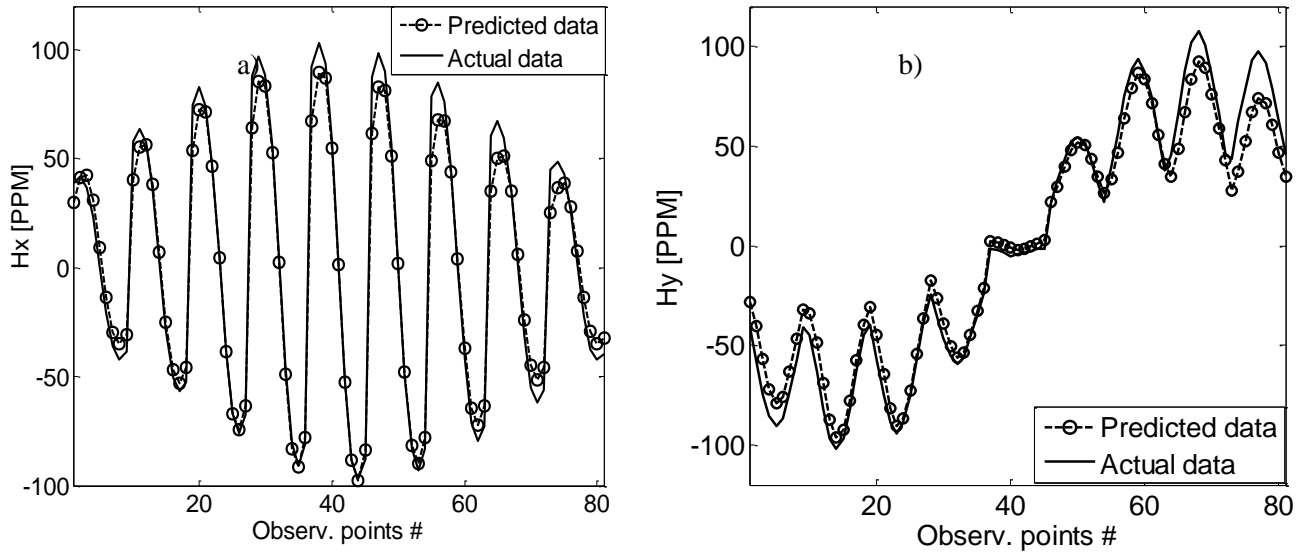


Figure 16. Comparisons between actual and predicted data for a sphere subject to GEM-3D+ excitation: (a) x -component, (b) y -component

Similarly, using these amplitudes of the NSMS layer we estimate the vector and scalar potentials $\tilde{\mathbf{A}}_1^{\text{sc}}$ and $\tilde{\psi}_1^{\text{sc}}$ at the same 9×9 grid at elevation $h_2 = 26$ cm in order to determine the coordinates of the center of

the sphere using (2.7). The predicted $\sqrt{x_c^2 + y_c^2}$ and z_c are depicted in Figure 17. The results illustrate that the algorithm can predict the object's location from actual H_z data.

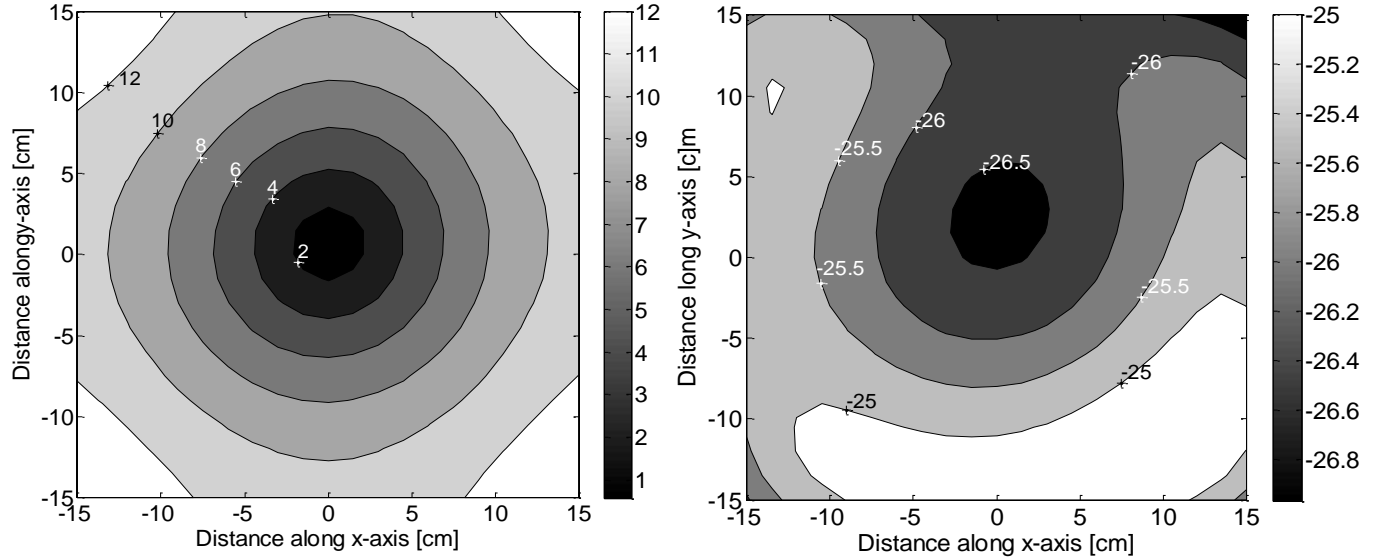
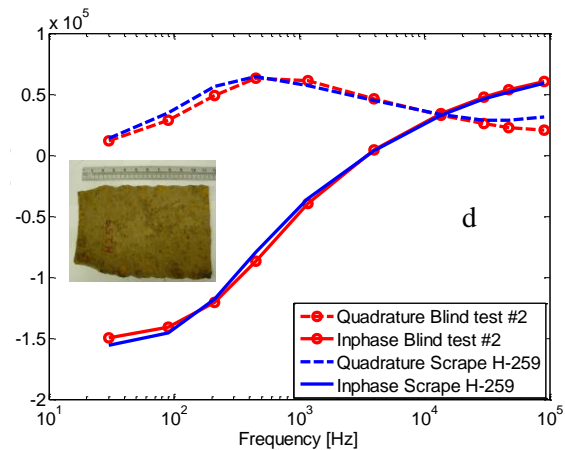
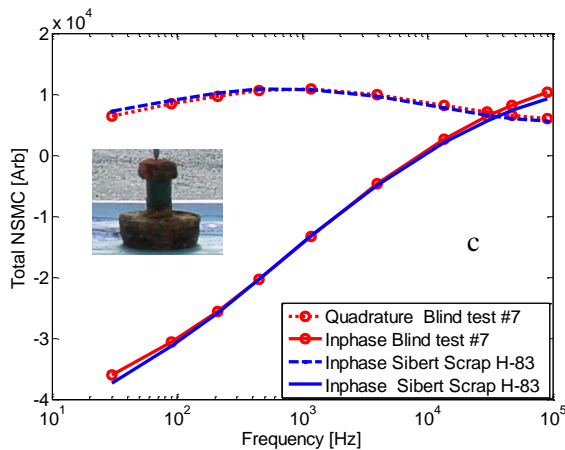
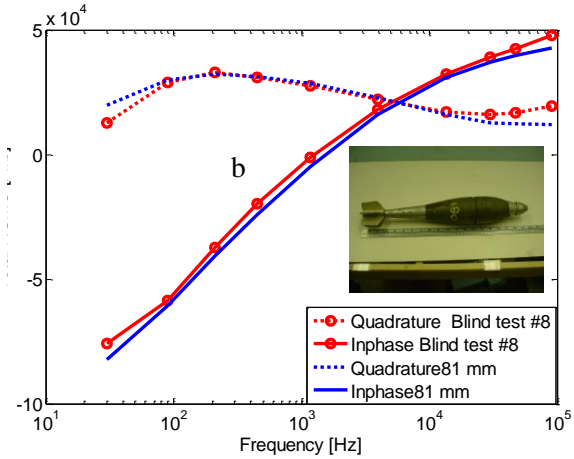
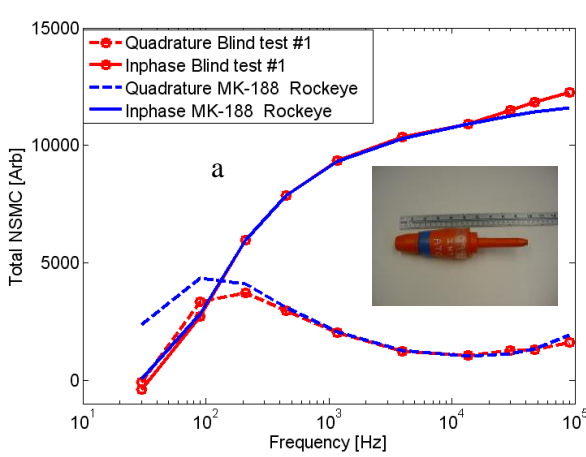


Figure 17. Estimated $\sqrt{x_c^2 + y_c^2}$ (left) and z_c (right) for the steel sphere. The true $z_c = 26$ cm.

To demonstrate the superior performance of the HAP technique combined with the NSMS approach, we apply the algorithm to frequency-domain GEM-3D+ blind-test data. These were collected for eight targets, of which three were clutter and five were UXO: a BLU-26 bomblet, a Rockeye, an 81-mm projectile, a 60-mm mortar, and a 57-mm bullet. For all these items detailed data were collected under controlled conditions, which were used to determine the total NSMS $Q(f)$ for each target. We then determined the locations and orientations of the objects using the HAP algorithm. The true and estimated locations and orientations of the targets are given in Table 1. Estimated and actual positions and orientations for the GEM-3D+ blind-test data runs. The results show that inverted and true values of position and orientation are in general very close. After that we calculated the total NSMS for each of the eight objects and compared them to the total NSMS values stored in a library of six UXO items. In all cases the inverted NSMS closely matches its corresponding UXO items (see Figure 18), which means that the algorithm was able to identify all items with 100% accuracy.

Table 1. Estimated and actual positions and orientations for the GEM-3D+ blind-test data runs.

Blind test #	Estimated (Actual)				
	θ ($^{\circ}$)	ϕ ($^{\circ}$)	x_0 (cm)	y_0 (cm)	z_0 (cm)
1	93.60 (45)	90.0 (90)	3.0 (0)	0.01(1.5)	-29.68(-28)
2	86.17 (90)	20.9 (135)	-5.5 (-5)	5.03(5)	-34.46(-31)
3	105.36 (0)	76.4 (arb)	-15.6 (-20)	-15.8 (-15)	-43.46(-42)
4	91.08 (arb)	2.25(arb)	18.2 (20)	-0.5 (0)	-25.19(-22)
5	81.05 (135)	10.11(135)	20.2 (15)	-0.7 (5)	-26.22(-26)
6	86.34 (180)	67.05(arb)	5.3 (10)	-12.64(-20)	-20.25(-18)
7	65.56 (90)	16.63(45)	12.9 (18)	4.13(12)	-25.81(-20)
8	66.06 (90)	14.01(90)	3.35 (5)	15.45(10)	-43.10(-40)



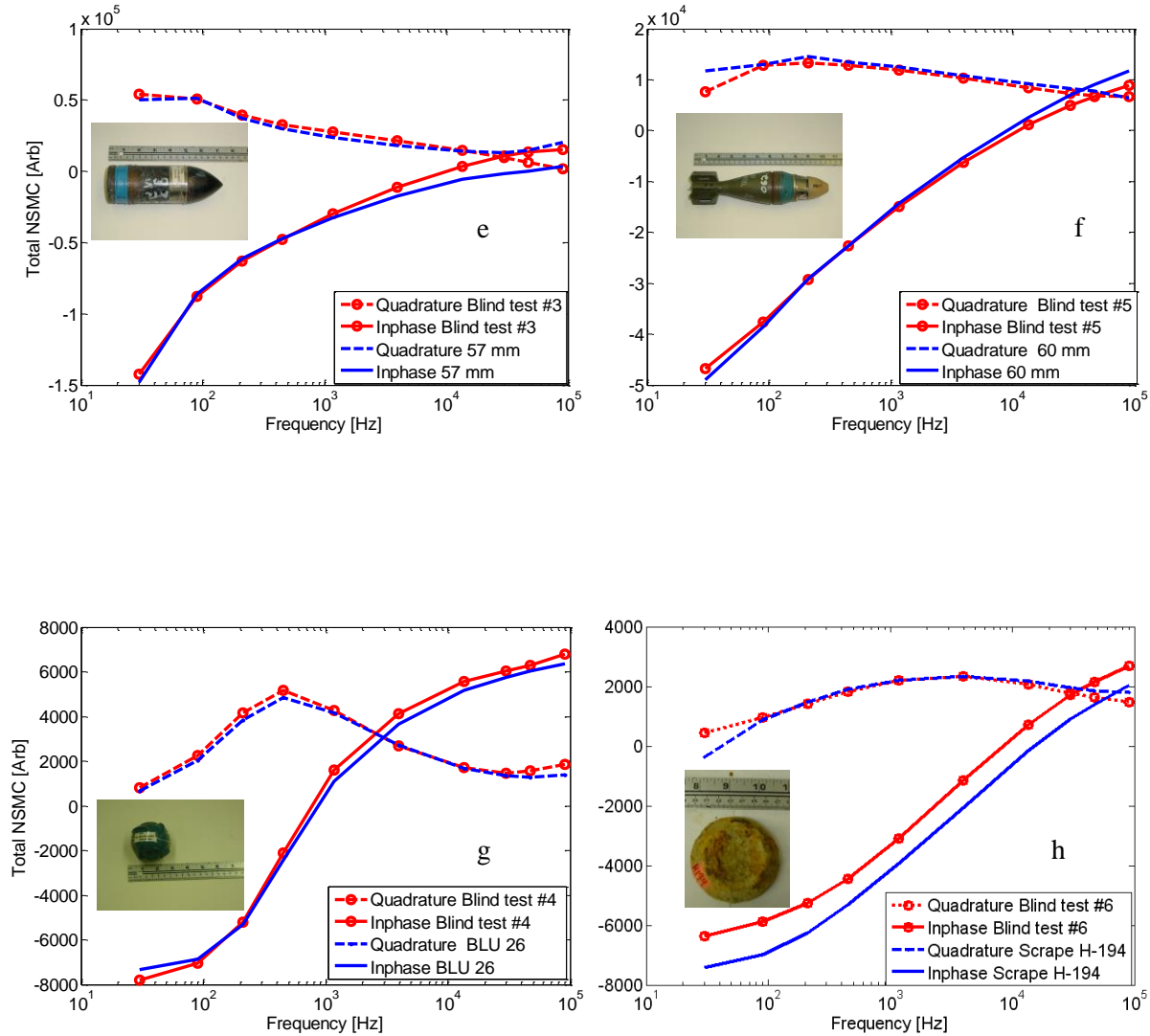


Figure 18. Comparison between GEM-3D+ blind tests inversions and library NSMS.

3.4.5.2 Time-domain EMI-63 data

The algorithm was also applied to data from the time domain EM-63 sensor made by Geonics LTD. The EM-63 sensor consists of a $1\text{ m} \times 1\text{ m}$ square transmitter loop and two receiver loops: (1) the main receiver loop is $0.5\text{ m} \times 0.5\text{ m}$ in size with a center that coincides with the transmitter coil's center, and (2) the same size receiver loop that is placed 60 cm above the main receiver coil. These receivers measure the complete transient response from $180\text{ }\mu\text{s}$ to 25 ms. The time-domain measurements were conducted at the UXO test-stand at the U.S. Army Corps of Engineers, Engineer Research and Development Center (ERDC) Laboratory, Vicksburg, MS. The measurement platform, which is made with nonmetallic fiberglass materials, has a usable measurement area of $3 \times 4\text{ m}$ in extent. The sensor is

mounted on a robotic arm that can be moved and controlled around the measurement area using software running on a remote personal computer. Automated remote controls are used to position an ordnance item at an accurate depth (within 1 cm) below the measurement area. The sensor can be positioned with an accuracy of approximately 1 mm.

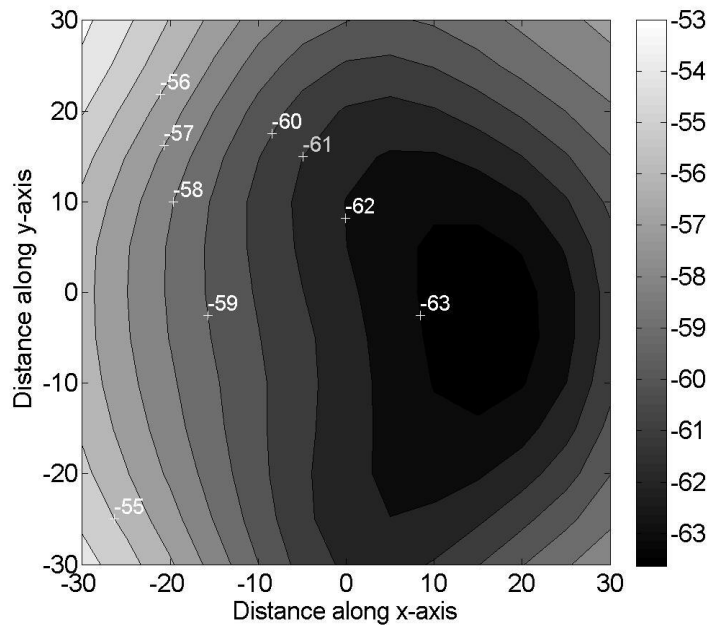


Figure 19. Estimated z_c for the 81-mm UXO. The true $z_c = 60$ cm.

The time domain data were collected at a $h = 60$ cm elevation at 441 points for a horizontally oriented 81-mm UXO. Again, the scattered magnetic field is modeled as a superposition of the magnetic field produced by a set of surface magnetic dipoles placed on a fictitious surface just 20 cm below the real surface. After determining the amplitudes of the NSMS on this surface, the magnetic field and the potentials are estimated, and the object's location is approximated using the method presented here. The estimated z_c location of the object's center is depicted on Figure 19, and the good agreement indicates that the proposed approach is applicable for TD EMI data as well. These results were obtained using only the first time channel, but our studies indicate that other time channels produce similar results. Multiple data channels can simultaneously be used to obtain more reliable estimates of the object's position.

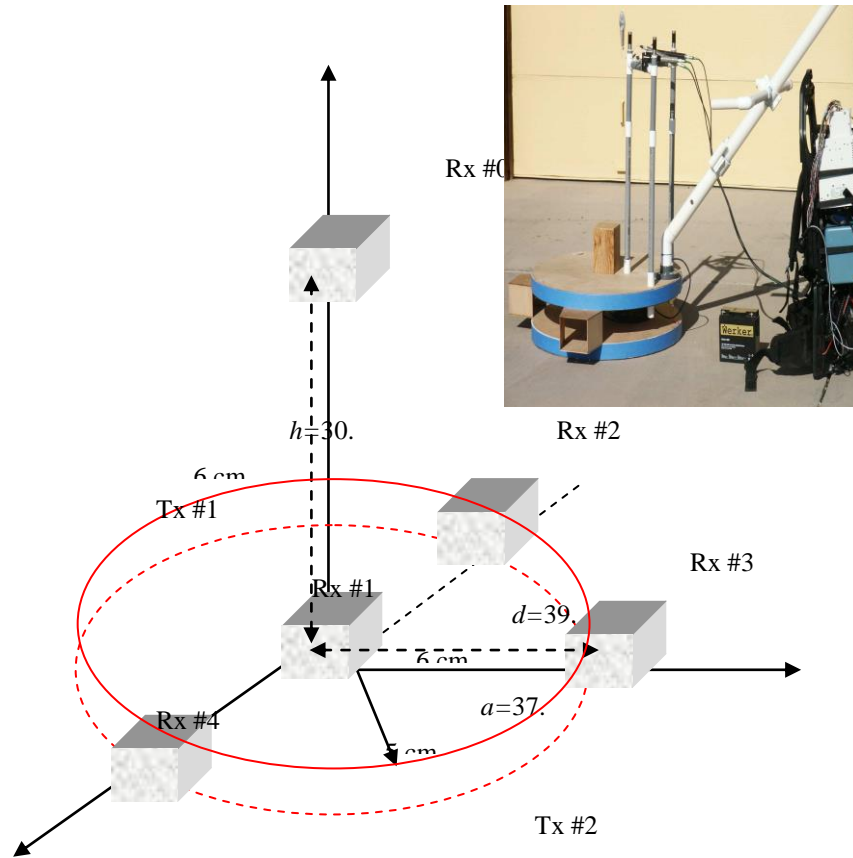


Figure 20. Actual and schematic diagram of the MPV-TD sensor

3.4.5.3 MPV-TD data blind-test analysis

We also tested the NSMS technique and the HAP approach using TD MPV sensor data. The MPV TD sensor consists of two transmitter loops with 37.5-cm radii and five triaxial receiver loops/cubes (see Figure 20). The receivers are located as follows: Cube #0 upper center; Cube #1 lower center; Cube #2 left of center ($x = -39.6$ cm); Cube #3 forward of center ($y = 39.6$ cm); and Cube #4 right of center ($x = 39.6$ cm). These receivers accurately measure the complete transient response over a wide dynamic range of time going from $100 \mu\text{s}$ to 25 ms. The measurements were conducted by G&G personnel at the UXO test stand of the USACE-ERDC Laboratory in Vicksburg, MS. The measurement platform, which is made of nonmetallic fiberglass materials, has a usable measurement area of 3×4 m in extent. The sensor is mounted on a robotic arm that can be moved and controlled around the measurement

area using software running on a personal computer. Automated remote controls are used to position ordnance items at an accurate depth (to within 1 cm) below the measurement area. The sensor can be positioned with an accuracy of approximately 1 mm. All data presented here were collected by personnel from G&G Sciences Inc. The data were collected on an 89 point grid for objects at different orientations and depths. The response of each object was represented with only five NSMS belts.

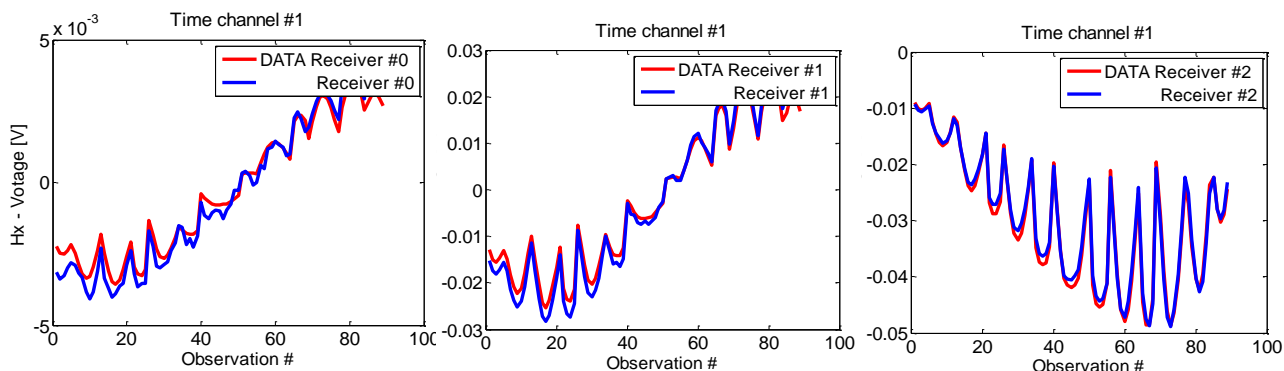


Figure 21. Predicted and actual TD MPV data for a 60-mm UXO.

We first test the accuracy of the NSMS technique against well controlled test-stand data for a 60-mm UXO. Figure 21 compares predicted and actual data at a fixed time gate for the x components of the scattered magnetic fields as measured by three receivers (Cubes #0, 1, and 2; see Figure 2.26). The results clearly show that the NSMS can predict the EMI response of the 60-mm UXO.

Once the accuracy of the NSMS has been established, we proceed to apply the technique to TD-MPV blind test data. These blind test data were collected for five unidentified targets at CRREL facilities by CRREL personnel using the MPV. The test objects considered were five UXO (a BLU-26 bomblet, 105-mm and 81-mm projectiles, a 60-mm mortar, and a 57-mm bullet) for which very detailed data were collected under controlled conditions at the USACE-ERDC test site in Vicksburg. Using those data sets we determined the total NSMS $Q(t)$ values for the known UXO. Target EMI responses were measured over 34 grid points at two elevations, but in this study only data at one elevation were used. First, the locations and orientations of the objects were determined using the new algorithm. The true locations and orientations of the five targets are given in Table 2; the inverted estimates are summarized in Table 3.

The comparison between inverted and true values for position and orientation shows that the predicted values in general are very close to the true values. Sometimes the azimuthal angle ϕ is seen to be flipped; this is mainly due to BOR symmetry and does not constitute an error.

Once the targets' locations and orientations were determined we computed the total NSMS for the five objects and compared them to the five total NSMS values stored in the library of UXO items. Comparisons between the total NSMC Target #1 and those of the library UXO are depicted in Figure 22. Note that the NSMS library was created using TD MPV data collected at the UXO test-stand site when the objects were oriented horizontally (dip = 90°) with respect to the measurement grid. The comparison shows that the total NSMS (a scalar discriminator) is directly related to the object's size and material properties: as the size of the object increases so does the total NSMS amplitude. In addition, the inverted total NSMS for Target #1 correctly identified the actual target. This demonstrates that the total NSMS is independent of the target's location and orientation and is characteristic of the object. In this test we used TD-MPV data collected at 17 points and one elevation.

Table 2. Ground truth for the MPV-TD blind-test data runs.

Target	ID	x0 (cm)	y0 (cm)	z0 (cm)	ϕ (°)	dip (°)
1	81-mm	-23.26	22.5	56.16	0	18.3
2	105-mm	-20.26	22.5	69.14	180	18.6
3	BLU-26	0.00	22.5	43.21	0	0.0
4	57-mm	5.22	22.5	51.45	180	306.6
5	60 -mm	0.00	22.5	54.50	0	0.0

Table 3. Inverted results for position and orientation for MPV-TD blind-test data. Numbers with an asterisk are arbitrary due to BOR considerations.

ID		y0 (cm)	z0 (cm)	ϕ (°)	dip (°)
1	81-mm	23.6	56.56	0	-2
2	105 mm	23.7	67.57	170	-20.8
3	BLU-26	22.8	47.55	*0	*180.0
4	57-mm	22.6	58.19	0	320.4
5	60- mm	19.3	54.02	*3	0.0

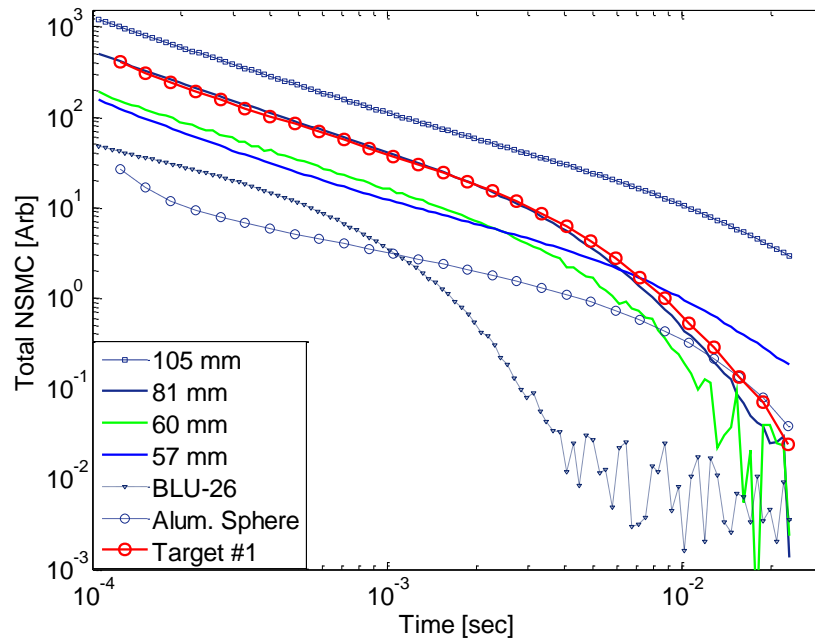


Figure 22. NSMS model comparison to library for Target #1.

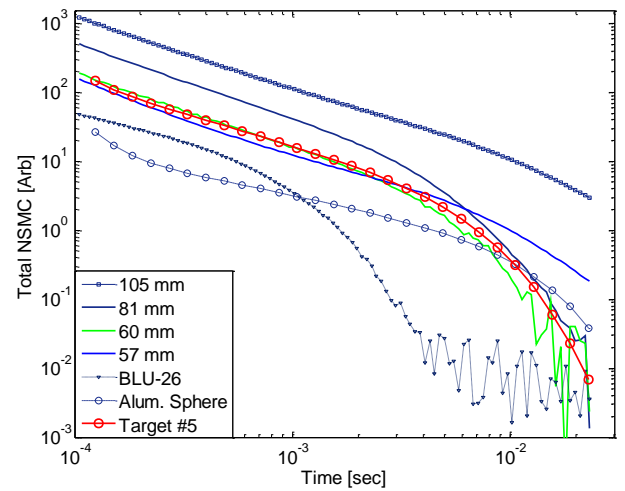
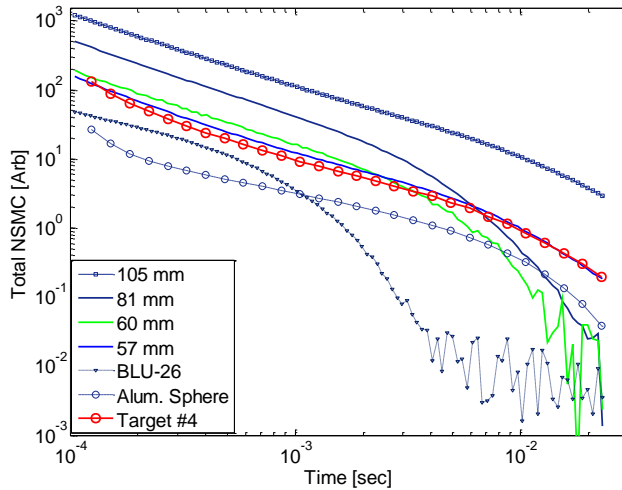


Figure 23. NSMS model comparison to library for Target #4 (left) and Target #5 (right).

The algorithm identified correctly all remaining targets. It is worth noticing, in the case of Targets #4 and #5, that the total NSMS was able to differentiate between the 57-mm and 60-mm UXO even though they have comparable geometrical sizes (Figure 23). The results show that at early times/high frequencies the total NSMS from both objects are similar, due to the small skin depth; however, at late times/low frequencies the skin depth becomes significant and the total NSMS of sizable objects is separable and depends on the object's material properties and metal content, demonstrating a good discrimination capability. To further illustrate how the object's EMI response affects the total NSMS, on Figure 24 we added the total NSMS of a non-permeable sphere. The non-permeable sphere has the same size as the BLU-26, which is made of permeable steel. The results show that at early times the NSMS amplitudes of the two spherical targets are similar; at late times, two objects of similar geometric size but different material properties have different total NSMS.

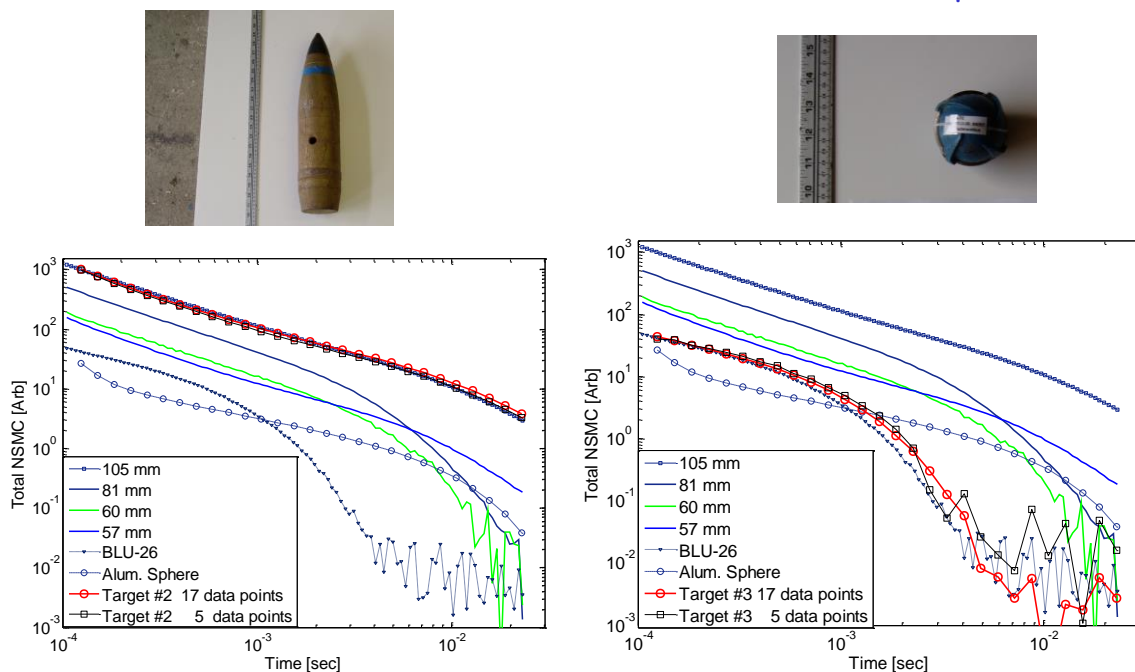


Figure 24. NSMS model comparison to library for Target #2 (left) and Target #3 (right).

Finally we investigate the data density requirement issue for UXO discrimination. UXO cleanup demands real/near-real time detection and discrimination systems to keep cleanup costs reasonably low by minimizing the time spent on each anomaly; moreover, such systems should discriminate between UXO and non-UXO items accurately and reliably. To address this problem here we study the TD-MPV data-density requirements for the NSMS model. Studies were done for Targets #2 and #3. The targets' total NSMS, as well as their positions and orientations, were inverted using either 17 or 5 measurement points. The inverted total NSMS values as functions of time for both cases are similar and they correctly coincide with the true object's total NSMS. Thus the results suggest that the amplitude of the total NSMC remains stable as the number and density of data points are reduced substantially for single-object discrimination.

4 ESTCP live-site classification studies using advanced models

4.1 Introduction

The Environmental Security Technology Certification Program (ESTCP) recently launched a series of live-site UXO classification blind tests at increasingly challenging and complex sites [55-57] aiming to demonstrate the performance of advanced EMI detection technologies and UXO discrimination and classification algorithms. The first test was conducted in 2007 at the UXO live site at the former Camp Sibert in Alabama using first-generation EMI sensors (the commercially available EM61-MK2 and EM-63, both developed by Geonics Ltd.). The Sibert test was relatively simple: one had to discriminate well-isolated large intact 4.2" mortars from smaller range scrap, shrapnel, and cultural debris. The second ESTCP discrimination study to demonstrate the applicability of EMI classification technologies was set up in 2009 at the live UXO site in San Luis Obispo (SLO) in California and featured a more challenging topography and a wider mix of TOI [55, 56]. Magnetometers and first-generation EMI sensors were deployed on the site and used in survey mode. Two advanced EMI sensing systems—the Berkeley UXO Discriminator (BUD) and the Naval Research Laboratory's TEMTADS EMI array were used to perform cued interrogation of the anomalies detected. A third advanced system, the Geometrics MetalMapper was used in both survey and cued modes for identifying and classifying anomalies. Among the munitions buried at SLO were 60-mm and 81-mm projectiles, 4.2" mortars, and 2.36" rockets; three additional munition types were discovered during the course of the demonstration. The third site chosen was the former Camp Butner in North Carolina. That demonstration was designed to investigate evolving classification methodologies at a site contaminated with 37-mm projectiles, adding yet another layer of complexity into the process [58-60], and fourth site was Camp George West in Colorado to study classification performance of the MPV system. In this chapter we describe the work we performed when we participated in those studies and summarize the results we obtained.

4.2 Camp Sibert

In 2006, researchers affiliated with Sky Research, Inc. collected data at Camp Sibert using the EM-63, a cart-based step-off time-domain EMI sensor produced by Geonics Ltd. [61]. The targets buried in 216 cells—some of which were empty—included unexploded 4.2" mortar shells, mortar explosion byproducts like base plates and partial mortars (i.e., stretched-out half-shells), smaller shrapnel, and unrelated metallic clutter; some examples appear in Figure 25. The different items were distributed as shown in Figure 25(d).



(a) 4.2" mortar shell



(b) Base plate



(c) Half-shell

Type	Training	Testing	Total
UXO	38	34	72
Partial	12	23	35
Base	5	40	45
Scrap	6	25	31
Clutter	4	22	26
Empty	1	6	7
Total	66	150	216

(d) Cell contents

Figure 25: Camp Sibert anomalies: 4.2 inch, base plates and partial mortars.

We analyzed the Sibert data using HAP and NSMS. By combining those two techniques we made sure our method of analysis [62, 63] avoided the tendency of inversion algorithms to linger in local minima. We performed the localization step independently at the outset and then used its results to help in the characterization, allowing for fast and accurate determination of the total NSMS for each target. We classified these NSMS values using a heuristic pattern-matching method (Section 4.2.1), an open-source implementation [64] of SVM (Section 4.2.3), and mixed modeling (Section 4.2.4). The SVM-based classification improved upon template-matching [65, 66] in that it required less human intervention and was thus faster to run and easier to adapt to other sets of observations. On the other hand, the semi-supervised Gaussian mixture model provided a classification performance exceeding that of SVM, which made it our preferred statistical classification procedure for use in all subsequent classification tasks.

4.2.1 Target location and characterization; preliminary pattern-matching classification

We started the procedure by applying HAP to determine the target location for each cell. Figure 26 compares actual and inverted data at the first and 20th time channels (top and bottom rows

respectively) for one cell. To find the target we take a fictitious $5 \text{ m} \times 5 \text{ m}$ flat square surface concentric with the plot and located 30 cm below the sensor (i.e., at ground level) and divide it into 11×11 patches, each of which is assumed to contain a magnetic-charge distribution of uniform density. We take the measured field data (seen on the left column of Figure 26) and use Eq. (127) to determine q , which in turn allows us to determine $\psi(\mathbf{r})$ using Eq. (129) and construct the matrices of Eq. (126) to find the location. We do this separately for every time channel and get consistent location estimates from gate to gate, which lends credence to their precision. The depths thus determined are also acceptably close to the ground truth.

After finding the locations we run a fully three-dimensional orientation-free NSMS code to determine the time-dependent total NSMS amplitude for all cells. To compute $Q(t)$ we surround the target with a prolate spheroid of semiminor axis $a = 5 \text{ cm}$ and elongation $e \equiv b/a = 4$. This spheroid is divided into seven azimuthal belts, each of which is assumed to contain a radial-magnetic-dipole distribution of constant density. The spheroid is placed at the location estimated by the HAP method and the orientation given by the dipole moment \mathbf{m} obtained from Eqs. (124) and (117)-(119). With all the pieces in place, we apply Eq. (43) to find Ω and Eq. (44) to extract $Q(t)$ for the target. The inverted total NSMS for all anomalies, and for 4.2'' mortars, base plates, and partial mortars are depicted in Figure 27.

It is evident that there are distinguishable differences between the total NSMS for the 4.2'' mortars, the base plates, and the partial mortars. Particularly at late times, each target has different natural decay characteristics that depend on its geometry and material properties. It is also important to notice that the total NSMS for the 4.2'' mortars is very well grouped. To further simplify the classification task we used the Pasion-Oldenburg law to fit the time-dependent NSMS curves, obtaining as a result the amplitudes (k), the power-law exponents (β), and the exponential-decay inverse time constants (γ), all of which we tested as classification features. We obtained the parameters by direct nonlinear least-squares fit of (75) and by linear (pseudo)inversion of its logarithm (131); both procedures gave consistent results. In general we obtain good fits to the measured fields [66]; Figure 26 shows that the discrepancy between the actual data and the model prediction runs only to a few percent.

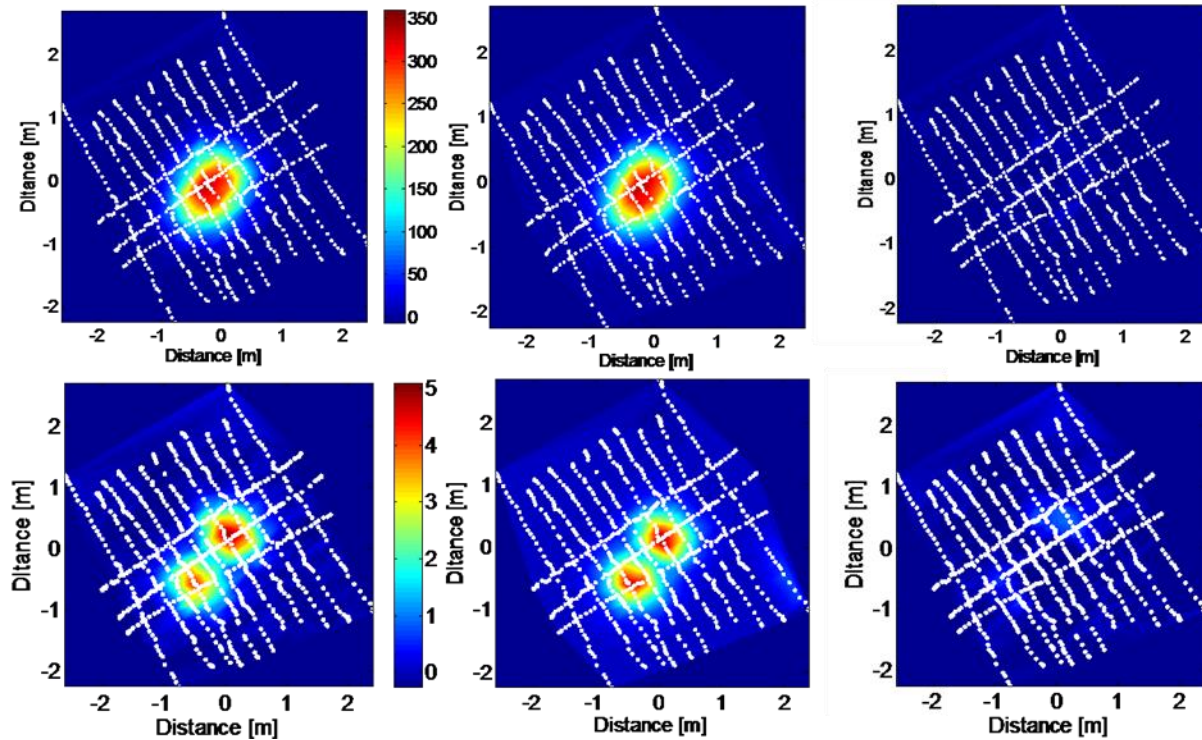


Figure 26: Camp Sibert EM-63 near field distributions: Left and middle columns: actual and modeled data respectively. Right column: misfits.

After investigating different combinations of these feature-space parameters we found that k in conjunction with the ratio $Q(t_{15})/Q(t_1)$ which involves a fixed superposition of β and γ , worked best: the left panel of Figure 28 depicts this winning combination for all items and clearly shows the tight clustering and generous cluster-to-cluster separation that generally lead to reliable classification. (The 15th time channel, centered at about 2.7 ms, was chosen because it takes place late enough to show the behavior described above but early enough that all targets still have an acceptable signal-to-noise ratio; nearby time channels produce similar results.) When we received the ground truth for all targets we proceeded to construct the ROC curve that appears in the right panel of Figure 28. We see that only one excavation out of 130 anomalies is necessary before all UXO are identified correctly.

We obtain similar results using the SVM algorithm.

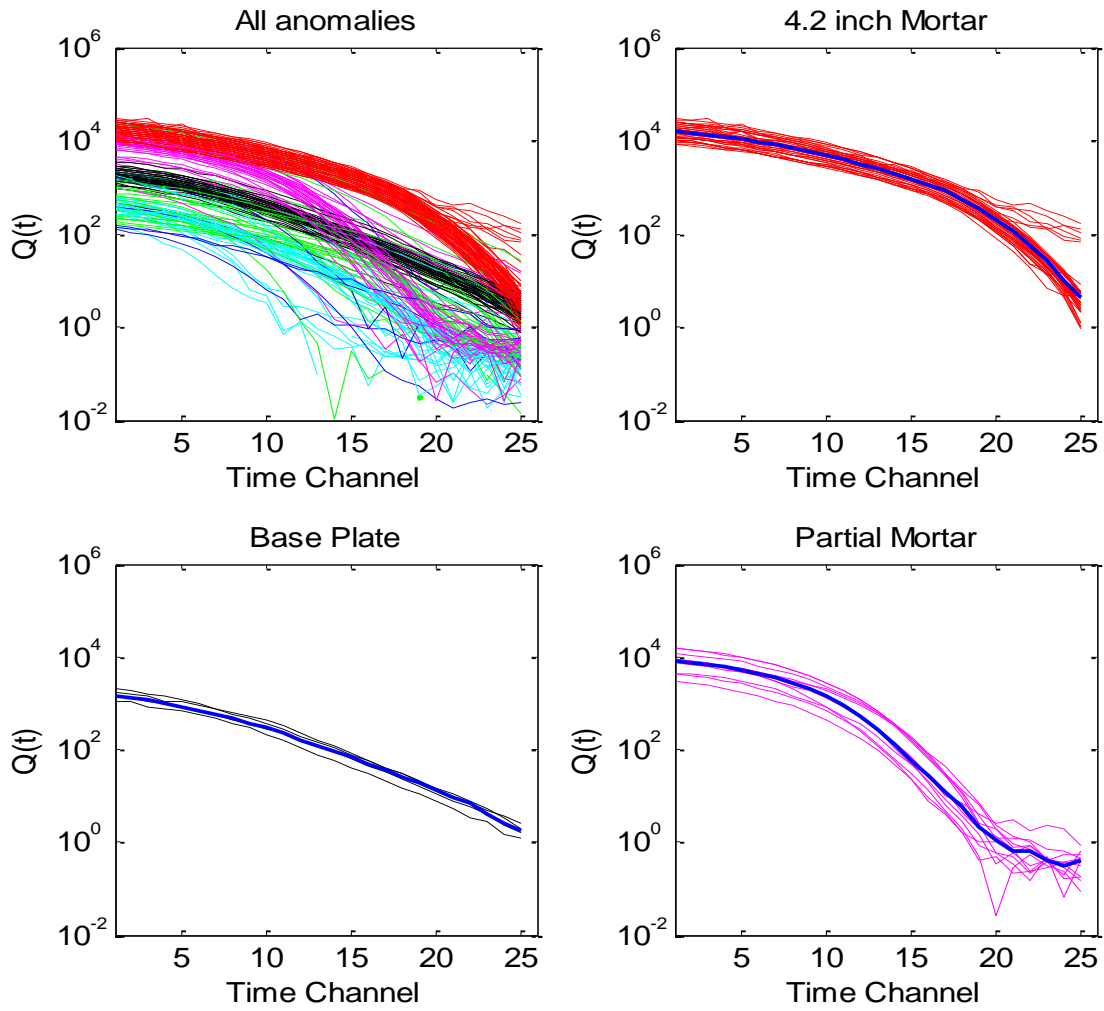


Figure 27: Inverted total NSMS for all anomalies: 4.2'' mortars, base plates, and partial mortars.

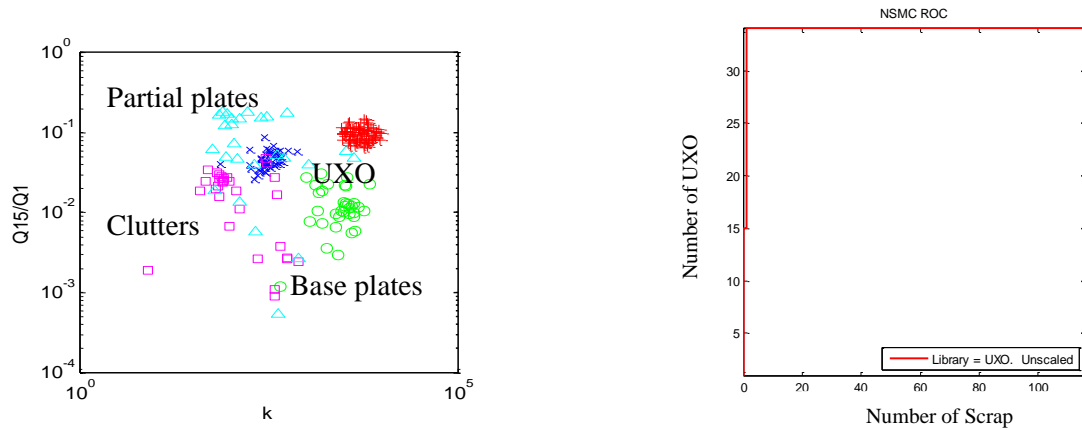


Figure 28: *Left:* Classification features. *Right:* ROC curve of NSMS performance.



Figure 29: a) Unexploded shell from Cell No. 7 and (b,c) the two false alarms obtained by the SVM classifier using k and $Q(t_{15})/Q(t_1)$ as discriminators.

4.2.2 SVM classification

We use a Gaussian RBF kernel for the SVM analysis. The kernel width turns out not to have much influence on the outcome; we usually set it so that a unit in a typical x - or y -axis in a log plot (for example, Figure 30) comprises 100Δ Gaussian widths, where Δ is the dimensionality of the feature space. To find the capacity C we train the SVM with a subset of the training data and a given C , scramble the training set, and use a new subset of the data for testing. We then vary C , setting it to a high value initially and then lowering it, and keep the lowest capacity with which the machine identifies all dangerous items in the test. The procedure is rather ad hoc but effective for the data at hand, given the small sample sizes, the low dimensionality of the feature spaces, and the speed of the SVM implementation. A more systematic search for C and γ using five-fold cross-validation [64] recommends slightly higher capacities that result in identical predictions.

For R and k as features we find the best SVM performance using $C = 10$. The results are displayed (for testing data only) in Table 4 and shown pictorially (for both training and testing) in Figure 30. The matrix element c_{ij} in the table denotes an item of category i that was identified by the SVM as belonging to category j ; in other words, the rows of this contingency table correspond to the ground truth and the columns to predictions. The small markers in the plot show the ground truth (hollow for training data and filled for the tests), while the large markers point out the items for which the SVM makes wrong predictions. For example, a small yellow upright triangle surrounded by a large cyan square is a piece of scrap (clutter unrelated to UXO) incorrectly identified as a base plate. The UXO, with their high initial amplitudes and slow decay, are clustered at the top right corner. We see that there are only two false alarms (i.e., objects identified with UXO that were in fact something else) and that all potentially dangerous items have been identified correctly.

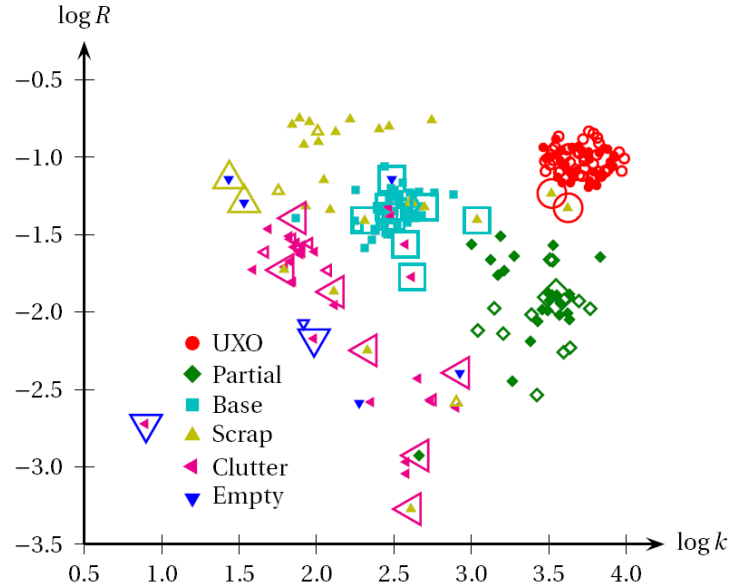


Figure 30: Result of the SVM classification for the Camp Sibert anomalies using the logarithms of k and $R = Q(t_{15}) / Q(t_1)$. The SVM has been trained with capacity $C = 10$ and kernel width $\sigma = 1/200$. The small markers denote the ground truth for both training (hollow) and testing (solid) cells. The larger markers highlight the cases where there is disagreement between the ground truth and the SVM prediction.

Table 4: SVM classification of Camp Sibert anomalies using k and R with $C = 10$

$k, R; C = 10$		SVM prediction					
		UXO	Partial	Base	Clutter	Scrap	Empty
Ground truth	UXO	34	0	0	0	0	0
	Partial	0	22	0	1	0	0
	Base	0	0	39	1	0	0
	Clutter	0	0	4	19	0	2
	Scrap	2	0	3	4	13	0
	Empty	0	1	1	1	2	1

The false alarms, two pieces of non-UXO clutter, appear in Figure 29(b) and Figure 29(c). They are seen to be similar to the 4.2" mortars in size and metal content (cf. Figure 29 (a)), which makes their k and R values lie closer to the tight UXO cluster than to any other anomaly. Here we note that, as can be seen in Figure 25(d), the training data provided by the examiners was somewhat biased toward UXO, while clutter and scrap samples were underrepresented (this was not the case with the testing data and should not be expected in future tests). If we switch training and testing data in the SVM analysis we can achieve perfect discrimination without varying the capacity—though in this case we have more training data than tests. This highlights the importance of having a diverse collection of representative samples to use during the training stage.

Table 5: SVM classification of Camp Sibert anomalies using γ and k with $C = 9$

$\gamma, k; C = 9$		SVM prediction					
		UXO	Partial	Base	Clutter	Scrap	Empty
Ground truth	UXO	34	0	0	0	0	0
	Partial	5	17	0	1	0	0
	Base	0	0	39	0	1	0
	Clutter	0	0	4	15	5	1
	Scrap	2	1	3	5	11	0
	Empty	1	1	2	2	0	0

We can repeat the analysis using other two-dimensional combinations of the Pasion-Oldenburg parameters. Combining k and γ yields results similar to those of k and R , as Figure 31 and Table 5 show. Figure 32 and Table 6 show the classification resulting from the use of β and γ as discriminators. The table shows that we can obtain reasonable discrimination, with all the UXO once again correctly identified, but the increased number of false alarms and the very high capacity needed (four orders of magnitude larger than the previous ones) indicate that this combination of parameters may not be optimal and that this machine is prone to overfitting. A glance at the figure shows the clustering is much less clear-cut than in the previous cases, partly because the range of β is rather small. In fact, combining k and β greatly reduces the performance, since the small β -range and the close similarity in k of the UXO and the partial mortars cause an overlap between the two categories that cannot be disentangled.

It is helpful and straightforward to increase the dimensionality of the feature space. Figure 33 shows the discrimination obtained by running the SVM using all three Pasion-Oldenburg features. The capacity $C = 9$ here, and increasing it changes the results only slightly. The number of false alarms increases: we get the same two pieces of scrap from before, and now a few of the partial mortars are identified as UXO by the algorithm, due in part to the small range of β and in part to the large gap between the UXO and the other anomalies, clearly visible in the figure, which again calls out for more and more-diverse training information.

Finally, it is possible to dispense with the Pasion-Oldenburg model altogether and run an SVM using the “raw” $Q(t)$ as input. The feature space has dimensionality $\Delta = 25$. We scale the values by $Q(t_1)$ and take the logarithm. We find $C = 20$ to be the optimal value. Table 4 shows the results. The performance is slightly inferior to that of R vs. k ; the usual two false alarms are there, along with a few new ones. All the UXO are identified correctly. We can also use the logarithm of Q without any scaling (though the SVM internally rescales the feature space to $[0,1]^A$). A capacity $C = 1$ suffices here. The results appear on Table 5. All dangerous items are once more identified as such.

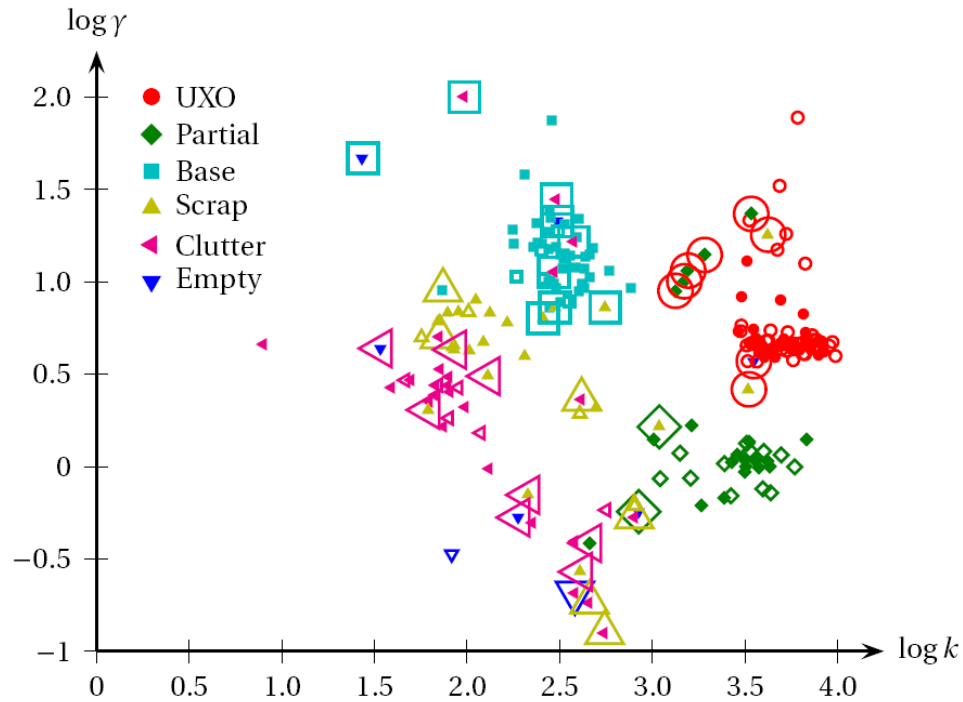


Figure 31: Result of the SVM classification for the Camp Sibert anomalies using the logarithms of the Pasion-Oldenburg parameters k and γ . The SVM here has a capacity $C = 9$. The small markers denote the ground truth for both training (hollow) and testing (solid) cells. The larger markers show the wrong SVM predictions.

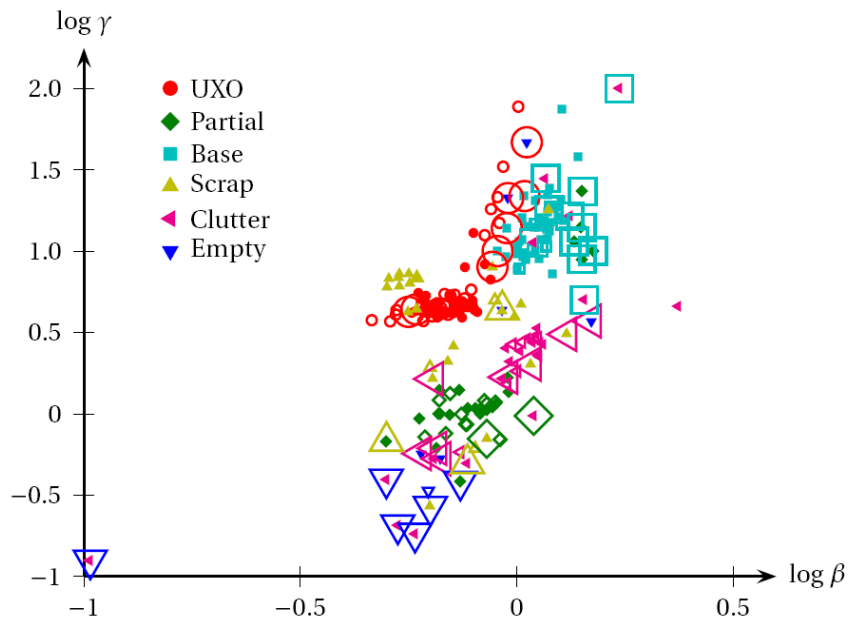


Figure 32: Result of the SVM classification for the Camp Sibert Anomalies using the logarithms of the Pasion-Oldenburg parameters β and γ . The SVM capacity $C = 10^5$. The small markers denote the ground truth for both training (hollow) and testing (solid) cells. The larger markers highlight the wrong predictions made by the SVM.

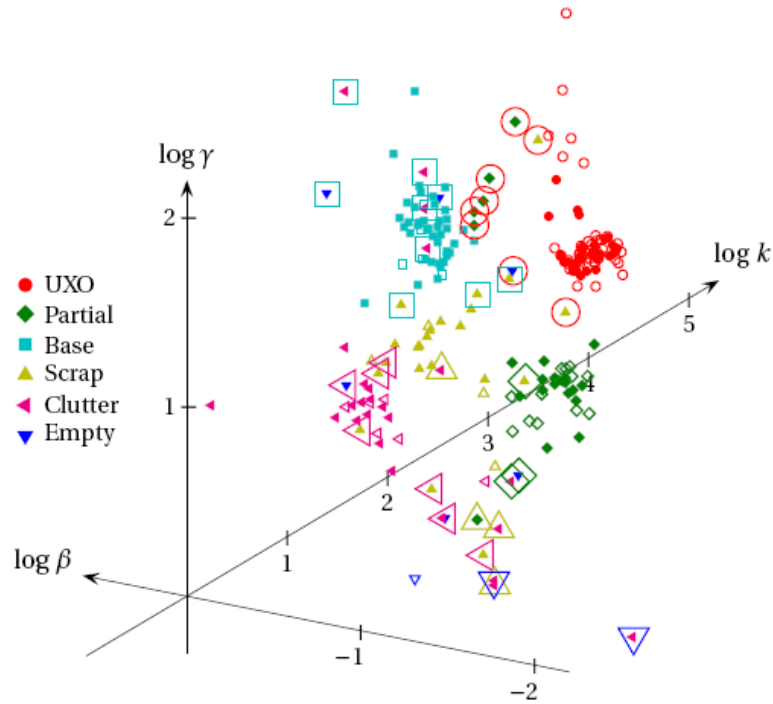


Figure 33: SVM classification of the Camp Sibert Anomalies using the logarithms of k , b , and g . The SVM has $C = 9$. The small markers denote the ground truth for both training and testing cells. The larger markers highlight the cases where there is disagreement between the ground truth and the SVM prediction.

Table 6: SVM classification of Camp Sibert anomalies using β and γ with $C = 105$

$\gamma, \beta; C = 10^5$		SVM prediction					
		UXO	Partial	Base	Clutter	Scrap	Empty
Ground truth	UXO	34	0	0	0	0	0
	Partial	0	14	5	2	1	1
	Base	3	0	37	0	0	0
	Clutter	0	1	5	14	1	4
	Scrap	3	1	1	3	13	1
	Empty	2	0	0	3	1	0

Table 7: SVM classification of Camp Sibert anomalies using the complete NSMS time decay

$Q/Q(t_1); C = 20$		SVM prediction					
		UXO	Partial	Base	Clutter	Scrap	Empty
Ground truth	UXO	34	0	0	0	0	0
	Partial	0	15	0	7	1	0
	Base	3	0	34	3	0	0
	Clutter	0	2	3	14	4	2
	Scrap	3	1	3	3	12	0
	Empty	2	2	1	0	1	0

4.2.3 SVM analysis of Camp Sibert data: summary

In this section we applied the NSMS model to EM-63 Camp Sibert discrimination data. First the locations of the objects were inverted for by the fast and accurate dipole-inspired HAP method. Subsequently each anomaly was characterized at each time channel through its total NSMS strength. Discrete intrinsic features were selected and extracted for each object using the Pasion-Oldenburg decay law and then used as input for a support vector machine that classified the items.

Our study reveals that the ratio of an object's late response to its early response can be used as a robust discriminator when combined with the Pasion-Oldenburg amplitude k . Other mixtures of these parameters also result in good classifiers. Moreover, we can use Q directly, completely obviating the need for the Pasion-Oldenburg fit. In each case the classifier runs by itself and does not require any human intervention. The SVM can be trained very quickly, even when the feature space has more than 20 dimensions, and it is a simple matter to add more training data on-the-fly. It is also possible to use already processed data to classify examples as yet unseen.

We should stress that none of our classifications yielded false negatives: all UXO were identified correctly in every instance. (This is due in part to the clean, UXO-intensive training data provided by the examiners and may change under different conditions.) The number of false alarms (false positives) varies with the classification features, but is in general low and can be as low as 2 out of 36 reported positives. Figure 30, Figure 31 and Figure 32 show, among others, how these false alarms occur: Some of the clutter items have a response that closely resembles that of UXO. While this will inevitably arise, it may still be possible to make the SVM more effective—and perhaps approach 100% accuracy—by including some of these refractory cases during the training. That said, there will certainly be cases in the field where the non-uniqueness inherent to noisy inverse scattering problems will cause the whole procedure to fail and yield dubious estimates. In those cases it will be necessary to assume the target is dangerous and dig it up.

In a completely realistic situation, where in principle no training data are given and the ground truth can be learned only as the anomalies are excavated, one can never be sure that the data already labeled constitute a representative sample containing enough of both hazardous and non-hazardous items. This difficulty is mitigated by two facts: 1) Usually at the outset we have some idea of the type of UXO present in the field, and 2) The (usually great) majority of detected anomalies will not be UXO and thus random digging will produce a varied sampling of the clutter present. Methods involving semi-supervised learning exploit this gradual revealing of the truth and have been found to perform better at UXO discrimination than supervised learning methods like SVM when starting from the point dipole model

[63, 67]. (Active learning methods, which try to infer which anomalies would contain the most useful information and could thus serve to guide the anomaly unveiling, show further, though fairly minor, improvement.) Combining this more powerful learning procedure with the excellent performance of the HAP/NSMS method may enhance the discrimination protocol and should be the subject of further research.

In summary, the results presented here show that our search and characterization procedure, whose effectiveness is apparent from several recent studies [23, 65, 66, 68], can be combined with an SVM classifier to produce a UXO discrimination system capable of correctly identifying dangerous items from among munitions-related debris and other natural and artificial clutter.

We repeated the analysis using the semi-supervised Gaussian mixture approach. The solution process and results are presented in Section 4.2.4. We found that the method provides excellent classification performance and has the advantage over SVM that it is less dependent on training data. This made it our preferred statistical classification model, and we have continued to prefer it.

4.2.4 Mixed model approach applied to Camp Sibert data

We also tested the mixed model approach of Section **Error! Reference source not found.** on the 216-sample Camp Sibert data. Initially we took the time decay of the total NSMS over 25 time channels for all targets and parameterized it using the Pasion-Oldenburg law of equation (75). Taking the logarithm of that equation we arrive at the linear model

$$\ln Q(t) = \ln k - \beta \ln t - \gamma t. \quad (131)$$

As features we use k and the ratio $Q(t_{15})/Q(t_1)$. Figure 34 is a log-log plot of $Q(t_{15})/Q(t_1)$ vs. k . Initially we used K -means clustering to estimate the number of target types; the algorithm found five clusters (see Figure 34). Then we proceeded to classify the targets. The resulting classification into the five classes is depicted in Figure 35 and the corresponding ROC curves are presented in Figure 36.

The results illustrated that the semi-supervised Gaussian mixture model provides excellent classification performance over the SVM. This made the semi-supervised Gaussian mixture our preferred statistical classification model, and was used in the consequence classification studies.

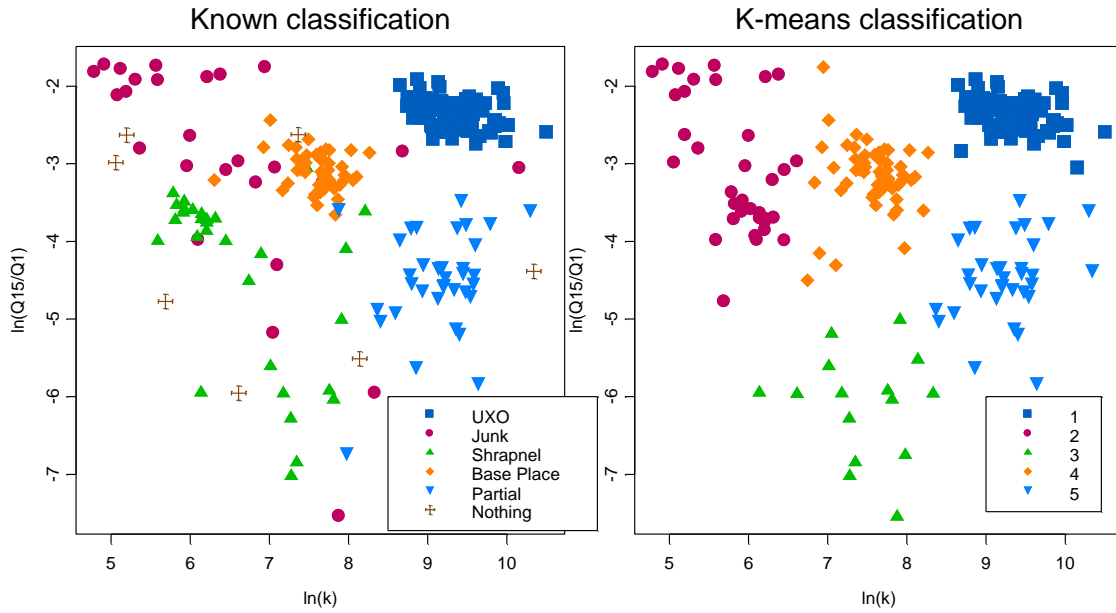


Figure 34: Log-scale plot of $Q(t_{15})/Q(t_1)$ vs. k for Camp Sibert data classification. *Left:* Ground truth. *Right:* K-means clustering result.

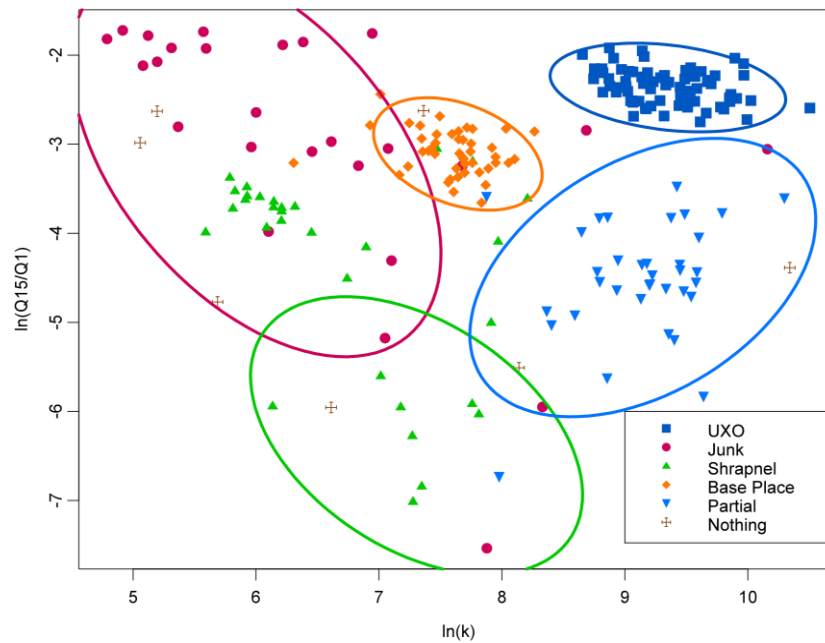


Figure 35: Classification of 216 targets into five classes using a bivariate normal mixture. Also shown are the 95% confidence ellipses.

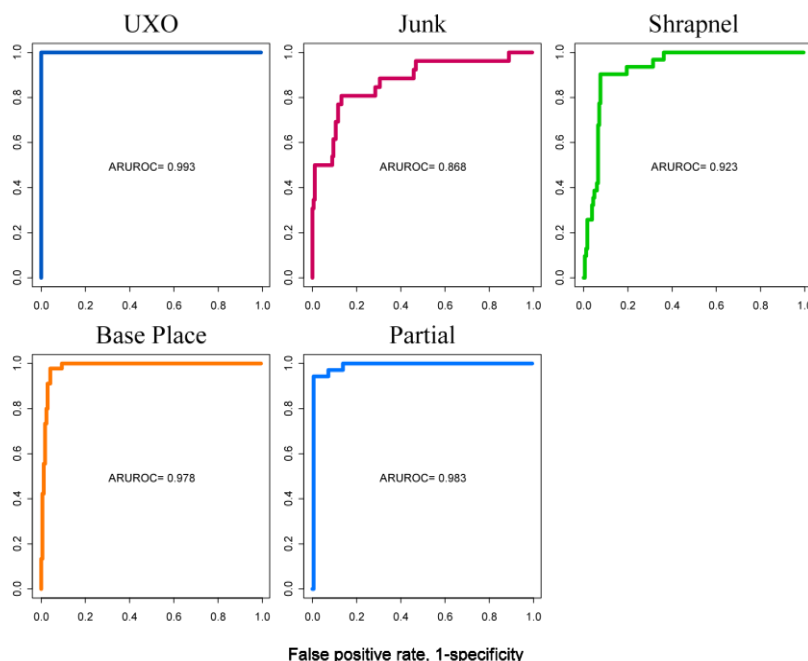


Figure 36: Five ROC curves that indicate the performance of the mixed model approach to Camp Sibert data.

4.3 Camp Butner

The former Camp Butner is a 40,384-acre site located approximately 15 miles north of Durham and straddling Durham, Granville, and Person Counties, all in North Carolina. The War Department acquired the property from private landowners in 1942 for use as a training and cantonment facility during World War II. The camp was primarily established for the training of infantry divisions (including the 78th, 89th, and 4th) and miscellaneous artillery and engineering units [56]. A large variety of munitions have been reported as used at the former Camp Butner, including rifle grenades, 2.36" rockets, 37-mm and 40-mm rounds, 81-mm mortars, and 105-mm, 155-mm, and 240-mm projectiles. Although the historical records are not definitive, it is thought that the targets of interest at the site of the test are mostly 37-mm and 105-mm projectiles; some of the former have a copper band, others do not. The clutter items found on the site are for the most part UXO explosion byproducts like partial mortars (i.e., stretched-out half-shells), smaller shrapnel, and man-made metallic clutter. An initial surface clearance was carried out on the site prior to the collection of digital geophysical data. Then an EM61 survey was conducted on two 100' \times 100' grids for site characterization. A surface clutter analysis and excavation of one of these 100' \times 100' grids confirmed the identities of the targets of interest (TOI), provided an indication of their depth distribution, and gave the demonstrators some information about the clutter environment at the site.

At a live site such as this, the ratio of clutter to TOI is such that only a small number of TOI may be found in a 10-acre area, far from enough to determine any demonstrator's classification performance with acceptable confidence bounds. To avoid this problem, the site was seeded with enough TOI to ensure reasonable statistics. Three types of targets—37-mm and 105-mm projectiles and M48 fuze assemblies—were thus used. The survey data for the study were collected with a line spacing of 50 cm. The detection threshold was set to detect all 37-mm projectiles at a depth of 30 cm [56], which for the EM61-MK2 carted survey corresponds to a threshold of 5.2 mV in the second time gate. Using this detection threshold a first anomaly list was produced. This list was used as a starting point for two detailed cued surveys carried out using TEMTADS and the MetalMapper.

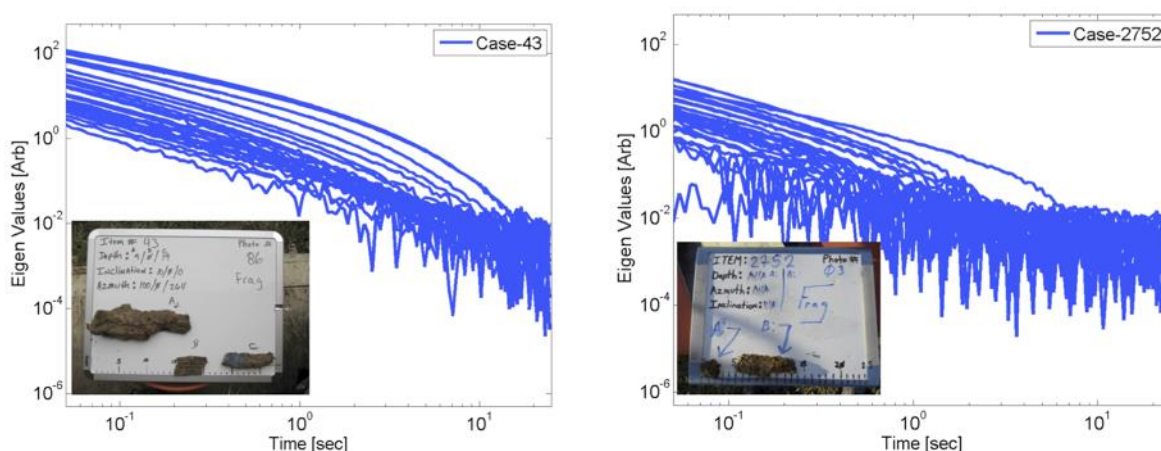


Figure 37: TEMTADS multi-static response matrix eigenvalues versus time for some samples of requested anomalies.

Our team processed both data sets independently using our advanced EMI discrimination techniques and occasionally requesting training data to assist during the classification stage. The main objective of this section is to demonstrate the discrimination performance of the ONVMS model [69] in a live UXO site under realistic field conditions; the method is combined with DE optimization (the two-step approach described in Section 3.3) to determine the locations, orientations, and time-dependent total ONVMS of the subsurface targets. The latter depends on the intrinsic properties of the object in question and can be used for discrimination. To streamline the process we employed JD to estimate the number of potential targets before inverting. To classify the targets in the MM data sets we performed semi-supervised Gaussian-mixture model-based clustering on the total ONVMS. We now present the results of our discrimination and classification strategies when applied to the Camp Butner TEMTADS and MM blind cued data sets. The SERDP office provided us with 2291 cases interrogated with each system. We

divided our team into two groups: One group processed TEMTADS data and the other worked on the MM sets; each group worked independently using different classification strategies. Each team constructed a custom training list (amounting to less than 5% of the entire blind data) and requested the ground truth for those anomalies for use during the classification stage.

4.3.1 TEMTADS data discrimination strategy and classification results using supervised clustering

We processed all the TEMTADS data using the JD and ONVMS models. Initially we used JD to estimate the data quality and the number of potential targets. The JD algorithm constructs a multi-static response matrix using TEMTADS data and computes its eigenvectors and eigenvalues, the latter as a function of time. Studies show that these eigenvalues are intrinsic properties of the targets and that each target has at least three eigenvalues above the threshold (noise level). For example, Figure 38 shows the eigenvalues extracted for a 105-mm HE projectile, a 105-mm HEAT round, an M-48 fuze, and a 37-mm UXO. As the number of targets increases (as in Figure 37 and the third row of Figure 38), so does the number of eigenvalues above the noise level. We thus examined the eigenvalues versus time for each case and used them to estimate the number of targets.

In addition, based on the eigenvalues' time-decay characteristics we built a custom training list. For the most part, the list contained anomalies that had too many above-threshold eigenvalues, like the samples depicted in Figure 37. We requested two batches of training data. The first contained 65 anomalies, all of which were clutter; some had six eigenvalues above the noise level, while others had several eigenvalues mixed with the noise. The second batch consisted mostly of UXO. Once we had the ground truth for all 75 custom identified anomalies we proceeded to invert all TEMTADS data sets using a multi-target ONVMS algorithm combined with DE. We extracted the total ONVMS for every anomaly. Armed with the custom identified training list and the inverted total ONVMS for each case we created a library for M-48 fuzes and 37-mm projectiles without copper band. We did not request training data for either of the 105-mm UXO or for the 37-mm projectile with copper band because we already had TEMTADS test-stand data for these targets. The JD and ONVMS analysis clearly showed the presence of those items at the site. We implemented a library-matching technique in which we quantified the mismatch in total ONVMS between library samples and blind items and used it to classify UXO and non-UXO items. The inverted total ONVMS for the anomalies that were classified as 105-mm HE projectiles, 105-mm HEAT rounds, M-48 fuzes, and 37-mm UXO with and without a copper band are depicted in Figure 39 and Figure 40. All the inverted total ONVMS are seen to cluster well, and each target has a total ONVMS with features—such as its amplitude at the first time channel, its decay rate, or the separation between the primary (blue lines) and secondary (red and green lines) components at different

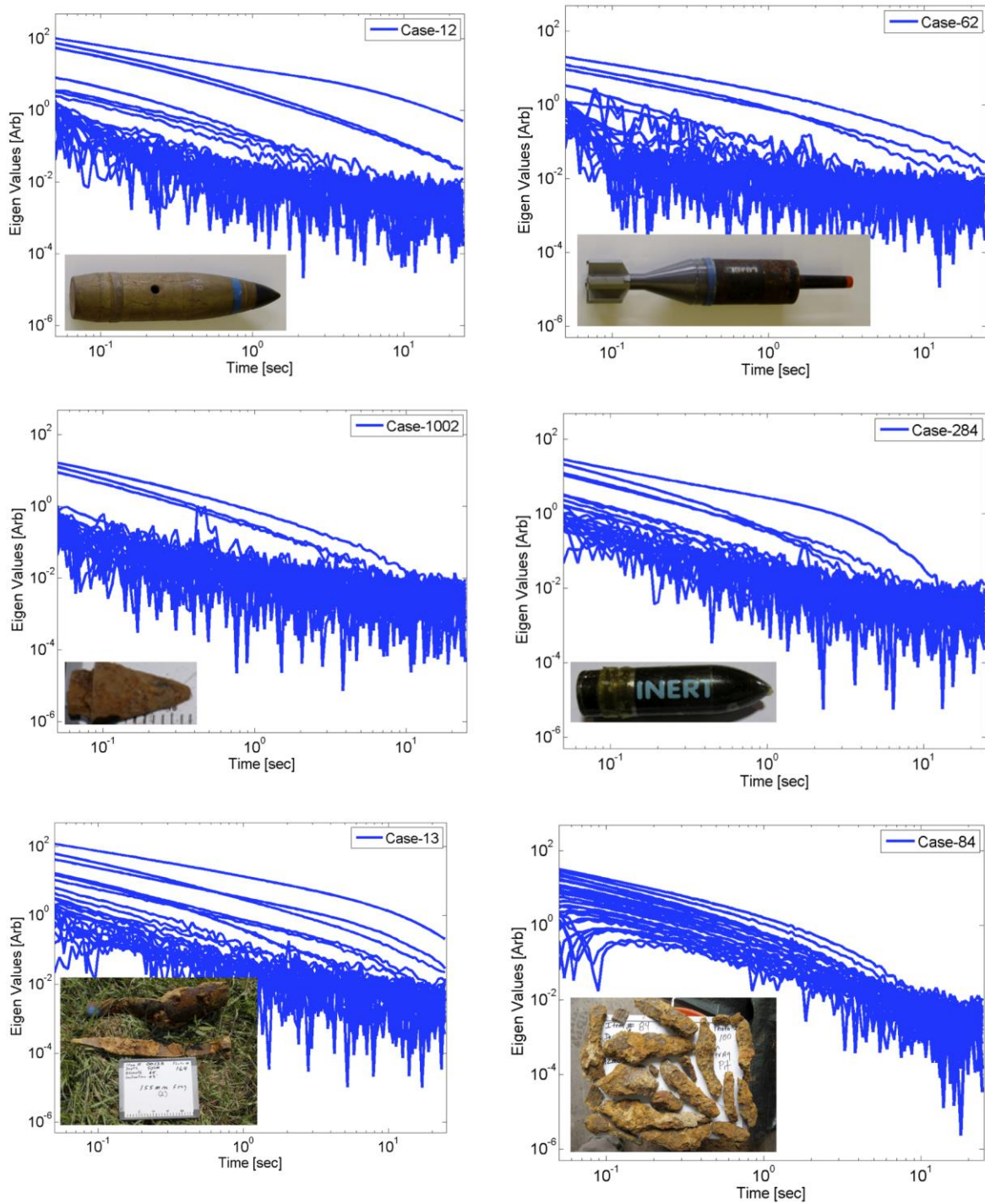


Figure 38: TEMTADS multi-static response matrix eigenvalues versus time for a 105-mm HE projectile and a 105-mm HEAT round (top row), an M-48 Fuze and a 37-mm muniton (center row), and two clutter scenarios, one with two items (left) and another with several (right) (third row).

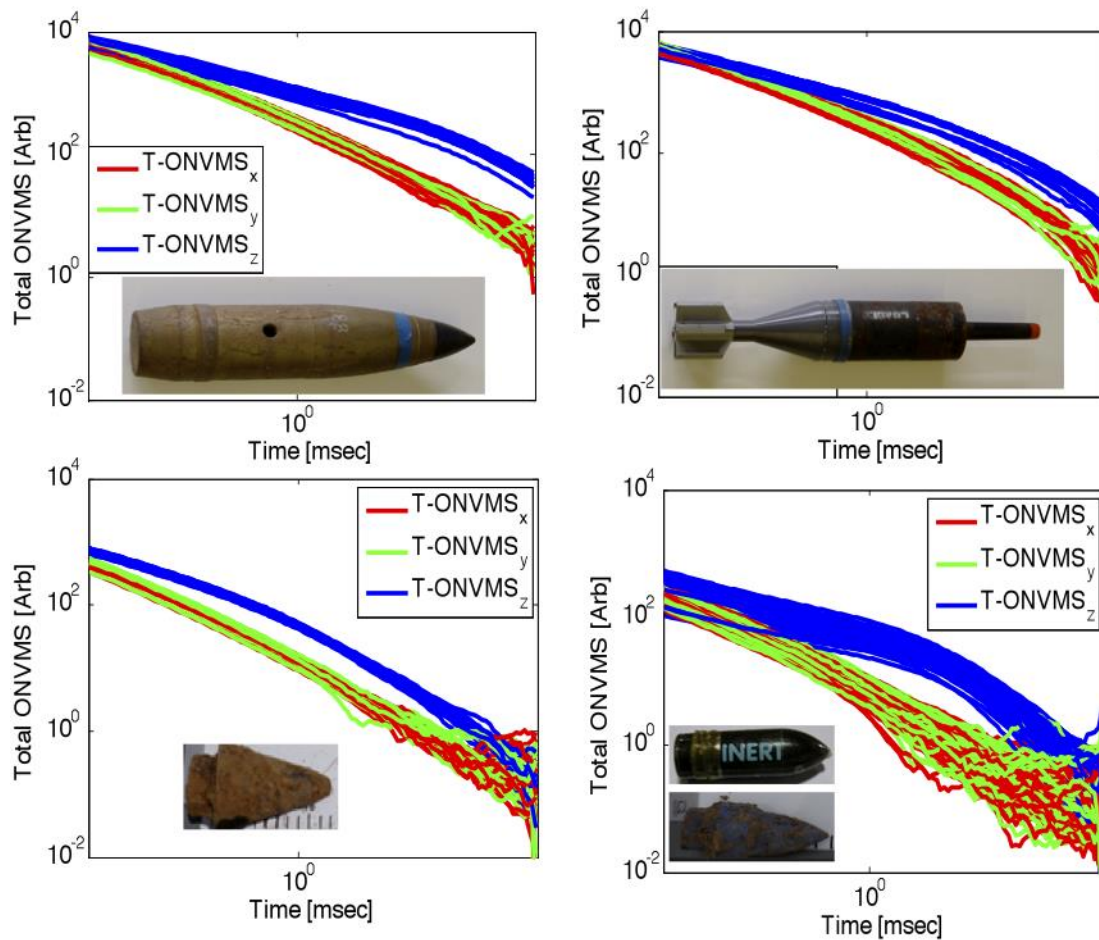


Figure 39: Inverted total ONVMS time-decay profiles for four Camp Butner targets: (top row) 105-mm HE munition and 105-mm HEAT round, and (bottom) M-48 Fuze and 37-mm projectile with copper band.

time channels—that make it amenable to identification. (The most difficult differences to discern were between the M-48 fuzes of Figure 39 and the 37-mm projectiles without copper band of Figure 40). These features allowed us to classify targets as UXO or clutter and also let us sort the UXO by caliber. With this knowledge we created a prioritized dig list that we cross-validated using the time-decay curves of the JD eigenvalues.

The final prioritized dig list was submitted to the Institute for Defense Analyses (IDA) for independent scoring. The scored results were sent back in the form of a receiver operating characteristic (ROC) curve, which we depict in Figure 41. We can see that a) of the 75 targets that were dug for training, 68 targets were not TOI (shift along x -axis) and seven were (shift along y -axis); b) for 95% TOI

classification (the pink dot in Figure 41) only seven extra (false positive) digs are needed; c) to classify all TOI correctly (the light blue dot) only 21 extra (false positive) digs are needed; d) for increased classification confidence the algorithm requested an additional thirty digs after all TOI had been identified correctly.

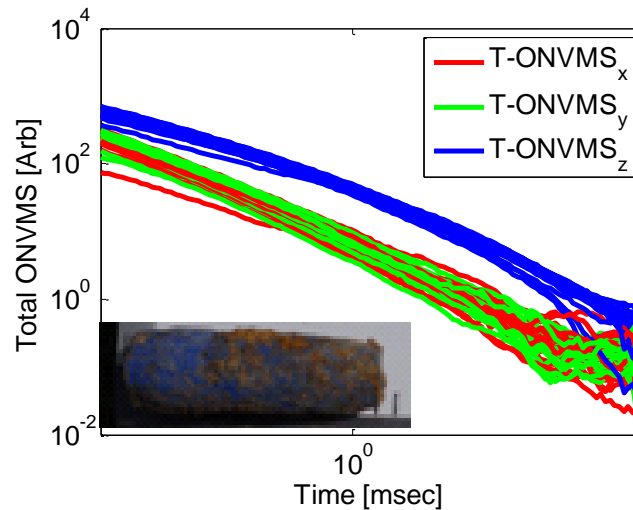


Figure 40: Inverted total ONSMS time decay profiles for a 37-mm projectile without copper band.

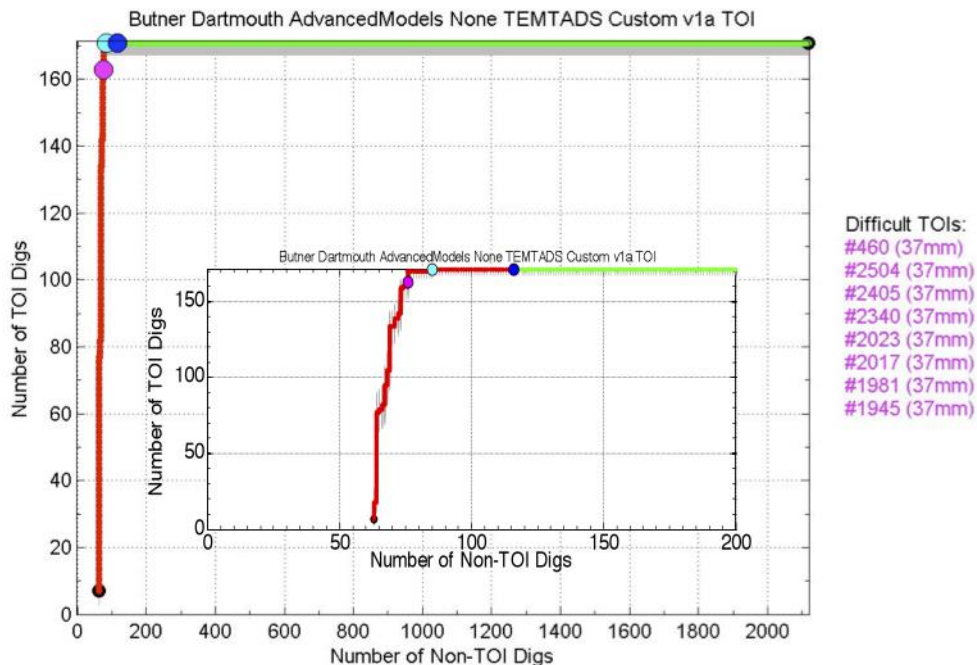


Figure 41: ROC curve for the Camp Butner TEMTADS test data.

4.4 Camp George West

In this chapter discrimination performance of advanced, electromagnetic induction (EMI) models, such as orthonormalized volume magnetic source (ONVMS), joint diagonalization (JD) and differential evolution (DE) approach, are presented for the camp George West, CO site as a part of ESTCP live-site UXO classification pilot studies program. In this demonstration the advanced models are applied to data collected using Man Portable Vector (MPV) instrument in cued mode at Camp George West artillery range. That is located in Jefferson County, Colorado and was used for 75 mm projectiles artillery training from 1930 to 1945. For each anomaly, MPV data are inverted and the targets intrinsic (total volume magnetic source (NVMS) i.e. the size, shape and material properties) and extrinsic (location, depth, orientation) parameters are estimated. The intrinsic parameters are used for classification and a ranked dig-list is generated. The dig-list is submitted to the Institute for Defense Analyses (IDA) for independent scoring. The advanced models classification performances are assessed and documented based on the independent scored results.

4.4.1 Camp George West MPV data inversion and classification scheme

The MPV sensor's Tx and Rx signals detailed modeling approach using the ONVMS-DE algorithm is described in **Error! Reference source not found.**

Step 1. Data pre-processing: All MPV-data were pre-processed using a Matlab Code (see Appendixes in **Error! Reference source not found.**). The code reads comma-delimited format CSV files and transfers them to ASCII files compatible with the ONVMS-DE code (ONVMS_MPV.exe). The user needs only to specify the path to the folder with the CSV files; the code then converts them all.

Step 2. Create MPV Multi Static Response (MSR) data matrix: Using equation **Error! Reference source not found.** we construct the measurement matrix $\bar{\bar{H}}(t_q)$ for each anomaly

and use it to create the MPV MSR matrix $\bar{\bar{B}}(t_q) = \bar{\bar{H}}^T(t_q) \bar{\bar{H}}(t_q)$.

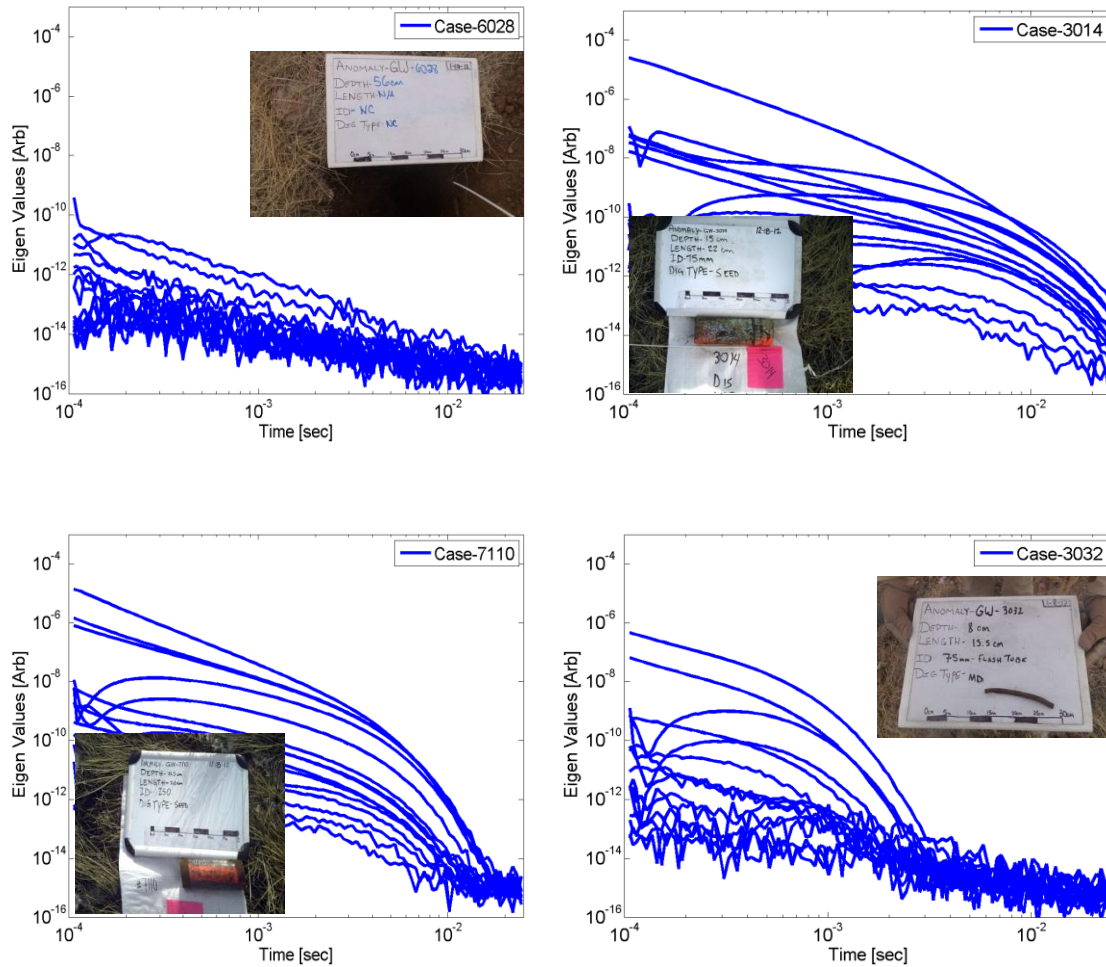


Figure 42. Camp George West MPV multi-static response matrix eigenvalues versus time for some samples of background, 75 mm, ISO and clutter anomalies.

Step 3. Eigenvalue analysis: The JD technique is applied to the created MPV MSR data matrix to extract the time-dependent eigenvalues for each anomaly. The eigenvalues for some of the Camp George West seeded and native anomalies and for background are depicted in Figure 42 respectively. The MSR data matrix eigenvalues are intrinsic properties of the targets; each target has at least three eigenvalues above the threshold (noise level: low magnitude eigenvalues). For example, Figure 42

show the eigenvalues extracted for a background, a 75-mm projectile, an ISO, and a clutter. The results illustrate that each target has distinguishable eigenvalues that can be used for classification; Note that the magnitudes of the MSR eigenvalues depend on the depths and orientations of the targets **Error! Reference source not found.**; therefore the user should use only their shapes when performing classification. In this study, we examined the eigenvalues versus time for each case and used them to estimate the number of targets and SNR. Once we had the JD analysis and estimated SNR for each anomaly we proceeded to invert all cued MPV datasets using the combined ONVMS-DE algorithm for multi-targets.

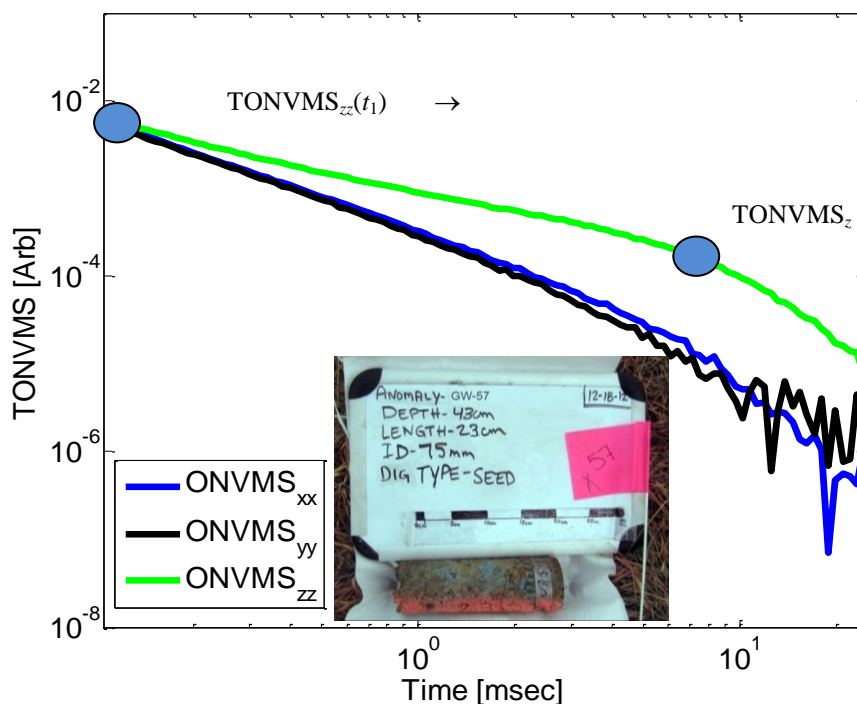


Figure 43. Inverted total ONVMS time-decay profiles for a 75 mm projectile in the Camp George West study, Anomaly #57.

Step 4. Extract the total ONVMS for each anomaly. The targets' extrinsic and intrinsic parameters, including the total ONVMS where extorted for all anomalies.

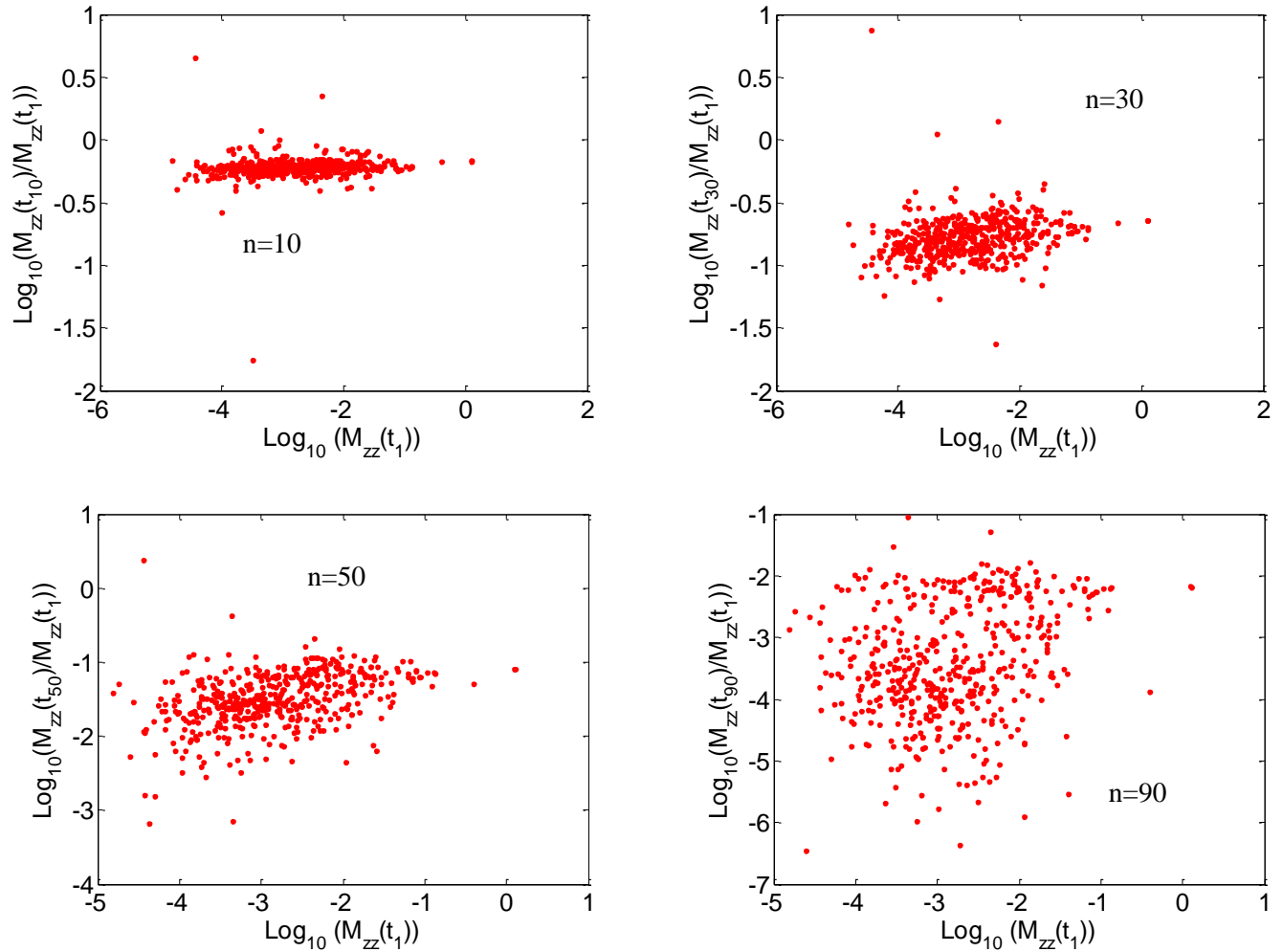


Figure 44. Scatter plot of size and decay for all Camp George West anomalies based on the extracted total ONVMS for time channels N# 5, 10, 20, and 35.

Step 5. Create a custom training list. We use the size i.e. magnitude of the inverted primary effective polarizability $M_{zz}(t_1)$ ($M_{zz}(t) = \text{ONVMS}_{zz}(t)$) at the first time channel and decay i.e. ratio of the primary effective polarizability at the n -th time channel $M_{zz}(t_n)$ to that at the $M_{zz}(t_1)$ as classification feature parameters and determined the best separations. The values of $\log_{10}[M_{zz}(t_1)/M_{zz}(t_n)]$ versus $\log_{10}[M_{zz}(t_1)]$ are plotted for all Camp George West MPV data sets, at the 10th, 30th, 50th, and 90th time channels. Visual examination shows that there are no distinguishable clusters at the 10th channel; at later times, on the other hand, the decay-vs.-size distribution starts to cluster. We used the

features evaluated at the 90th time channel and applied statistical classification techniques **Error!**
Reference source not found..

Step 6. For each cluster we computed the centroid and determined the anomaly closest to it. We included this anomaly in the custom training data list. The clustering results are depicted in Figure 45. Each color corresponds to a cluster; circles denote anomalies for which the ground truth was asked. In addition to the statistical clustering algorithm, ONVMS time decay curves were inspected for each anomaly: we used the TONVMS time decay shapes and symmetries to further validate or modify the custom training anomaly list. Anomalies with significantly asymmetric TONVMS were removed from the training list; anomalies with fast decay but symmetric profiles were added to the training list for which we requested the identifying ground truth.

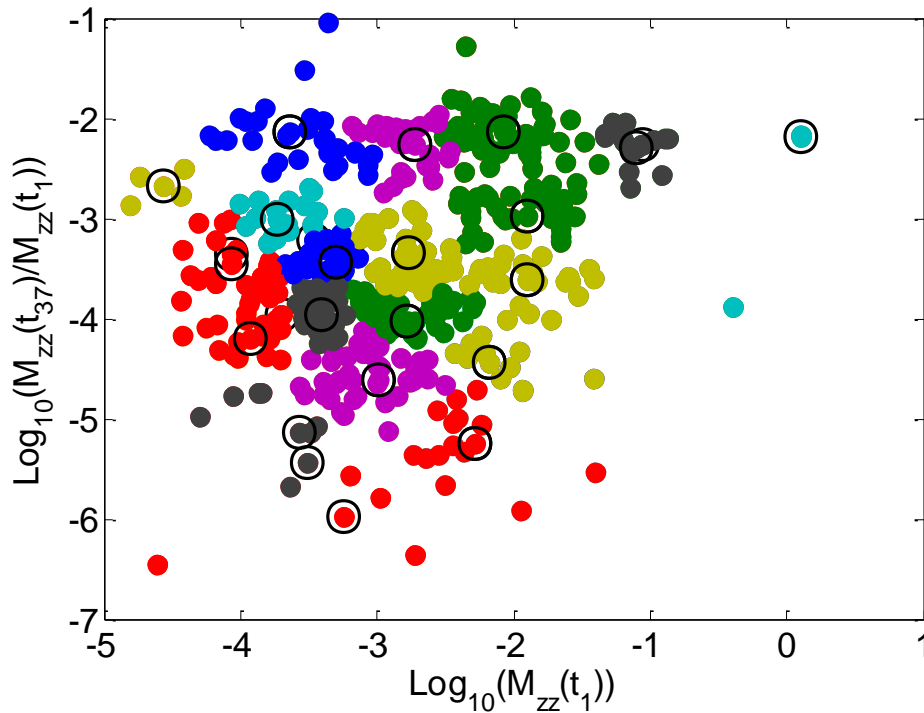


Figure 45. Result of the clustering for the Camp George West anomalies using the size and shape information for $n = 90$. The circles denote the anomalies for which the ground truth was asked.

Step 7. Request ground truth for selected anomalies. The custom training list, a combination of JD, clustering and ONVMS-DE single-target inversion results, was submitted to the ESTCP office, which

then provided the ground truth for training. We used the delivered ground truth to identify the different possible TOI types and their size variations. There were native site-specific 75-mm projectiles and their parts, along with seeded ISO targets which the ESTCP office identified as TOI.

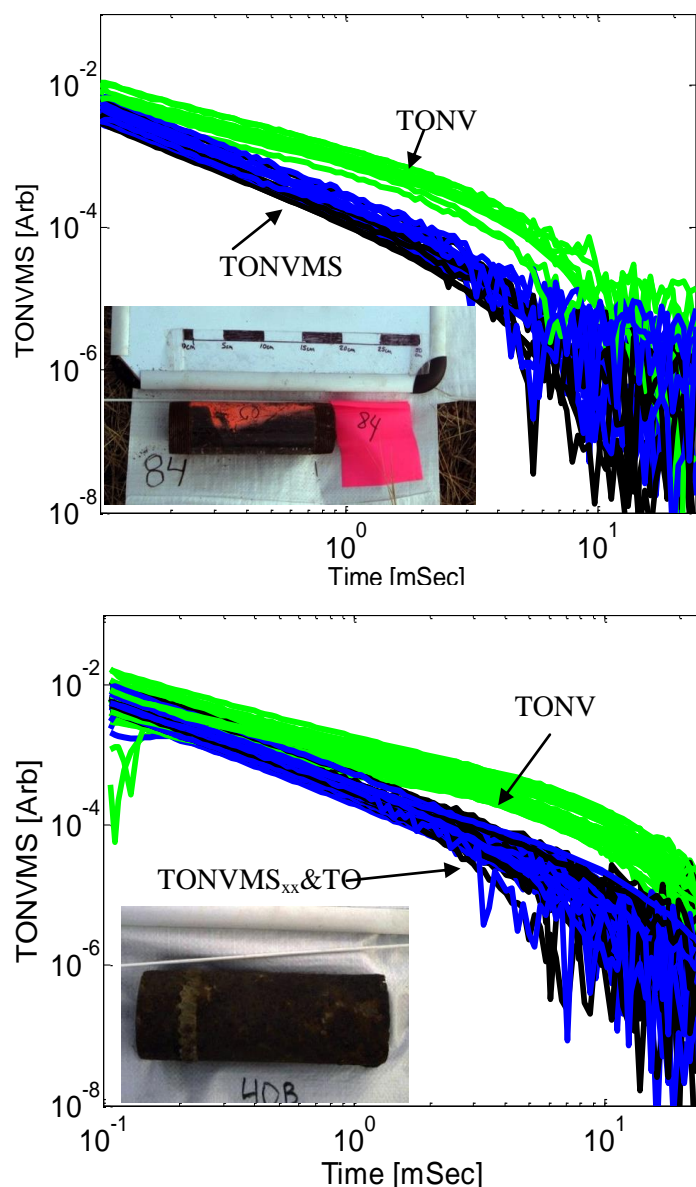


Figure 46. Inverted total ONVMS time-decay profiles for ISO (upper figure) and 75 mm projectiles (lower figure) targets.

Step 8. Create ranked dig list. Armed with the ground truth of (a total of 20) custom identified training anomalies and the inverted total ONVMS for each MPV cued data, we created a

library for all seeded and native TOI. The inverted total ONVMS for the anomalies that were classified as TOI appear in Figure 46 and Figure 47. All the inverted total ONVMS are seen to cluster well, and each target has a total ONVMS with features that make it amenable to identification: its amplitude at the first time channel, its decay rate, or the separation between the primary (green lines) and secondary (black and blue) components at different time channels. However, the total ONVMS for the native MEC targets (such as whole and partial 75-mm projectiles) varied in magnitude due to size variations, but, as can be seen in Figure 47, they were symmetric (i.e., $\text{TONVMS}_{xx} = \text{TONVMS}_{yy}$). Therefore, to classify native targets as MEC and clutter we used a classification approach based on symmetry and time-decay shapes.

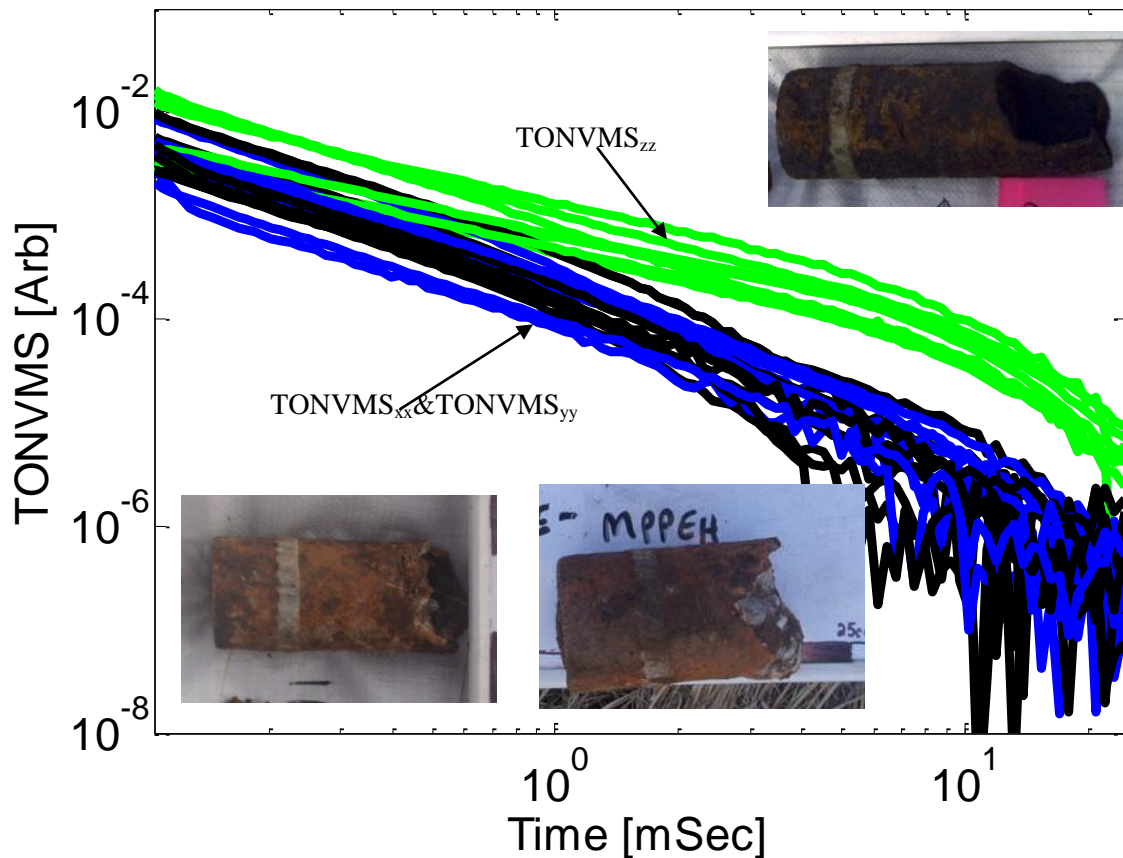


Figure 47. Inverted total ONVMS time-decay profiles for whole and partial native partial 75 mm projectiles. Green, black and blue lines are for total ONMVS_{zz}, ONMVS_{yy} and ONMVS_{xx}, respectively.

Step 9. Submit the dig list to ESTCP. The final prioritized dig list was submitted to the Institute for Defense Analyses (IDA) for independent scoring. The scored results were sent back in the form of a

receiver operating characteristic (ROC) curve, which we depict in Figure 48. The result shows that of the 20 targets that were dug for training, 14 targets were not TOI (shift along x -axis) and 6 were (shift along y -axis); all TOI targets were classified as TOI. The result clearly shows that advanced EMI sensing and classification technologies can be applied at active UXO sites. The technology provides the ability to leave at least 93% of clutter items in the ground.

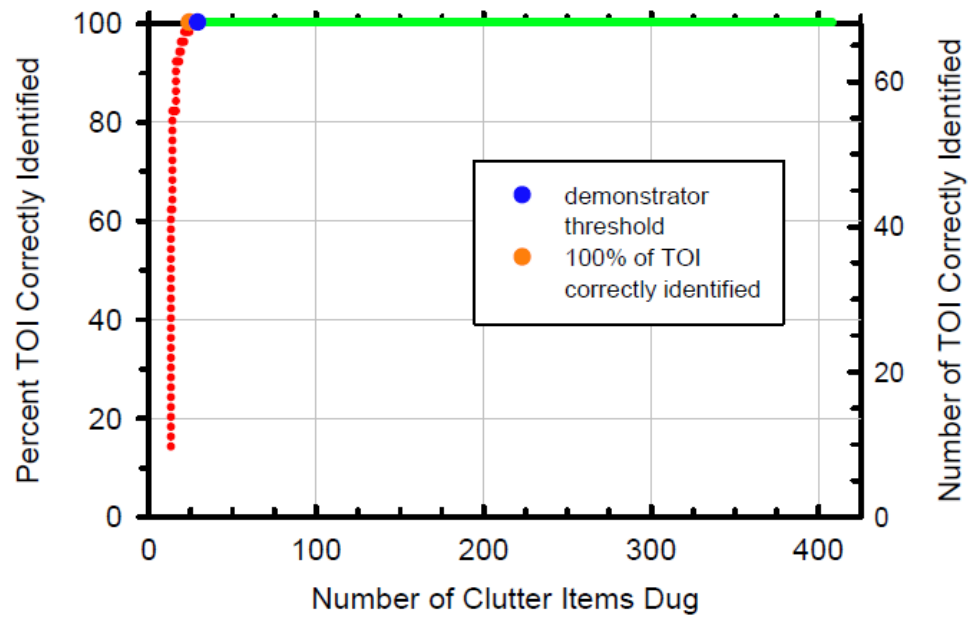


Figure 48. ROC curve for the Camp George West data.

5 Conclusions

ARO project# 5500-EV entitled “Resolving and Discriminating Overlapping Anomalies from multiple Objects in Cluttered Environments ” is complete. We have developed physically complete forward approaches: Standardized Excitation Approach for understanding modeling targets EMI responses in great details; Normalized surface magnetic source model (NSMS) for EMI sensors data inversion and classification. Orthonormalized volume magnetic source model (ONVMS) for next generation EMI systems data analysis and subsurface multiple targets classification. These models were combined with advanced signal processing and data-inversion approaches, which provided robust regularization and classification feature parameters estimations for targets intrinsic, such as magnetic polarizabilities, multi-static data matrix eigenvalues, and extrinsic, i.e. targets locations and orientations. These advanced signal processing algorithms are: Joint diagonalization for multi-target data pre-processing (JD); Differential evolution (DE) for estimating targets locations and orientations; A field-potential (HAP) method to locate targets.

Our advanced forward-inverse and signal processing algorithms have been applied to next generation sensors data sets collected at several live UXO sites. We developed site specific UXO libraries for each live UXO sites. These libraries were used for targets classification via a finger-print matching technique. Our models were adapted to all next-generation sensors, including the MetalMapper, TEMTADS and MPV data sets. The models were applied to blind live-site UXO discriminations studies. The methods performed very well at Camp Butner, Camp George West demonstration sites

6 References

- [1] I. Shamatava, F. Shubitidze, K. O'Neill, K. Sun, and K. Paulsen, "Simple magnetic charge model for representation of emi responses from a buried UXO," 2004, pp. 155-159.
- [2] F. Shubitidze, K. O'Neill, B. Barrowes, I. Shamatava, J. Fernandez, K. Sun, *et al.*, "Application of the normalized surface magnetic charge model to UXO discrimination in cases with overlapping signals," *Journal of Applied Geophysics*, vol. 61, pp. 292-303, 2007.
- [3] F. Shubitidze, K. O'Neill, I. Shamatava, K. Sun, and K. Paulsen, "A simple magnetic charge model for classification of multiple buried metallic objects in cases with overlapping signals," 2005.
- [4] F. Shubitidze, K. O'Neill, I. Shamatava, K. Sun, and K. Paulsen, "Combined differential evolution and surface magnetic charge model algorithm for discrimination of UXO from non-UXO items: simple and general inversions," 2005, p. 346.
- [5] J. D. Jackson, *Classical electrodynamics*, 3rd ed. New York: Wiley, 1999.
- [6] C. O. Ao, H. Braunisch, K. O'Neill, and J. A. Kong, "Quasi-magnetostatic solution for a conducting and permeable spheroid with arbitrary excitation," *Geoscience and Remote Sensing, IEEE Transactions on*, vol. 40, pp. 887-897, 2002.
- [7] H. Braunisch, C. O. Ao, K. O'Neill, and J. A. Kong, "Magnetostatic response of conducting and permeable prolate spheroid under axial excitation," *Geoscience and Remote Sensing, IEEE Transactions on*, vol. 39, pp. 2689-2701, 2001.
- [8] B. E. Barrowes, K. O'Neill, T. M. Grzegorzczuk, C. Xudong, and J. A. Kong, "Broadband analytical magnetostatic electromagnetic induction solution for a conducting and permeable spheroid," *Geoscience and Remote Sensing, IEEE Transactions on*, vol. 42, pp. 2479-2489, 2004.
- [9] F. Shubitidze, K. O'Neill, I. Shamatava, K. Sun, and K. D. Paulsen, "Analysis of EMI scattering to support UXO discrimination: heterogeneous and multiple objects," 2003, p. 928.
- [10] F. Shubitidze, K. O'Neill, I. Shamatava, and K. Sun, "Coupling between highly conducting and permeable metallic objects in the EMI frequency range," *Applied Computational Electromagnetics Society Journal*, vol. 19, pp. 139-148, Mar 2004.
- [11] F. Shubitidze, K. O'Neill, I. Shamatava, K. Sun, and K. D. Paulsen, "Use of standardized source sets for enhanced emi classification of buried heterogeneous objects," 2004, p. 263.
- [12] J. T. Miller, T. H. Bell, J. Soukup, and D. Keiswetter, "Simple phenomenological models for wideband frequency-domain electromagnetic induction," *Geoscience and Remote Sensing, IEEE Transactions on*, vol. 39, pp. 1294-1298, 2001.
- [13] K. Sun, K. O'Neill, F. Shubitidze, I. Shamatava, and K. D. Paulsen, "Fast data-derived fundamental spheroidal excitation models with application to UXO identification," *Detection and Remediation Technologies for Mines and Minelike Targets IX, Pts 1 and 2*, vol. 5415, pp. 855-865, 2004.
- [14] K. Sun, K. O'Neill, F. Shubitidze, I. Shamatava, and K. D. Paulsen, "Fast data-derived fundamental spheroidal excitation models with application to UXO discrimination," *Geoscience and Remote Sensing, IEEE Transactions on*, vol. 43, pp. 2573-2583, 2005.
- [15] F. Shubitidze, K. O'Neill, I. Shamatava, K. Sun, and K. D. Paulsen, "Fast and accurate calculation of physically complete EMI response by a heterogeneous metallic object," *Geoscience and Remote Sensing, IEEE Transactions on*, vol. 43, pp. 1736-1750, 2005.
- [16] S. D. Billings, "Practical Discrimination Strategies for Application to Live Sites," presented at the SERDP and ESTCP Partners in Environmental Technology Technical Symposium & Workshop, Washington, DC, 2006.
- [17] Y. Zhang, L. Collins, H. Yu, C. E. Baum, and L. Carin, "Sensing of unexploded ordnance with magnetometer and induction data: Theory and signal processing," *Geoscience and Remote Sensing, IEEE Transactions on*, vol. 41, pp. 1005-1015, 2003.

- [18] W. Hu, S. L. Tantom, and L. M. Collins, "EMI-based classification of multiple closely spaced subsurface objects via independent component analysis," *Ieee Transactions on Geoscience and Remote Sensing*, vol. 42, pp. 2544-2554, Nov 2004.
- [19] E. Gasperikova, J. T. Smith, H. F. Morrison, A. Becker, and K. Kappler, "UXO detection and identification based on intrinsic target polarizabilities - A case history," *Geophysics*, vol. 74, pp. B1-B8, Jan-Feb 2009.
- [20] J. T. Smith and H. F. Morrison, "Optimizing receiver configurations for resolution of equivalent dipole polarizabilities in situ," *IEEE Transactions on Geoscience and Remote Sensing*, vol. 43, pp. 1490-1498, Jul 2005.
- [21] J. T. Smith and H. F. Morrison, "Estimating equivalent dipole polarizabilities for the inductive response of isolated conductive bodies," *IEEE Transactions on Geoscience and Remote Sensing*, vol. 42, pp. 1208-1214, Jun 2004.
- [22] T. H. Bell, B. J. Barrow, and J. T. Miller, "Subsurface discrimination using electromagnetic induction sensors," *Geoscience and Remote Sensing, IEEE Transactions on*, vol. 39, pp. 1286-1293, 2001.
- [23] F. Shubitidze, B. E. Barrowes, J. P. Fernández, I. Shamatava, and K. O'Neill, "APG UXO discrimination studies using advanced EMI models and TEMTADS data," presented at the Detection and Sensing of Mines, Explosive Objects, and Obscured Targets XIV, Orlando, FL, 2009.
- [24] N. Geng, C. E. Baum, and L. Carin, "On the low-frequency natural response of conducting and permeable targets," *IEEE Transactions on Geoscience and Remote Sensing*, vol. 37, pp. 347-359, Jan 1999.
- [25] L. R. Pasion and D. W. Oldenburg, "A Discrimination Algorithm for UXO Using Time Domain Electromagnetics," *Journal of Environmental and Engineering Geophysics*, vol. 6, pp. 91-102, 2001.
- [26] G. A. Korn and T. M. Korn, *Mathematical Handbook for Scientists and Engineers*. New York: McGraw-Hill, 1968.
- [27] J. E. Gentle, *Matrix algebra : theory, computations, and applications in statistics*. New York, N.Y. ; London: Springer, 2007.
- [28] L. P. Song, F. Shubitidze, L. R. Pasion, D. W. Oldenburg, and S. D. Billings, "Computing transient electromagnetic responses of a metallic object using a spheroidal excitation approach," *Geoscience and Remote Sensing Letters, IEEE*, vol. 5, pp. 359-363, 2008.
- [29] J. P. Fernández, B. E. Barrowes, T. M. Grzegorzcyk, N. Lhomme, K. A. O'Neill, and F. Shubitidze, "A Man-Portable Vector Sensor for Identification of Unexploded Ordnance," *IEEE Sensors Journal*, vol. 11, pp. 2542-2555, Oct 2011.
- [30] P. Comon, "Independent Component Analysis, a New Concept," *Signal Processing*, vol. 36, pp. 287-314, Apr 1994.
- [31] A. Belouchrani, K. AbedMeraim, J. F. Cardoso, and E. Moulines, "A blind source separation technique using second-order statistics," *IEEE Transactions on Signal Processing*, vol. 45, pp. 434-444, Feb 1997.
- [32] S. Harmeling, A. Ziehe, M. Kawanabe, and K. R. Muller, "Kernel-based nonlinear blind source separation," *Neural Computation*, vol. 15, pp. 1089-1124, May 2003.
- [33] B. N. Flury and W. Gautschi, "An Algorithm for Simultaneous Orthogonal Transformation of Several Positive Definite Symmetrical-Matrices to Nearly Diagonal Form," *Siam Journal on Scientific and Statistical Computing*, vol. 7, pp. 169-184, Jan 1986.
- [34] J. F. Cardoso and A. Souloumiac, "Jacobi angles for simultaneous diagonalization," *Siam Journal on Matrix Analysis and Applications*, vol. 17, pp. 161-164, Jan 1996.
- [35] F. Shubitidze, B. Barrowes, K. O'Neill, I. Shamatava, and J. Fernández, "NSMC for UXO discrimination in cases with overlapping signatures," pp. 65530F-1.
- [36] B. Barrowes, K. O'Neill, D. Snyder, D. George, and F. Shubitidze, "New man-portable vector time domain EMI sensor and discrimination processing," 2006.

- [37] R. Storn and K. Price, "Differential evolution - A simple and efficient heuristic for global optimization over continuous spaces," *Journal of Global Optimization*, vol. 11, pp. 341-359, Dec 1997.
- [38] R. Storn, "System design by constraint adaptation and differential evolution," *Evolutionary Computation, IEEE Transactions on*, vol. 3, pp. 22-34, 1999.
- [39] J. T. Smith, H. F. Morrison, and A. Becker, "Resolution depths for some transmitter-receiver configurations," *Geoscience and Remote Sensing, IEEE Transactions on*, vol. 42, pp. 1215-1221, 2004.
- [40] B. Barrowes and H. Nelson, "Model-based characterization of electromagnetic induction signatures obtained with the MTADS electromagnetic array," *Geoscience and Remote Sensing, IEEE Transactions on*, vol. 39, pp. 1279-1285, 2001.
- [41] D. W. Marquardt, "An Algorithm for Least-Squares Estimation of Nonlinear Parameters," *Journal of the Society for Industrial and Applied Mathematics*, vol. 11, pp. 431-441, 1963.
- [42] K. Levenberg, "A method for the solution of certain problems in least squares," *Quarterly of Applied Mathematics*, vol. 2, pp. 164-168, 1944.
- [43] J. E. Dennis and R. B. Schnabel, *Numerical methods for unconstrained optimization and nonlinear equations*. Philadelphia: Society for Industrial and Applied Mathematics, 1996.
- [44] K. Tavzarashvili, C. Hafner, X. D. Cui, R. Vahdieck, D. Karkashadze, and G. Ghvedashvili, "Model-based parameter estimation (MBPE) for metallic photonic crystal filters," *Applied Computational Electromagnetics Society Journal*, vol. 22, pp. 228-235, Jul 2007.
- [45] M. Berry, "Waves as catastrophes," *Physics Bulletin*, vol. 107, p. 108, 1976.
- [46] V. I. Arnold, *Catastrophe theory*: Springer, 1992.
- [47] N. Bliznyuk, R. J. Pogorzelski, and V. P. Cable, "Localization of Scattered Field Singularities in Method of Auxiliary Sources," in *Proceedings of the IEEE AP-S/URSI Symposium*, 2005.
- [48] A. G. Kyurkchan, B. Y. Sternin, and V. Shatalov, "Singularities of continuation of wave fields," *Physics-Uspekhi*, vol. 39, p. 1221, 1996.
- [49] J. McNeill and M. Bosnar, "Application of time domain electromagnetic techniques to UXO detection," 1996, pp. 34-42.
- [50] K. O'Neill, I. Won, A. Oren, F. Shubitidze, K. Sun, and I. Shamatava, "A new handheld vector EMI sensor with precise 3-D positioning," 2004.
- [51] J. A. Stratton, *Electromagnetic theory*, 1st ed. New York, London,: McGraw-Hill book company, inc., 1941.
- [52] R. Zaridze, G. Bit-Babik, K. Tavzarashvili, D. P. Economou, and N. K. Uzunoglu, "Wave field singularity aspects in large-size scatterers and inverse problems," *Antennas and Propagation, IEEE Transactions on*, vol. 50, pp. 50-58, 2002.
- [53] F. Shubitidze, D. Karkashadze, B. Barrowes, I. Shamatava, and K. O'Neill, "A New Physics-based Approach for Estimating a Buried Object's Location, Orientation and Magnetic Polarization from EMI Data," *Journal of Environmental and Engineering Geophysics*, vol. 13, pp. 115-130, Sep 2008.
- [54] E. Gasperikova, J. T. Smith, H. F. Morrison, and A. Becker, "Berkeley UXO Discriminator (BUD)," 2007.
- [55] ESTCP, "2009 ESTCP UXO Classification Study, Former Camp San Luis Obispo, CA," presented at the Environmental Security Technology Certification Program Demonstration Plan, Arlington, VA, 2009.
- [56] ESTCP, "2010 ESTCP UXO Classification Study, Former Camp Butner, NC," presented at the Environmental Security Technology Certification Program Demonstration Plan, Arlington, VA, 2010.
- [57] H. Nelson, K. Kaye, and A. Andrews, "ESTCP Pilot Program, Classification Approaches in Munitions Response," in *Environmental Security Technology Certification Program*, Arlington, VA, 2007.

- [58] F. Shubitidze, "Camp Butner UXO Data Inversion and Classification Using Advanced EMI Models," presented at the SERDP-ESTCP, Partners, 2010.
- [59] A. Paski, "Former Camp Butner Site Description and EM61 Data Collection and Analysis," presented at the SERDP-ESTCP, Partners, 2010.
- [60] L. Pasion, "UXO Discrimination Using Full Coverage and Cued Interrogation Data Sets at Camp Butner, NC," presented at the SERDP-ESTCP, Partners, 2010.
- [61] N. Cristianini and J. Shawe-Taylor, *An Introduction to Support Vector Machines and other Kernel-Based Learning Methods*. Cambridge: Cambridge University Press, 2000.
- [62] U. Kreßel, "Pairwise classification and Support Vector Machines," in *Advances in Kernel Methods: Support Vector Learning*, B. Schölkopf, C. J. C. Burges, and A. J. Smola, Eds., ed Cambridge, MA: MIT Press, 1999, pp. 255-268.
- [63] Y. Zhang, X. Liao, and L. Carin, "Detection of buried targets via active selection of labeled data: Application to sensing subsurface UXO," *Geoscience and Remote Sensing, IEEE Transactions on*, vol. 42, pp. 2535-2543, 2004.
- [64] C.-C. Chang and C.-J. Lin, "(LIBSVM): a library for support vector machines," 2001.
- [65] F. Shubitidze, J. P. Fernández, B. E. Barrowes, I. Shamatava, and K. O'Neill, "Normalized Surface Magnetic Source Model Applied to Camp Sibert Data: Discrimination Studies," presented at the Applied Computational Electromagnetics Symposium (ACES), Monterey, CA, 2009.
- [66] F. Shubitidze, J. P. Fernandez, I. Shamatava, L. R. Pasion, B. E. Barrowes, and K. O'Neill, "Application of the Normalized Surface Magnetic Source Model to a Blind Unexploded Ordnance Discrimination Test," *Applied Computational Electromagnetics Society Journal*, vol. 25, pp. 89-98, Jan 2010.
- [67] Q. H. Liu, X. J. Liao, and L. Carin, "Detection of unexploded ordnance via efficient semisupervised and active learning," *IEEE Transactions on Geoscience and Remote Sensing*, vol. 46, pp. 2558-2567, Sep 2008.
- [68] I. Shamatava, F. Shubitidze, B. E. Barrowes, J. P. Fernández, and K. O'Neill, "Physically complete models applied to BUD time-domain EMI data," presented at the Detection and Sensing of Mines, Explosive Objects, and Obscured Targets XIV, Orlando, FL, 2009.
- [69] F. Shubitidze, D. Karkashadze, J. P. Fernández, B. E. Barrowes, K. O'Neill, T. M. Grzegorzczuk, *et al.*, "Applying a Volume Dipole Distribution Model to Next-Generation Sensor Data for Multi-Object Data Inversion and Discrimination," in *Proceedings of SPIE*, 2010.